Energy Scaling by Stacking of Ultrashort Pulses in a Passive Enhancement Cavity

FRIEDRICH-SCHILLER-UNIVERSITÄT JENA
PHYSIKALISCH-ASTRONOMISCHE FAKULTÄT

eingereicht von Dipl.-Phys. Sven Breitkopf

geboren am 30.09.1987 in Erfurt, Deutschland

Institute of
Applied Physics
Friedrich-Schiller-Universität Jena

Gutachter:

1. Prof. Dr. Andreas Tünnermann

Institut für Angewandte Physik, Friedrich-Schiller-Universität Jena

2. Prof. Dr. Malte Kaluza

Institut für Optik und Quantenelektronik, Friedrich-Schiller-Universität Jena

3. Prof. Dr. Almantas Galvanauskas

Electrical and Computer Engineering, University of Michigan, USA

Tag der Disputation: 31.05.2018

Contents

1. Introduction

Over the last decades, constantly improved laser output parameters have repeatedly enabled new applications [1, 2]. This applies to continuous-wave (cw) systems [3] as well as for pulsed laser sources down to pulse-durations in the sub-femtosecond range [4]. Today, such ultrafast laser systems are widely considered as unique tools for industry and science. The key parameter to access new applications often is the pulse-peak power. Impressive progress was made over the last decades and one current benchmark laser system is 'BELLA', producing 30-fs pulses with $40\,\mathrm{J}$ of pulse energy, i.e. $1\,\mathrm{PW}$ peak power, at a repetition rate of up to $10\,\mathrm{Hz}$ [5]. However, almost every application is somehow restricted by the low repetition rates and companies as well as researchers in various fields request such high peak powers at repetition rates in the kHz to MHz-range. Out of these emerging applications, probably the most challenging is laser-wakefield particle acceleration (LWFA). Here, an extremely intense femtosecond laser pulse generates a plasma wave which accelerates particles, such as electrons, in its wake-field [6, 7]. There is a growing interest in LWFA schemes due the fact that classical radiofrequency-driven (RF) machines are about to reach their intrinsic limitations, given by their acceleration gradient and, thus, their size and cost [8]. However, even near-future laser-based accelerator applications will require parameters that are well beyond the state-of-the-art, particularly in terms of repetition rate. To generate electrons or positrons at a TeV-energy level via LWFA with fluxes comparable to those of RF-accelerators, a laser architecture that efficiently allows for the combination of PW-peak powers with MW-average powers is required. A few years ago, Leeman et al. estimated that at a laser with a central-wavelength of around $1\,\mathrm{\mu m}$, a pulse energy of $32\,\mathrm{J}$ at a repetition rate as high as $15\,\mathrm{kHz}$, preferably with sub 100-fs pulse-duration and an almost diffraction limited beam quality is required [5, 9]. Setting up such a system once is already an enormous challenge and 100 of such stages would be required in a cascaded setup to achieve said TeV-level particles. This laser parameter range is far beyond the capability of any existing technology today, furthermore, there is a general problem intrinsic to all current laser design approaches. A laser system can be optimized for either high-average power or high peak power operation. Achieving both simultaneously and therewith achieving PW-peak powers

at multi-kHz-repetition rates, is currently impossible. Unfortunately, that is exactly what most applications would require to rise from 'lab-curiosities' to valuable tools in a scientific-laboratory, a clinic or a production facility. One key question is, which laser-technology should act as a fundament for further development towards these goals. While the mentioned bulk-technology, best represented by 'BELLA', can offer impressive parameter sets, the technology faces critical immanent limitations, such as a very low wall-plug-efficiency well below $0.1\,\%$ and thermal issues, which restricts further improvement.

This is were other solid-state laser concepts with advanced active medium geometries, including the thin disk [10], the Innoslab [11] and the fiber [12, 13], excel. All of them feature an improved thermal management, and are therefore, compared to classic bulk-amplifier-technologies, superior in terms of average power, while still preserving an excellent spatial beam quality - even in the femtosecond-pulse regime [14, 15]. On the contrary, they still face serious obstacles when to be pushed to even higher peak or average powers [16]. In fibers, for instance, the tight transverse confinement of the optical pulses over considerable lengths eventually results in nonlinear pulse distortions and damage. Thus, to generate pulses with high energy and, consequently, high peak powers, fibers with large mode-field areas [17] in combination with a chirped-pulse amplification-scheme (CPA) [18, 19] are employed. State-of-the-art grating-based stretchers allow to temporally extend femtosecond pulses up to a duration of several nanoseconds and have enabled fiber-based systems to produce pulse peak powers of up to $3.8\,\text{GW}$ and pulse energies of up to $2.2\,\text{mJ}$, respectively [20]. In principle, the stretched pulse duration could be further increased but in practice it is limited to about $10\,\text{ns}$ by the footprint of the laser system and the available grating sizes. However, using a 60-ns pulse, generated by a Q-switched oscillator, already allowed for the extraction of $26\,\text{mJ}$ from a single state-of-the-art Yb-doped fiber [21]. Hence, broadband pulses supporting femtosecond duration and containing an energy in the >20-mJ-regime might be extracted from a single fiber.

To exhaust this potential without the need to increase the grating size, temporally separated amplification can be used and suitable schemes emerged over the last decades. These techniques aim to distribute the pulse energy as equally over time as possible. The most straight forward of such approaches is called divided-pulse-amplification (DPA), wherein each pulse is split temporally into a train of pulses via birefringent crystals [22], or via a combination of beam splitters and free-space delay lines [23, 24]. Subsequently, the individual lower-intensity pulses are amplified and, finally, coherently recombined in time. DPA is an established method to scale the pulse energy by about one order of magnitude [25]. However, increasing the number of pulse replicas to 100 or even 1000 using DPA approaches will

become extremely challenging due to the required number and length of the delay lines, their individual stabilization and the necessary mitigation of saturation effects in the amplifier [26]. Therefore, an interesting alternative to DPA is to start with a higher repetition rate and to use only one delay line for stacking hundreds or even thousands of pulses. Such a delay line can be realized in the form of a passive enhancement cavity [27, 28].

Enhancement cavities are passive resonators, consisting of mirror arrangements without any transmissive elements and, therefore, ideally suited for handling highest laser powers. Intra-cavity average powers of up to 670 kW at enhancement factors of up to 2000 were achieved using 10-ps pulses, stacked a 250-MHz cavity [29]. To date, such cavities were primarily used for the generation of short-wavelength radiation via intracavity high-harmonic generation [30–32] or inverse Compton scattering [33]. The concept addressed during this thesis is called stack-and-dump (SnD) and employs a very similar enhancement cavity with the substantial modification, that the pulses are coupled out of the cavity after a certain number of round-trips to make them available for applications outside of the resonator. This already states the key challenge of the concept: finding a suitable switch to enable extraction of the pulses from the cavity. SnD allows to convert repetition rate to pulse-energy at an un-altered average power. In general, this technique might be applied to any existing amplifier technology. However, it is particularly well-suited for amplifier geometries that can deliver medium pulse energies at high repetition rates, such as fiber-based systems. Although the generation of cavity-dumped enhanced pulses has been demonstrated in the past for low-power systems [34–36], the combination of today's high-average power femtosecond laser systems [37] together with state-of-the-art enhancement cavities [38] promised to enable a new class of laser output parameters. In a first experimental step as a part of this thesis, the potential of SnD cavities employing an acousto-optic modulator as a switching device was exhausted [39]. This required to scale the length of the cavity and face the therewith uprising challenges. As a result, the output energy from such a SnD cavity was increased by almost three orders of magnitude compared to the state-of-the-art before this thesis. To evaluate the power scalability of SnD further, the highest enhancement, pulse energy and average power levels in such a long cavity were demonstrated with chirped ultrashort pulses. Additionally, the mentioned key challenge of extracting the enhanced pulses from the cavity was addressed by investigating novel switching technologies to evaluate their value for SnD, eventually identifying one particularly interesting candidate [40].

This thesis is structured as follows. Chapter 2 introduces the fundamentals of ultrashort laser pulses and different pulse-stacking techniques. Chapter 3 explains how enhancement cavities can be utilized as pulse-stacking devices and what is to be taken care of, in order

to do so. In chapter 4 the results of the stack-and-dump experiments carried out within the scope of this thesis are presented, while chapter 5 presents the theoretical and experimental work on novel switching technologies. Finally, the most important results of this thesis are summarized and a brief outlook is given in chapter 6.

2. Properties of Laser Pulses

This chapter aims to cover the basic physical concepts this thesis is based upon. It gives a brief introduction to the origin and properties of ultrashort laser pulses, briefly explaining limitations in regards to pulse-peak power. Furthermore, it explains interference and the influence of temporal pulse distortions on it. Additionally, the mathematical description of enhancement cavities is given, before a section about cavity-dumping techniques finishes this chapter.

2.1. Ultrashort Laser Pulses

2.1.1. Temporal Description

As shown in [41], a laser pulse, propagating in z-direction, can be separated in a longitudinal $E(z,t)$ and a transversal part $T(x,y)$ as follows:

$$E(x,y,z,t) = T(x,y)E(z,t) \ . \tag{2.1}$$

The first section will focus on the temporal part $E(z,t)$, which describes the absolute value of the longitudinal fraction of such a pulse. A mode-locked pulse [42] can be described as the superposition of plane waves with different frequencies ω:

$$E(z,t) = \int_{-\infty}^{\infty} \tilde{E}(\omega) \exp\left[\mathrm{i}\left(\omega t - k(\omega)z\right)\right] \mathrm{d}\omega \ . \tag{2.2}$$

$k(\omega) = \omega n(\omega)/c$ is the z-component of the wave-vector, c the speed of light, $\tilde{E}(\omega)$ is the electric field, $n(\omega)$ the refractive index of the medium the light is propagating in, and i the imaginary unit. If the oscillation of the carrier frequency at ω_0 is extracted from the integral and an arbitrary shaped spectral phase $\phi(\omega)$ is introduced, one can rearrange Eq. 2.2 to:

$$E(z,t) = \exp(\mathrm{i}\omega_0 t) \int\limits_{-\infty}^{\infty} \tilde{E}(\omega) \exp\left\{\mathrm{i}\left[(\omega - \omega_0)\,t - k(\omega)z\right]\right\} \exp\left[\mathrm{i}\phi\left(\omega\right)\right]\,\mathrm{d}\omega\,. \tag{2.3}$$

In order to carry out the required simulations for the presented experiments, the following description in the temporal and spectral domain suffices:

$$E(t) = E_0(t)\exp\left[\mathrm{i}\left(\omega t + \phi(t)\right)\right] \quad \overset{\text{FT}}{\to} \quad \tilde{E}(\omega) = \tilde{E}_0(\omega)\exp\left[\mathrm{i}\left(\omega t + \phi(\omega)\right)\right]\,. \tag{2.4}$$

These two equations describe the field in the temporal and in the spectral domain. Both are connected via Fourier-transformation (FT). This allows to calculate the development of a certain electrical field during a propagation, by simply adding the necessary phase terms stepwise in the respective regime. If phasesin both domains, spectral and temporal need to be taken into account, the so-called split-step algorithm can be employed to easily calculate the field after all phase influences during propagation, were considered [43]. Introducing ϵ_0 as the dielectric constant, the temporal power distribution of such a field is given by the multiplication of $E(t)$ with the complex-conjugated field $E^*(t)$ [41]:

$$P(t) = \frac{c\epsilon_0}{2}E(t)E^*(t)\,. \tag{2.5}$$

The temporal power distribution crucially depends on the shape and duration of the pulse. A short pulse duration is often favored to maximize the peak power. For a spectral distribution $\tilde{E}(\omega)$ with the full-width-at-half-maximum (FWHM) spectral bandwidth of $\Delta\omega$, the achievable FWHM-pulse duration Δt, the so-called Fourier-limit, is given by [41]:

$$\Delta t \cdot \Delta\omega = \text{TBW}\,. \tag{2.6}$$

Herein TBW is the time-bandwidth product, a constant that solely depends on the pulse shape. For a Gaussian pulse

$$P(t) = P_0 \exp\left[-4\ln(2)\left(\frac{t - t_0}{\Delta t}\right)^2\right]\,, \tag{2.7}$$

with pulse-peak power $P(t = t_0) = P_o$, it is 0.44. The energy E_p contained in such a pulse can be calculated using the average power of the laser system $\bar{P}$ and its repetition rate

$f_{\text{rep}} = 1/T$, or via the integral over the power distribution of a single pulse as follows:

$$E_{\text{p}} = \bar{P}T = \frac{\bar{P}}{f_{\text{rep}}} = \int_{-\frac{T}{2}}^{\frac{T}{2}} P(t)\,\mathrm{d}t \ .$$

(2.8)

The connection between those values is also shown visually in Fig. 2.1.
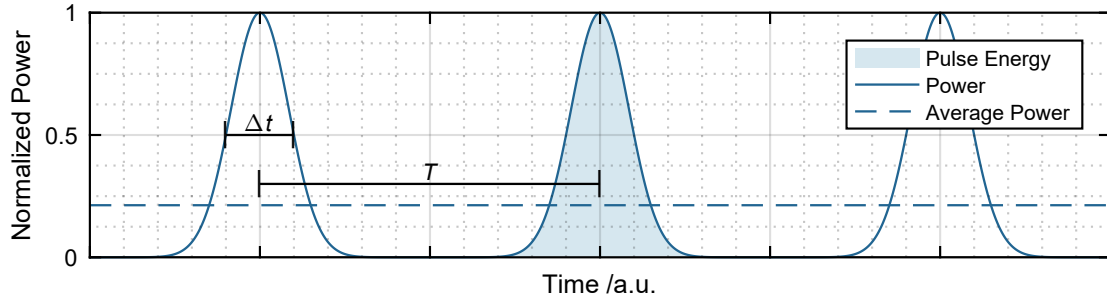
Figure 2.1.: Visual explanation of laser output parameters. The power is normalized to the pulse-peak power.

In case of a Gaussian pulse, the often interesting parameter pulse peak power can be calculated as:

$$P_0 \approx 0.94\frac{E_{\text{p}}}{\Delta t} \ .$$

(2.9)

2.1.2. Carrier-Envelope-Offset and Frequency-Combs

The envelope of a pulse describes the development of the electrical field amplitude. However, the exact temporal shape of the field within the pulse depends on a frequency-independent, constant phase ϕ_{ceo}. This phase has no impact on the envelope but influences the position of the peak of the oscillating electrical field (red) relative to the peak of the envelope (blue) as shown in Fig. 2.2. It is commonly called carrier-envelope-offset and can, depending on the system, stay static, drift slowly, or even jump randomly. The change of ϕ_{ceo} is $\phi_{\text{cep}} = \Delta\phi_{\text{ceo}}$ and called carrier-envelope-phase (CEP) and describes how the CEO changes in between two round-trips. For the application of few-cycle pulses, CEO and CEP can be very critical parameters, that have to be controlled. It is noteworthy, that a stable CEO always implies a stable CEP (equally zero), but not vice versa. Stabilizing the CEO of a system is therefore a harsher requirement. For pulses with a large number of optical cycles both parameters are usually irrelevant, since CEO differences do not introduce significant changes to the field

maximum. If a multitude of longer pulses are to interact with each other, however, the CEO gains a certain amount of importance as it will be shown in Sec. 2.2.
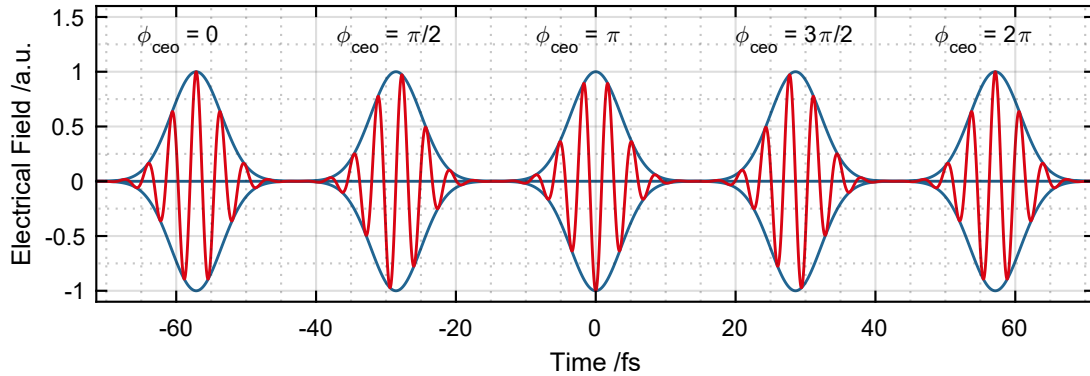
Figure 2.2.: Depiction of pulses with $\Delta t = 6\,\text{fs}$ at $1040\,\text{nm}$ central-wavelength and with different Carrier-Envelope Offsets ϕ_{ceo}. If this example was a pulse train, its CEP would be $\phi_{\text{cep}} = \pi/2$.

Fig. 2.2 shows the shape of the electrical field and its envelope for different CEOs. For $\phi_{\text{ceo}} \neq 2k\pi$ ($k \in \mathbb{Z}$) the maximum of the electrical field is lower than the maximum of the envelope, which can be detrimental for applications of few-cycle pulses. However, after a certain number of pulses, the pulse shape, and therewith the CEO, repeats itself. The frequency of this phase change is commonly called carrier-envelope-offset-frequency [44]:

$$\omega_{\text{ceo}} = 2\pi f_{\text{ceo}} = \frac{2\pi}{T_{\text{ceo}}} = \phi_{\text{ceo}} f_{\text{rep}} \,, \tag{2.10}$$

where T_{ceo} describes how much time passes by, before the pulses are identically shaped again. If a laser pulse is to be depicted in the spectral domain, this can be done as a frequency comb. A so-called optical frequency comb is a certain optical spectrum which consists of typically equidistant optical frequency components. The intensity of such comb lines often varies substantially. As shown in Fig. 2.3, the CEO-frequency shifts the entire frequency comb of the pulse (see Fig. 2.3) [45].
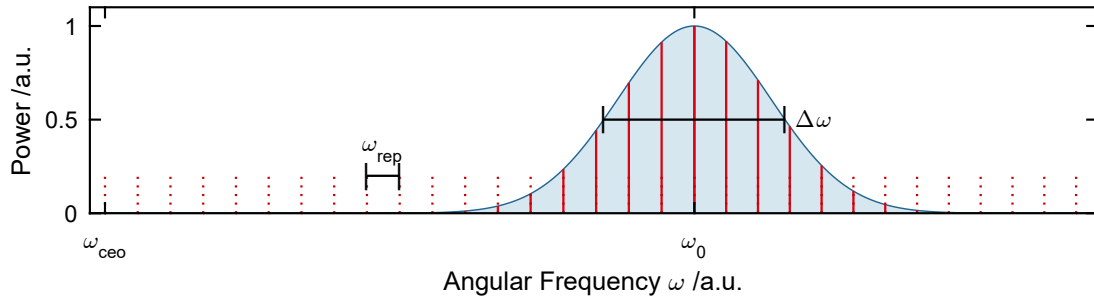
Figure 2.3.: Schematical depiction of the frequency comb of a fs-laser pulse with $\omega_{\text{rep}} = 2\pi f_{\text{rep}}$ and $\Delta\omega$ being the FWHM spectral bandwidth.

Using $\omega_{\text{rep}} = 2\pi f_{\text{rep}}$, the frequency comb of a mode-locked laser, consisting of the resonant frequencies ω_{m} with $m \in \mathbb{N}$ can be written as [46]:

$$\omega_m = m\omega_{\text{rep}} + \omega_{\text{ceo}} = m\omega_{\text{rep}} + \phi_{\text{ceo}}\omega_{\text{rep}} \; . \tag{2.11}$$

However, there are further sources of additional temporal or spectral phases a laser pulse can acquire while propagating in a medium, such as dispersion or non-linear effects, for example.

2.1.3. Dispersion

A materials response on electromagnetic waves is usual depending on the wavelength i.e. the frequency ω of the wave. Therefore, the refractive index can be expressed as $n = n(\omega)$. The wave-number k and the refractive index are connected by [43]:

$$k(\omega) = n(\omega)\frac{\omega}{c} \; . \tag{2.12}$$

This relationship can be approximated by a Taylor series around the central-frequency ω_0

$$k(\omega) = \underbrace{k(\omega_0)}_{\beta_0} + \underbrace{\left(\frac{\mathrm{d}k}{\mathrm{d}\omega}\right)\Big|_{\omega_0}}_{\beta_1}(\omega - \omega_0) + \frac{1}{2}\underbrace{\left(\frac{\mathrm{d}^2k}{\mathrm{d}\omega}\right)\Big|_{\omega_0}}_{\beta_2}(\omega - \omega_0)^2 + \frac{1}{6}\underbrace{\left(\frac{\mathrm{d}^3k}{\mathrm{d}\omega}\right)\Big|_{\omega_0}}_{\beta_3}(\omega - \omega_0)^3 + \dots \; .$$

The Taylor-coefficients β_n allow to describe different aspects of the dispersive wave:

$$\text{Phase velocity:} \quad v_{\mathsf{ph}} = \frac{\omega_0}{\beta_0} = \frac{\omega_0}{k(\omega_0)} \tag{2.13}$$

$$\text{Group velocity:} \quad v_{\mathsf{gr}} = \frac{1}{\beta_1} = \left(\frac{\mathrm{d}k}{\mathrm{d}\omega}\right)^{-1}\bigg|_{\omega_0} \tag{2.14}$$

$$\text{Group velocity dispersion (GVD):} \quad \beta_2 = \left(\frac{\mathrm{d}^2 k}{\mathrm{d}\omega}\right)\bigg|_{\omega_0} \tag{2.15}$$

$$\text{Third order dispersion (TOD):} \quad \beta_3 = \left(\frac{\mathrm{d}^3 k}{\mathrm{d}\omega}\right)\bigg|_{\omega_0} \tag{2.16}$$

While β_0 and β_1 describe the propagation of carrier and envelope, they have no effect on the temporal pulse shape. The higher-order dispersion terms cause a deviation in propagation velocity of the different frequency components. Due to this deviation, the superposition of the fields creates a temporally broadened pulse. When the β_2-term shifts the high frequencies towards the pulse end, the pulse is called 'up-chirped'. If it shifts the low frequencies to the pulse end it is called 'down-chirped'. The β_3-term alters the pulse shape as well, but other than β_2, asymmetrically. Third and higher order dispersion is especially important for the treatment of few-cycle pulses, due to their large bandwidth.

2.1.4. Self-Phase-Modulation

Whenever an electrical field propagates through a medium, it polarizes this medium. The polarization $\mathcal{P}(\omega)$ is not necessarily linearly proportional to the incident field $E(\omega)$, but fulfills the equation:

$$\mathcal{P}(\omega) = \epsilon_0 \left[\chi^{(1)} \cdot E(\omega) + \chi^{(2)} : E^2(\omega) + \chi^{(3)} \vdots E^3(\omega) + \dots \right]. \tag{2.17}$$

Herein, ϵ_0 is the electric field constant and $\chi^{(m)}$ is the m-th order of the susceptibility tensor. For small field-strengths, Eq. 2.17 can be approximated by $\mathcal{P}(\omega) = \epsilon_0 \chi^{(1)} E(\omega)$. For higher intensities however, the higher order terms are of increasing importance. There is a plethora of nonlinear effects resulting from this, but this section is focused on those caused by $\chi^{(3)}$, which are the dominant effects in glass [47]. The refractive index $\tilde{n}$ has a part, that depends on the intensity of the electric-field interacting with it. For increased field intensities, this part becomes increasingly significant and consequently $\tilde{n}$ deviates from n. This can be expressed as [43]:

$$\tilde{n} = n(\omega) + n_2 I \quad \text{with} \quad n_2 = \frac{3\chi^{(3)}}{8n(\omega)} \tag{2.18}$$

and is called temporal Kerr-effect. As a result of the intensity dependence of the refractive index, the pulse acquires an additional phase when propagating through a medium of length l:

$$\phi_{\mathsf{spm}} = -\delta n \cdot l\frac{\omega_0}{c} \quad \text{with} \quad \delta n = n_2 I \,. \tag{2.19}$$

Consequently, this phase is intensity dependent and hence the temporal shape of the pulse is changed. This effect is called self-phase modulation (SPM). The maximum phase collected by the peak of the pulse while propagating through a medium is commonly referred to as 'B-integral' and can be calculated as

$$B = \frac{2\pi}{\lambda} \int_{z=0}^{l} n_2 I_0(z) \, \mathsf{d}z \,, \tag{2.20}$$

with $I_0(z)$ being the peak intensity of the pulse depending on the position z in the medium. The B-integral is often used to estimate the magnitude of nonlinear-pulse distortions acquired by a laser pulse during its propagation.

2.1.5. Spatial Description

The transversal part $T(x, y)$ of the electrical field in Eq. 2.1 describes the spatial field distribution and is for Gaussian beams given by

$$I(x, y) = \frac{c\epsilon_0}{2}T(x, y)T^*(x, y) = I_0\mathsf{exp}\left[-2\left(\frac{x^2 + y^2}{w^2}\right)\right] \,. \tag{2.21}$$

Wherein $2w$ is the full width of the beam at $1/e^2$ of the peak-intensity I_0 often also called beam diameter $d = 2w$. The peak intensity of a laser pulse with a circular beam profile is given by [48]:

$$I_0 = \lim_{r \to 0} \frac{P_0\left[1 - \mathsf{exp}\left(\frac{-2r^2}{w^2}\right)\right]}{\pi r^2} = \frac{2P_0}{\pi w^2} \,. \tag{2.22}$$

For elliptically shaped beams with $d_x = 2w_x$ and $d_y = 2w_y$ the following equation is valid, respectively:

$$I_0 = \frac{2P_0}{\pi w_x w_y} \ . \tag{2.23}$$

2.2. Interference of Femtosecond Pulses

As discussed in the previous sections, a laser-pulse as described in Eq. 2.4 may contain different temporal and spectral phases. If two pulses are to be superposed, depending on the difference between the individual phases, the temporal interference pattern can vary between complete constructive or complete destructive interference. For an optimum combining efficiency (e.g. completely constructive interference), all parameters need to be identical. Therefore, in order to overlap two maxima the central frequency ω_0, the absolute phase offset ϕ_0, the carrier-envelope-offset ϕ_{ceo}, the nonlinear phase ϕ_{spm} and the phase due to dispersion ϕ_{disp} as well as the peak power $P_0 \propto E_0$ have to be matched. Any deviation between those parameters will typically result in a decreased efficiency and is hence not desirable in most scenarios.
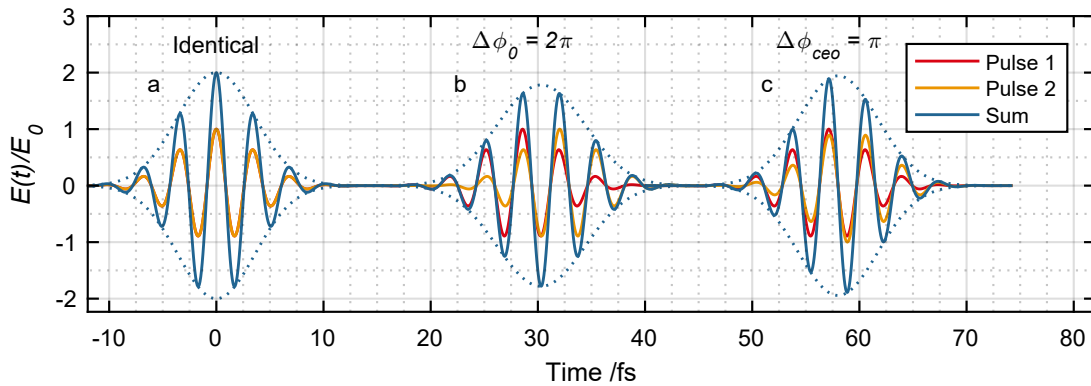
Figure 2.4.: Field and envelope of individual pulses and their superposition in the case of (a) two identical fs-pulses, (b) two pulses temporally misaligned by exactly one wavelength (c) two fs-pulses with a CEO-difference of π, but also shifted to have a matching field maxima position. The initial pulse duration is $6\,\mathrm{fs}$ at a central wavelength of $\lambda_0 = 1040\,\mathrm{nm}$.

In Fig. 2.4 some cases that are relevant for the experiments presented in this thesis are depicted. The temporal interference pattern of the fields as well as the resulting intensity is shown for two temporally perfectly matched and identical pulses, two pulses temporally misaligned by $\Delta\phi_0 = 2\pi$ and two pulses with a CEO-mismatch of $\Delta\phi_{ceo} = \pi$, but realigned for optimum constructive interference. Similar effects occur for pulses that differ in terms of

dispersion and nonlinear phases as explained in [49]. For a better visibility, this plot shows the effects using few-cycle pulses. For a longer pulse duration, as used in the later presented experiments, they become significantly weaker. However, for larger numbers of interacting pulses, their impact grows significantly. Fig. 2.5 depicts this in the case of of 200 identical 700-fs pulses with a phase slip of exactly $2k\pi \,\hat{=}\, k\lambda$ between each two subsequent pulses (equivalent to Fig. 2.4b). Obviously, even though the pulses are much longer, the effects are strongly visible due to the high number of interacting pulses. Even a misalignment of only one wavelength reduces the peak power of these 200 superposed pulses by $20\,\%$ from 200 to 160. It is therefore clear, that for the highest peak power enhancement, the fields have to be matched perfectly.
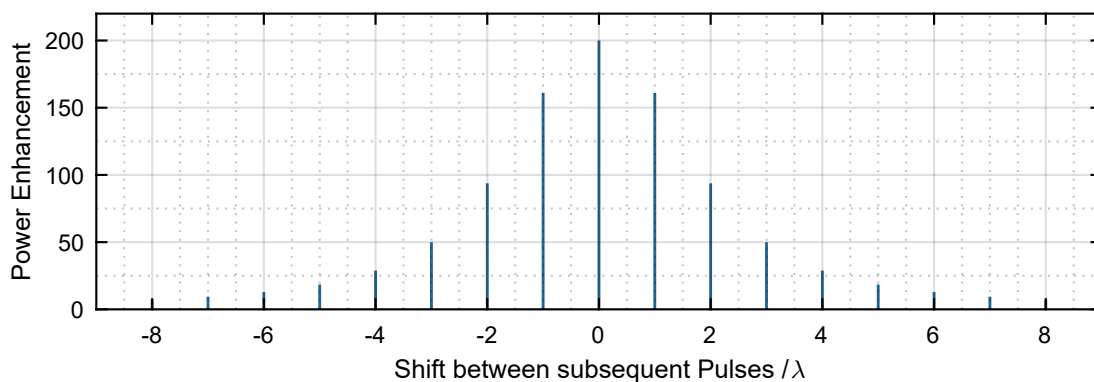
Figure 2.5.: Coherent superposition of 200 pulses with a duration of $700\,\mathrm{fs}$ and shifted by $k\lambda$ between two subsequent pulses for different values of k.

2.3. Concepts to circumvent amplifier limitations

2.3.1. Ultrafast Laser Amplifier Technologies

Even restricted to laser amplifiers for ultrashort pulses, there is a multitude of vastly different technologies varying significantly in the geometry of the active medium and the entire resulting amplifier design. Some are optimized to minimize the occurring peak-intensities, like multi-stage bulk-geometries [50], some are optimized for high-average power operation, like Innoslabs [11] or fibers [14, 51]. Optimizing a single amplifier setup for both is virtually impossible and trade-offs have to be made. Figure 2.6 shows an overview of the achieved laser output parameters with different ultrafast amplifier technologies to this date. Each data point represents one particular published experimental result. Naturally, mapping all

published experiments is not feasible, hence, only the most distinguished ones, extending each technologies range and some historical landmarks, are depicted.
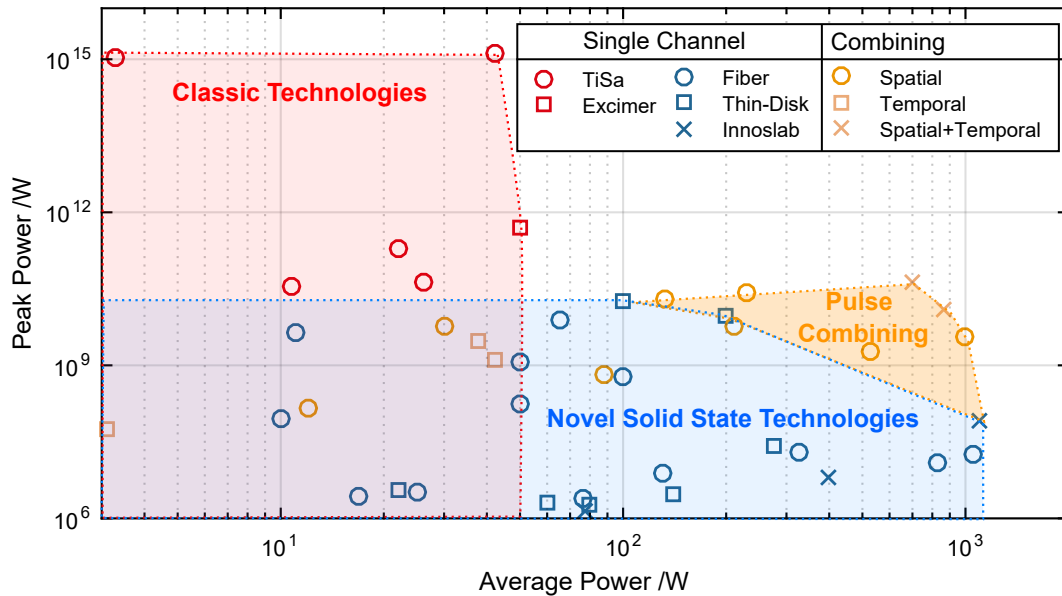
Figure 2.6.: Overview of the pulse-peak and average power of significant publications presenting the generation of laser-pulses with a duration of $\leq 1\,\mathrm{ps}$ achieved with different laser technologies (Ti:Sapphire: [50, 52], Excimer: [53], Fiber: [14, 20, 51] Thin-Disk: [54, 55], Innoslab: [11], Spatial Combining: [37, 56–59], Temporal Combining: [24, 60], Spatial+Temporal: [25]).

The biggest leap in pulse-peak power was achieved, when the chirped-pulse-amplification (CPA) approach was first adapted to optical applications in 1985 [61]. Ever since, CPA is an indispensable part of almost every fs-laser system. Similarly, developing novel solid-state laser technologies with optimized thermal properties, e.g. fiber, Innoslab or thin-disk amplifiers, allowed to improve the achievable average power in ultrafast-systems up to $\sim 1\,\mathrm{kW}$ [51]. Moreover, cw-fiber-amplifiers can even deliver up to $4.3\,\mathrm{kW}$ of average power (single-mode) [62] or $> 100\,\mathrm{kW}$ (multi-mode) [63]. Despite all this progress, CPA-systems are limited by size and cost of the gratings and even the thermally optimized laser geometries suffer from thermal effects eventually [64–66]. Hence, to further scale the laser output parameters, beam or pulse combining is of paramount importance [67]. The remaining sections of this chapter will explain the concepts and operating principles of spatial and temporal combining techniques.

2.3.2. Spatial Pulse Combining

Whenever any technology approaches its intrinsic limitations or further scaling is unreasonably difficult, parallelization offers a straight-forward solution to still achieve increased functionality [68]. Over the last two decades, this was adapted to laser amplifiers [67, 69, 70], where a seed signal is split into M-channels before the last amplifier stage and recombined after amplification, hence increasing the possible output average and peak power by a factor of $\eta_{\mathrm{spc}}M$, where η_{spc} accounts for the combining efficiency. Figure 2.7 depicts such a setup. This is also referred to as 'spatially separated amplification' or 'coherent beam combining'. State-of-the-art setups deliver 200-fs pulses containing $1\,\mathrm{mJ}$ of energy at $\sim 1\,\mathrm{kW}$ of average power (see Fig. 2.6). It is noteworthy that there are also concepts that make use of incoherent combining approaches, but they are not employable in femtosecond-laser systems and will be neglected in this work [71].
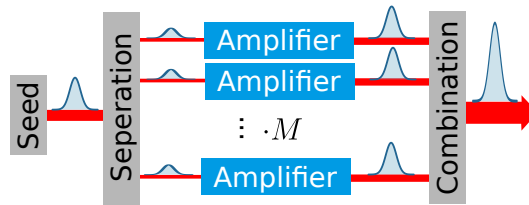
Figure 2.7.: Concept of spatially separated amplification.

2.3.3. Temporal Pulse Combining
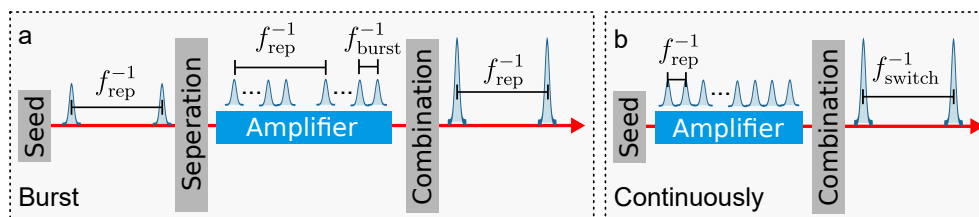
Figure 2.8.: The two different approaches on temporally separated amplification.

In opposition to spatially separated amplification, in a temporal combining setup only one amplifier channel is used but in order to minimize the pulse-peak power in the amplifier the pulse energy is distributed more equally over time by temporally separating the pulses prior amplification (see Fig. 2.8). The goal is to artificially increase the stretched pulse duration in order to minimize peak power effects during the critical last amplification step. Two

fundamentally different approaches can be employed. The first method (Fig. 2.8a) is to use a signal at the repetition rate f_{rep}, split it into a burst of N pulses at f_{rep} with the intra-burst repetition rate of f_{burst}, amplify it and afterwards recombine the burst to the original pulse pattern. The second method (Fig. 2.8b) starts with a high-repetitive oscillator and coherently stacks N pulses and recombines them, in order to generate an output signal with $f_{switch} = f_{rep}/N$. Each of the following approaches classifies into one of these categories.
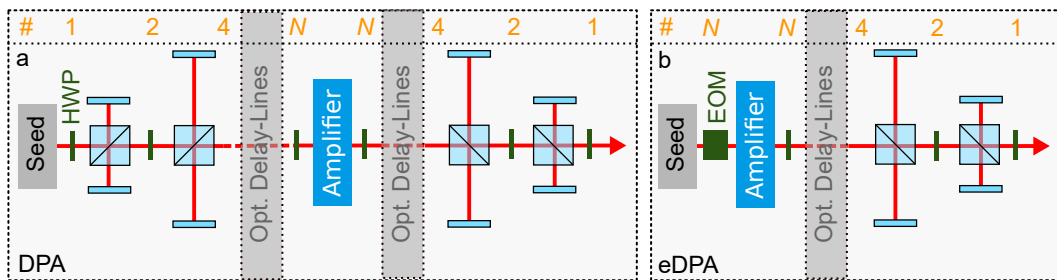
Figure 2.9.: Schematic setup of a) DPA and b) eDPA. The top bar shows the pulse number (orange) at each part of the setup. Additional optional delay lines can be added to increase the number of pulse replicas. Using n delay-lines allows to distribute the energy to N pulse replicas.

Divided-Pulse-Amplification (DPA)   The straight forward approach for a burst-type temporal combining setup is divided-pulse-amplification (DPA) [22]. Here, n cascaded delay lines are used to split a pulse into $N = 2^n$ temporal replicas using polarization, amplify and recombine them vice versa, employing n-combining stages (see Fig. 2.9b). In combination with spatial combining, such a scheme allowed to achieve up to 12-mJ pulse energy at 700-W average power [25]. However, since the pulses of this burst each see different inversion-levels in the amplifier, their gain will differ too, making it necessary to preshape the burst. Therein lies the current limitation of such approaches, since this shaping can only optimize for the amplitude or the B-integral and the combining efficiency will consequentially drop significantly for a growing number of division stages as thoroughly investigated and explained in [26]. Additionally, the fractions of the pulses that are not combined will remain as pre- and post-pulses in the output channel, making a later contrast optimization unavoidable for most applications.

Electronically Divided-Pulse-Amplification (eDPA)   In this novel approach [72], the combination scheme is identical to DPA but the separation is done vastly different (see

Fig. 2.9b). Contrary to DPA, eDPA starts with a continuously pulsed signal out of an oscillator. Since the power level is very low at this point of the setup, an electro-optic modulator (EOM) can be used to cut out N pulses and impress the same polarization pattern that this pulse train would have had after the classical DPA delay-lines. Afterwards, the pulses are amplified and recombined identically to the classical DPA scheme. This simplifies the first part of the setup significantly and can theoretically allow to compensate better for the gain effects. If these potential benefits can be underlined experimentally, is yet to be shown.

Both, DPA and eDPA are increasingly complex for higher pulse numbers, since the number of delay lines needs to grow accordingly with $n = \sqrt{N}$. This is circumvented in the following scheme, by using only a single delay-line.
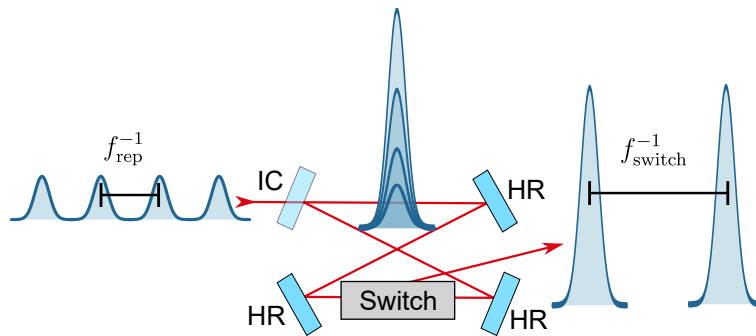
Figure 2.10.: Schematic of the stack-and-dump concept. [28].

Stack-and-Dump (SnD)   This dissertation is based upon a concept called stack-and-dump, which was first proposed theoretically in 2002 [27] and later demonstrated experimentally for low power levels [34–36]. Instead of multiple delay lines like DPA, SnD only employs a single delay line to stack a continuous train of pulses as shown in Fig. 2.10. This delay-line is simply an enhancement cavity, seeded with the pulses delivered from the main-amplifier of a high repetition rate laser system. The length of the cavity matches the distance between two subsequent pulses. For example, if seeded with a 10-MHz pulse train, the cavity will be $\sim 30\,\mathrm{m}$ long, so that the electrical field of each incoming pulse can constructively interfere with the field in the cavity. To allow for an efficient power transfer to the cavity, an input-coupling mirror with an optimized reflectivity is to be chosen (see Chap. 3). Most enhancement cavities are operated in a so-called steady-state regime (see Sec. 3.2), where the intracavity power level does not change over time. SnD, however, needs to make the enhanced pulses available outside of the cavity, hence the cavity is operated in a non-

steady-state regime (see Sec. 3.3) and a fast switch is necessary to extract the pulses (see Sec. 3.5).

SnD offers a number of advantages compared to DPA and eDPA. First, it only needs one combination stage, a passive cavity. Second, it amplifies a continuous pulse train and not a burst of pulses, hence, no pulse separation stage is needed and the pulses do not see any saturation effects in the amplifier. Therefore, neglecting small temporal fluctuations, they all have the same nonlinear phase and amplitude when entering the cavity. Third, no parasitic pre- or post-pulses are extracted from the cavity and amplified-spontaneous emission (ASE) is not coherent enough to be enhanced in the cavity, hence the contrast of the output is superior to all other temporal combining techniques. As a trade-off, a large number of subsequent incoming pulses from a mode-locked oscillator need to be stacked. This is challenging, since the pulses coming from an oscillator usually vary slightly over time in terms of the temporal shape and phases they have. This variation needs to be minimized in order to achieve a stable constructive interference during the cavity build-up. The theoretical fundamentals of these concepts are thoroughly analyzed in the following Chap. 3, including the key challenge of finding a suitable switch to extract the stacked pulses from the cavity (Sec. 3.6).
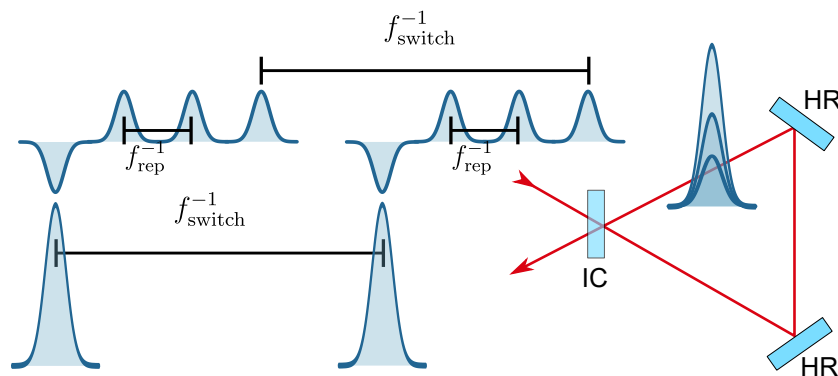
Figure 2.11.: Schematic of the GTI concept [73].

Gires-Tournois Interferometer like Cavities (GTI-Cavities)   On one hand, GTI-cavities are a modified version of SnD while on the other hand, they are more similar to DPA. GTI-cavities offer an elegant solution for the extraction of the stacked pulse from the enhancement cavity, by shifting the phase of the last pulse in the incoming pulse train by π, to force constructive interference on the outside of the input-coupling mirror, instead of inside the cavity [73]. However, this method forces some trade-offs. First, the extraction is also done via the input-coupling mirror, which can only be optimized for either stacking or extracting.

This leads to a limitation of the number of pulses that can be stacked efficiently in one cavity to around 10 [74]. To increase the enhancement beyond that, further cavities have to be added in a cascaded setup, similar to the delay-lines in DPA. Second, GTI-cavities amplify bursts of pulses, leading to saturation effects in the amplifiers, which eventually results in a decreased combining efficiency of the pulses. Third, such imperfect temporal combining leads to strong pre- or post-pulses that contain a considerable amount of energy ($\sim 50\,\%$) in the so far demonstrated experiments [75]. However, GTI-cavities are of a very low finesse, which leads to relaxed demands on the stabilization and adjustment and impressive output parameters have been demonstrated recently [75]. A detailed explanation of GTI-cavities is given in the dissertation by T. Zhou [74].

3. Enhancement Cavities

While constructive interference is the key mechanism enabling the build-up of high intense pulses in any resonator, it also demands certain design criteria from such resonators. Optical resonators or cavities can be set up either in a linear, or ring design. This entire thesis will solely focus on ring-cavities and this chapter describes the working principles of such passive resonators and how to optimize them for the stacking of femtosecond laser pulses.

3.1. Optical Design of Passive Resonators

3.1.1. Stability of Resonators

Along with the stacking of a higher number of pulses in a passive resonator, a certain stability on the propagation behaviour of the beam is required, so that the spatial beam profile can be reproduced after each round-trip. To define a suitable stability criterion, one usually employs the principles of Gaussian optics, which are valid in the paraxial approximation. Therein

$$\mathcal{M}_{\mathsf{c}} = \begin{pmatrix} A_{\mathsf{c}} & B_c \\ C_{\mathsf{c}} & D_{\mathsf{c}} \end{pmatrix} = \mathcal{M}_{\alpha} \cdot \ldots \cdot \mathcal{M}_2 \cdot \mathcal{M}_1 \tag{3.1}$$

is defined as the transfer matrix of a ring-cavity consisting of α-elements with the starting point between the 1st and the αth element and $\mathcal{M}_j$ being the transfer matrix of the j-th element. Furthermore, the so-called q-parameter can be introduced as [76]:

$$\frac{1}{q(z)} = \frac{1}{R_{\mathsf{c}}(z)} - \frac{i\lambda_0}{\pi w^2(z)}, \tag{3.2}$$

with $R_{\mathsf{c}}(z)$ being the radius of curvature of the beam and $w(z)$ the beam radius. The development from $q_1 = q(z_1)$ to $q_2 = q(z_2)$ during the propagation from z_1 to z_2 can then be calculated via

$$q_2 = \frac{Aq_1 + B}{Cq_1 + D}, \tag{3.3}$$

with $\mathcal{M} = \begin{pmatrix} A & B \\ C & D \end{pmatrix}$ representing the transfer-matrix of all the elements between the positions z_1 and z_2. A resonator is considered 'stable' as long as the criterion [76]

$$|A_{\mathrm{c}} + D_{\mathrm{c}}| \leq 2 \tag{3.4}$$

is fulfilled. The optical stability is a crucial criterion for keeping the effects of small disturbances and misalignment negligible. The cavity is therefore best operated close to the stability center, unless other requirements arise (i.e. large beam diameters to reduce peak powers [77]) . The transfer-matrix allows to calculate the beam-radius w and curvature R_{c} between the first and the last element of the components it includes

$$R_{\mathrm{c}} = \frac{2B}{D - A} \quad \text{and} \quad w = \sqrt{\frac{2\lambda |B|}{\pi \sqrt{4 - (A + D)^2}}}. \tag{3.5}$$

This enables straight forward calculation of the beam size $w(\mathrm{IC})$ and curvature $R_{\mathrm{c}}(\mathrm{IC})$ at the input-coupling mirror (IC) of an enhancement cavity, when all the elements and distances in the cavity are known and $\mathcal{M}_{\mathrm{c}}$ is chosen with the position of the IC as a starting point. One example for that is given in the Appendix (Sec. A.2). It is noteworthy, that at extremely high power levels, thermal effects in the mirrors can have a significant impact on the caustic and appropriate countermeasures need to be applied [78, 79].

3.1.2. Transverse Optical Resonator Modes

The simple Gaussian beam, as discussed in the last section, is only one of many solutions for the paraxial wave equation. Using Hermite polynomials H_n and H_m $(n, m \epsilon \mathbb{N})$, the general solution can be expressed as [76]:

$$\begin{aligned} T_{mn}(x, y, z) = \frac{w_0}{w(z)} H_n \left(\sqrt{2} \frac{x}{w} \right) H_m \left(\sqrt{2} \frac{y}{w} \right) \\ \cdot \exp\left\{ -\left[\mathrm{i}kz - \phi(m, n, z) \right] - \mathrm{i}\frac{k}{2q} (x^2 + y^2) \right\}, \end{aligned} \tag{3.6}$$

where

$$\frac{w_0}{w(z)} = \frac{1}{\sqrt{1 + (z/z_R)^2}} \tag{3.7}$$

and

$$\phi(n, m, z) = (n + m + 1)\arctan(\frac{z}{z_R}) \tag{3.8}$$

is the so-called Gouy phase. The Rayleigh length is therein defined as $z_R = \pi w_0^2/\lambda$. A multitude of resonator modes can oscillate at once, leading to a superposition of the individual modes. While acting as a possible mathematical solution, the shape of these higher order modes makes them usually irrelevant for pulse-stacking in enhancement cavities. It is important, however, to minimize them and to know about the Gouy-phase shift, since it is the reason different modes are resonant at different resonator-lengths, making it easier to separate them from another and only enhance the fundamental mode by matching the resonator-length accordingly. Hence, in experiments, the energy content of the higher order modes is to be minimized by matching the incoming beam to the fundamental mode of the cavity (see section 3.2.4) and by discriminating the higher cavity modes using the resonator length.

3.2. Fundamentals of Steady-State Enhancement

Apart from the spatial mode-shape and stability, there are further important design parameters of enhancement cavities. Choosing the reflectivity of the input-coupling mirror has a strong impact on the cavity efficiency and effectiveness and will therefore be the focus of this upcoming section. First, for classical steady-state, and second, for non-steady-state operation. The entire section will assume that intensity reflection R and transmittance T of the input-coupler are always dominant ($R + T = 1$) and therefore ignore scattering and absorption effects of the input-coupling mirror. While differently arranged, most of the basic concepts are derived similarly to [76].

3.2.1. Field Enhancement in Optical Resonators

A passive optical cavity typically consists of one input-coupling mirror (IC) with an intensity reflectivity R and at least one more mirror, usually with an highly reflective coating. Such a basic cavity setup is shown in Fig. 3.1.
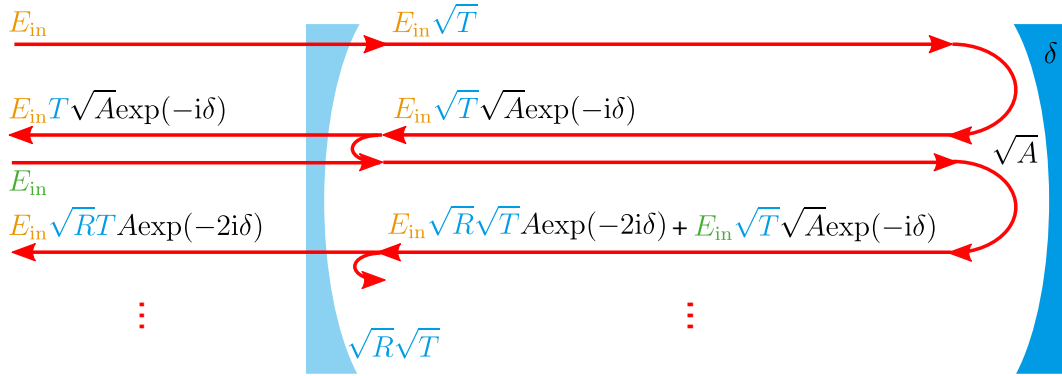
Figure 3.1.: Simple cavity setup consisting of two mirrors. One of which is an input-coupling mirror with reflectivity R and transmittance T. The round-trip attenuation due to other losses is A and the phase-shift per round-trip is δ. E_in is the incoming field.

An electromagnetic-wave E_in is now seeded into the passive resonator through the input-coupler and is being split into a transmitted part $E_\text{in}\sqrt{T}$ and a reflected part $E_\text{in}\sqrt{R}$, with $T = 1 - R$. During each round-trip inside the cavity, an attenuation $\sqrt{A}$ is applied to the field and each reflection on a mirror adds a phase shift δ. If the number of round-trips approaches infinity (for a sufficiently high number of round-trips), the field inside the cavity E_IC can be expressed by

$$
\begin{aligned}
E_\text{IC} &= E_\text{in}\sqrt{T} + E_\text{in}\sqrt{TAR}\exp\left(-\mathrm{i}\delta\right) + E_\text{in}\sqrt{T}AR\exp\left(-2\mathrm{i}\delta\right) + \dots \\
E_\text{IC} &= E_\text{in}\sqrt{T}\left\{1 + \sqrt{AR}\exp\left(-\mathrm{i}\delta\right) + \left[\sqrt{AR}\exp\left(-\mathrm{i}\delta\right)\right]^2 + \dots\right\} \\
E_\text{IC} &= \frac{E_\text{in}\sqrt{T}}{1 - \sqrt{AR}\exp\left(-\mathrm{i}\delta\right)}
\end{aligned}
$$

Hence, the theoretically possible power enhancement factor V (henceforth simply called 'enhancement') can be written as

$$
V = \left|\frac{E_\text{IC}}{E_\text{in}}\right|^2 = \frac{1 - R}{\left(1 - \sqrt{RA}\right)^2} \tag{3.9}
$$

Other important parameters of an enhancement cavity include the free spectral range (FSR), which is, for a dispersion free, ring-cavity defined as [76]:

$$f_{\text{FSR}} = \frac{c}{ns} \, , \tag{3.10}$$

with s being the cavity length and n the refractive index of the medium inside the cavity. If operated in vacuum, n will be unity and can hence be neglected. For the approximation that R and A are close to unity, the width of the resonances is defined as

$$f_{\text{FWHM}} = 2\frac{c}{s} \arcsin\left(\frac{1 - \sqrt{RA}}{2\sqrt[4]{RA}}\right) \approx \frac{1 - \sqrt{RA}}{\pi} f_{\text{FSR}} \, . \tag{3.11}$$

A visual depiction of f_{FSR} and f_{FWHM} is given in Fig. 3.2.
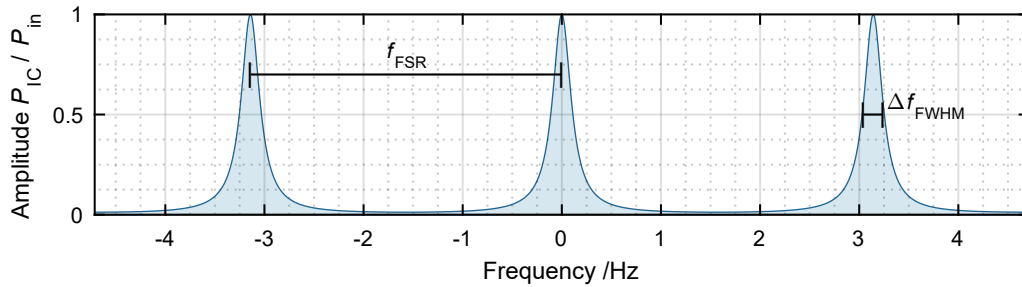
Figure 3.2.: Intracavity spectrum of an empty resonator with $20\,\%$ losses and an input-coupler with $80\,\%$ reflectivity. The frequency difference between two resonances is called free spectral range and is depicted as f_{FSR} chosen to be $\pi\,\text{Hz}$. Δf_{FWHM} is the full width at half maximum value of a resonance peak.

With the help of these quantities, it is common to introduce the finesse $\mathcal{F}$ of the resonator as

$$\mathcal{F} = \frac{f_{\text{FSR}}}{f_{\text{FWHM}}} \approx \frac{\pi}{1 - \sqrt{RA}} \, . \tag{3.12}$$

The finesse gives an estimation of how many pulses will interfere with each other in a cavity with an input-coupler reflectivity R and round-trip attenuation A. In high finesse resonators, the enhancement can be higher and high average and peak powers can build up. Unfortunately, as visible in Eq. 3.12, at a fixed FSR, a growing finesse also leads to a shrinking width of the resonance peaks and, therefore, enhancing a broad spectrum becomes increasingly difficult.

In reality, the entire build-up curve of the energy inside an enhancement cavity and the achievable enhancement not only depends on the losses $L = 1 - A$ and the input-coupler reflectivity R, but also on the amount of intracavity dispersion and nonlinear-phases (see Fig. 3.3).

3.2.2. Influence of Dispersion and Nonlinear Effects on Enhancement
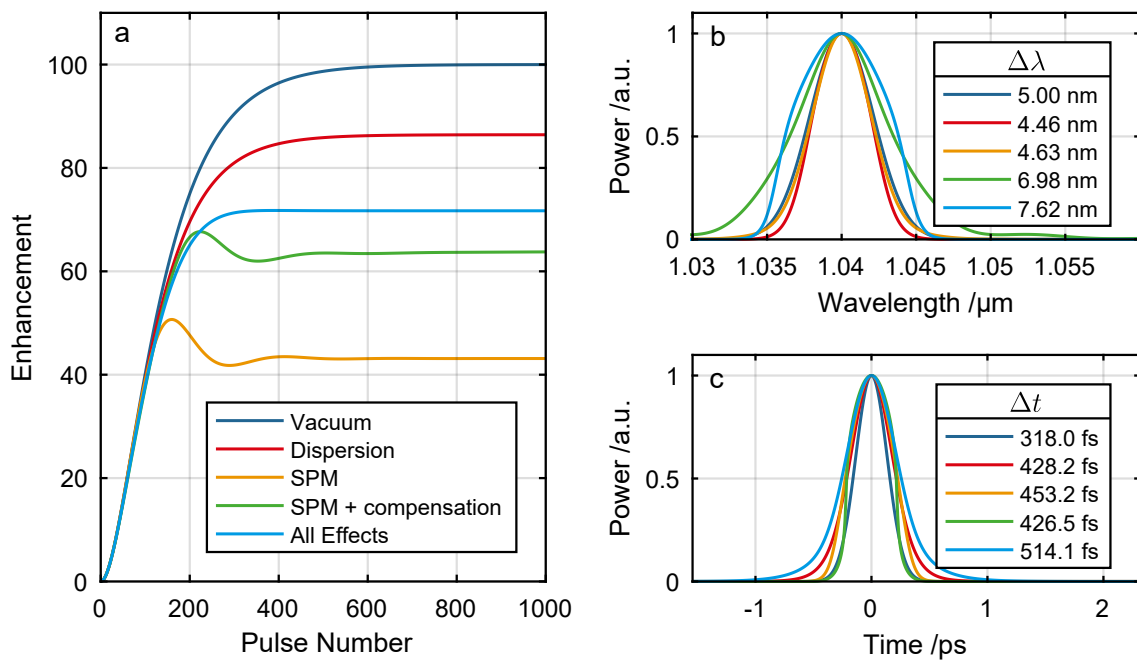
Figure 3.3.: a) Exemplary plot for the build-up signal of 1000 pulses in a 10-MHz enhancement cavity. The Fourier-limited, Gaussian shaped input pulses have spectral bandwidth of $5\,\mathrm{nm}$ and a duration of $318\,\mathrm{fs}$, respectively. They contain an energy of $E_{\mathrm{in}} = 5\,\mathrm{nJ}$, the cavity round-trip losses are $L = 1\,\%$ and the input-coupler reflectivity is $R = 99\,\%$. The unstretched pulses are seeded into the cavity. Different cases are depicted: without any dispersion or SPM (dark blue), under consideration of the dispersion (β_2- and β_3-effects) due to $23.5\,\mathrm{mm}$ of fused silica (typical length of an acousto-optical modulator) in the cavity (red), considering the SPM caused by the AOM in the cavity when the beam is focused to $0.4\,\mathrm{mm}$ in the AOM, not compensated (yellow) or compensated (green), and all of these effects combined (light blue). b) shows the corresponding enhanced spectra and their FWHM bandwidth and c) depicts the temporal pulse-shapes and their FWHM duration, each after 1000 stacked pulses.

Contrary to phase perturbations, a pulse acquires prior entering the cavity [49], every perturbation that is added to the pulse within the cavity has a negative impact on the achievable

enhancement and the stacking efficiency. This is intuitive since the pulse inside the cavity needs to be identical to the incoming pulse, in terms of spectral and temporal phases, to overlap perfectly. If the pulse in the cavity acquires an additional phase perturbation during every round-trip, its shape will increasingly deviate from the shape of the input pulse, thus limiting the enhancement. Figure 3.3 shows the development of the enhancement during the build-up process. The simulation parameters are chosen to depict common scenarios. The two major effects that lead to the mentioned phase perturbations are dispersion and self-phase modulation. Both are often introduced by a transmissive element, such as an acousto-optic modulator or a Pockels-cell inside the cavity. Furthermore, the HR-coatings of the cavity mirrors can be accountable for a considerable amount of dispersion. Theoretically, such dispersive effects can be completely compensated for by adequate mirrors [80]. However, due to manufacturing uncertainties, it is unlikely to achieve this in the experiment and therefore the influence of the residual dispersion needs to be considered. The SPM related phase perturbations, however, are partially automatically compensated for by a constant phase, which is added by the stabilization when optimizing the overlap. This is taken into account for the 'SPM compensated' and 'All Effects' plot in Fig. 3.3a, where an optimization was carried out to find the best phase offset between the incoming pulse and the intracavity pulse, to partially compensate the SPM and achieve the highest possible enhancement. The simulations show that a certain amount of dispersion leads to a slower build-up and a reduction of the enhancement in steady-state operation. The effects of SPM on the build-up and saturation behaviour are more complex. Even when compensated, the spectral and temporal shape of the enhanced pulse may be drastically changed, as visible in the plots. The periodical nature of the phase distortion is also visible in the build-up curve, which, contrary to the normal build-up, does not converge to a maximum with increased pulse number, but has a distinct maximum after a certain number of stacked pulses. Both, dispersion and SPM, narrow the spectral bandwidth and broaden the temporal shape of the pulse. This acts as a strong motivation to minimize both effects.

3.2.3. Impedance Matching

Impedance matching in general aims to minimize reflections of a source signal at a load. This leads to an optimal power transfer from the source to the load. In this case, the seeding field is the source and the field within the enhancement cavity is the load. With the round-trip attenuation A of the cavity being defined as $A = 1 - L$, the iImpedance-matching condition is given as [76]:

$$R = A = 1 - L \, . \tag{3.13}$$

If this condition applies, the theoretically possible power enhancement from Eq. 3.9 can be simplified to

$$V = \frac{1}{1 - R} = \frac{\mathcal{F}}{\pi} \, . \tag{3.14}$$

Fig. 3.4 depicts the impedance-matching condition visually. The highest enhancement is always achieved when Eq. 3.13 is fulfilled.
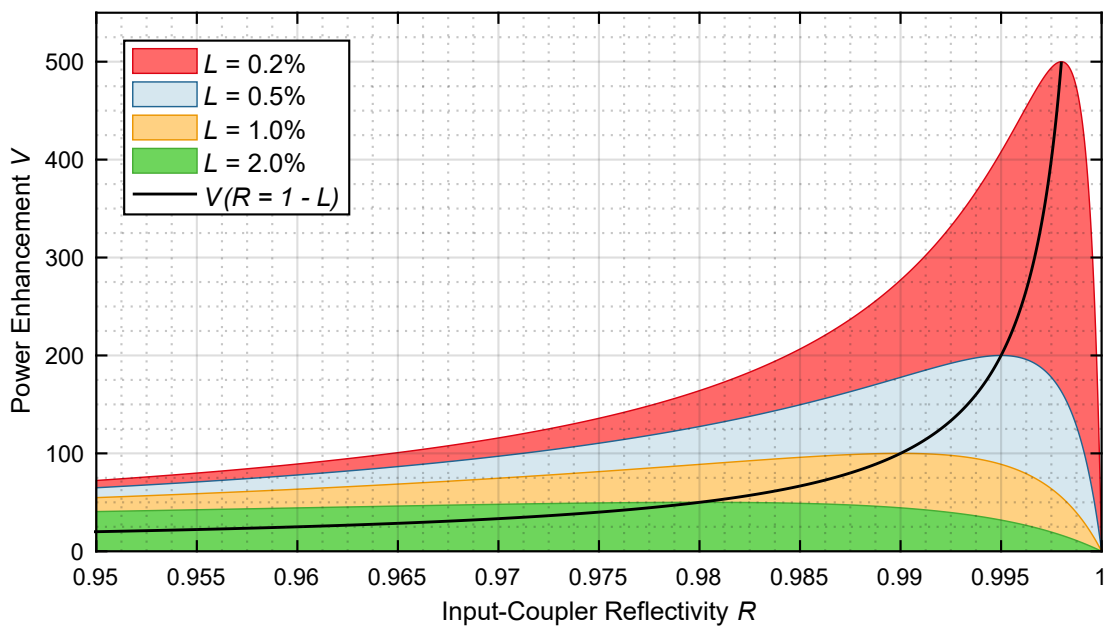
Figure 3.4.: Power enhancement for different intracavity losses and the impedance matched input-coupling mirror, respectively. A cavity in vacuum without any dispersion or nonlinear effects was assumed.

3.2.4. Matching of the Transversal Mode Profile

Matching the spatial profile of the incoming beam to the cavity mode at the input-coupler is crucial, when a beam is to be enhanced in a resonator. Generally, the overlap of the input beam profile with the intracavity mode is not perfect and, therefore, the amount of in-coupled power is not equal to the overall input power. The spatial distribution of the incident field $T_{\text{in}}(x, y)$ can be treated as a superposition of the orthogonal cavity Eigenmodes at the

input-coupling mirror (IC). This sum can be separated in two summands, the fundamental mode $T_{00}(x, y)$ and higher order modes $T_{\mathsf{HOM}}(x, y)$ as follows:

$$T_{\mathsf{in}}(x, y) = \sum_{mn} \alpha_{mn} T_{mn}(x, y) = \alpha_{00} T_{00}(x, y) + T_{\mathsf{HOM}}(x, y) \ . \tag{3.15}$$

Using the dielectric constant ϵ_0, the incident power can hence be described as

$$P_{\mathsf{in}} = \frac{c\epsilon_0}{2} \int \int |T_{\mathsf{in}}(x, y)|^2 \, \mathsf{d}x \mathsf{d}y = \frac{c\epsilon_0}{2} |\alpha_{00}|^2 |T_{00}(x, y)|^2 + P_{\mathsf{HOM}} = P_{00} + P_{\mathsf{HOM}} \ . \tag{3.16}$$

All the mixed terms disappear since the Eigenmodes are orthogonal. The input power P_{in} is therefore the sum of the power in the fundamental mode P_{00} and all the power in the higher-order-modes P_{HOM}. Since most applications, and stack-and-dump in particular, are interested in the enhancement of the fundamental mode, it is now convenient to define the spatial overlap U_{s} of the input beam with the fundamental cavity mode, in order to evaluate the mode-matching

$$U_{\mathsf{s}} = \frac{\left| \int \int T_{\mathsf{in}}(x, y) \alpha_{00}^* T_{00}^*(x, y) \mathsf{d}x \mathsf{d}y \right|^2}{\int \int |T_{\mathsf{in}}(x, y)|^2 \, \mathsf{d}x \mathsf{d}y \cdot \int \int |\alpha_{00} T_{00}(x, y)|^2 \, \mathsf{d}x \mathsf{d}y} = \frac{P_{00}}{P_{\mathsf{in}}} \ . \tag{3.17}$$

The essence of this section can be summarized as follows: the size and curvature of the input beam have to be matched to the intracavity mode at the input-coupling mirror. While theoretically a spatial overlap of $100\,\%$ is possible, experimentally achieved values commonly vary between 75 and $95\,\%$.

3.2.5. Characterization

Apart from the beforehand mentioned spatial overlap U_{s}, the non-perfect temporal overlap U_{t} limits the achievable power enhancement factor, the 'effective enhancement' V_{eff}. This typically occurs due to insufficient phase matching, as well as dispersive or nonlinear effects inside the cavity, as discussed in Sec. 3.2.2. Hence, the effective enhancement V_{eff} will always be below the theoretically possible enhancement of a given combination of round-trip losses L and reflectivity of the IC R. It can be easily calculated as

$$V_{\mathsf{eff}} = U_{\mathsf{s}} U_{\mathsf{t}} V = U V \ , \tag{3.18}$$

with U representing the overall overlap, temporally and spatially, and hence expressing the deviation of the effective enhancement from the theoretically possible enhancement with the employed set of cavity mirrors and intracavity elements. Experimentally, V_{eff} can be readily derived from the circulating average power inside the cavity P_{IC} and the average power of the input beam P_{in} as follows

$$V_{eff} = \frac{P_{IC}}{P_{in}} \ . \tag{3.19}$$

While P_{in} can be measured directly in front of the IC, P_{IC} has to be calculated from the leaking power P_{leak} behind one of the cavity mirrors with known transmittance T_{leak}. It can be expressed as

$$P_{IC} = \frac{P_{leak}}{T_{leak}} \ . \tag{3.20}$$

Equation 3.19 can now be written as

$$V_{eff} = \frac{P_{leak}}{P_{in} \cdot T_{leak}} \ . \tag{3.21}$$

Additionally, if the losses do not fulfill the criteria for impedance matching as explained in Eq. 3.13, an additional deviation factor U_i has to be introduced. Consequently, due to the mentioned spatial U_s, temporal U_t or impedance U_i mismatch, not the entire input power can be coupled into the cavity and a certain amount gets reflected at the IC and can be measured as P_{refl}. When the cavity round-trip is blocked, the entire input power is reflected and P_{refl} will reach a maximum which is defined as P_{refl}^{max}. Otherwise, when the cavity length matches the pulse repetition time, P_{refl} drops, as a certain fraction of the incoming field can now constructively interfere with the field inside of the cavity. In the ideal case of a perfectly stabilized, impedance and mode matched and dispersion free cavity, no power will be reflected, and therefore P_{refl} equals zero. Since this is usually not the case in an experiment, a power level $P_{refl} > 0$ remains. This is defined as the minimum level of reflected power P_{refl}^{min}. The so-called coupling-parameter K characterizes how well the input-power is coupled into the cavity and is given as

$$K = U_s U_t U_i = 1 - \frac{P_{refl}^{min}}{P_{refl}^{max}} = 1 - \left(\frac{\sqrt{R} - \sqrt{A}}{1 - \sqrt{RA}} \right)^2 \ . \tag{3.22}$$

K is the fraction of enhancement that has been achieved, compared to the enhancement that would have been possible with the given losses L of the cavity, when using the impedance

matched IC ($R = 1 - L \Rightarrow U_\mathrm{i} = 1$) and achieving perfect temporal and spatial overlap of the incoming field with the cavity field $U_\mathrm{s} = U_\mathrm{t} = 1$. It is noteworthy that perfect impedance matching is rarely achieved in an experiment and is for non-steady-state cavities not even desired (more on that in Sec. 3.3.2). The levels $P_\mathrm{refl}^\mathrm{max}$ and $P_\mathrm{refl}^\mathrm{min}$ can easily be measured by a photo-diode, monitoring the reflected signal. Since only the ratio is important, no absolute power measurement is necessary. The round-trip attenuation is connected to K and V_eff by

$$A = 1 - \frac{K}{V_\mathrm{eff}} \,. \tag{3.23}$$

This allows for a straightforward calculation of A, and hence, an indirect measurement of the cavity losses L with measured values $P_\mathrm{refl}^\mathrm{max}$, $P_\mathrm{refl}^\mathrm{min}$ and V_eff. A complete derivation of Eq. 3.23 can be found in Sec. A.3.

3.3. Fundamentals of Non-Steady-State Enhancement

Different design approaches have to be considered when an enhancement cavity is to be operated in a non-steady-state setup. Non-steady-state means, that the energy in the cavity fluctuates considerably over time, particularly due to the extraction of enhanced pulses.

3.3.1. Cavity Efficiency and Output Quantities

The stacking efficiency of a non-steady state enhancement cavity can be calculated as the ratio of intracavity energy E_IC to the summarized energy of all N input pulses with the energy E_in:

$$\eta_\mathrm{stack} = \frac{E_\mathrm{IC}}{N E_\mathrm{in}} \,. \tag{3.24}$$

Extracting the intracavity energy via a switch is usually also limited by the extraction efficiency η_ext. Hence, the overall cavity efficiency is further reduced to

$$\eta = \eta_\mathrm{stack} \eta_\mathrm{ext} \,. \tag{3.25}$$

For example, if an AOM is employed, η_ext would be the diffraction efficiency of the AOM. This allows to define the output power and energy of the cavity as

$$P_\mathrm{out} = \eta P_\mathrm{in} \quad \text{and} \quad E_\mathrm{out} = \eta N E_\mathrm{in} = \frac{P_\mathrm{out}}{f_\mathrm{switch}} \,, \tag{3.26}$$

with f_{switch} being the switching-rate of the switch. η_{stack} strongly depends on the losses L and R, since it determines the amount of in-coupled energy per pulse during the build-up. Optimizing the input-coupler reflectivity R for specific losses L, a certain number of stacked pulses N and extraction efficiency η_{extr} for one cycle is a rather easy task. But as soon as a fraction of the field remains in the cavity after the switching process (e.g. 0th order of AOM), the build-up dynamics change drastically. And since in reality a vast number of stacking cycles occur subsequently, the task of optimizing R becomes increasingly difficult and can indeed only be addressed numerically.

3.3.2. Intracavity Pulse Build-up and Extraction
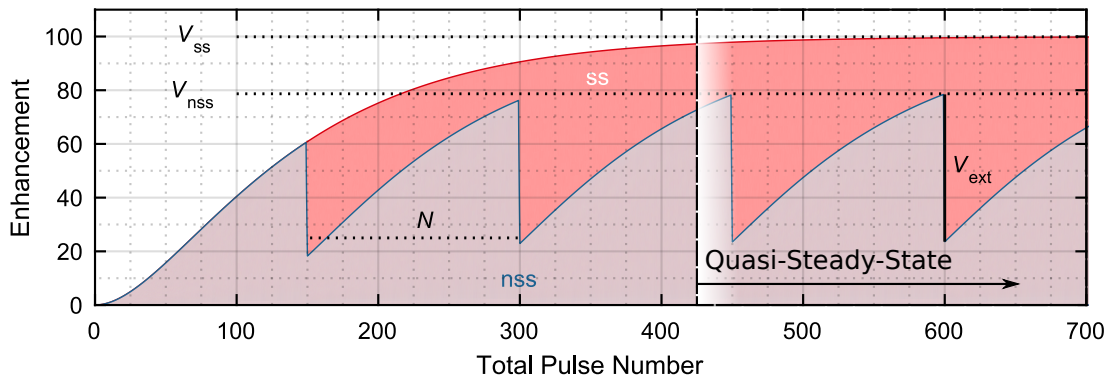
Figure 3.5.: Build-up of the intracavity enhancement is depicted for the steady-state scenario (ss) and for the non-steady state scenario (nss). Each scenario has a maximum enhancement V_{ss} and V_{nss}. Both simulations were carried out for $L = 1\,\%$, $R = 99\,\%$ and $\eta_{ext} = 70\,\%$. For the nss-case $N = 150$ pulses were stacked per build-up cycle.

If not the entire pulse energy is extracted after one build-up phase, there will be a remaining field E_R in the cavity. This naturally changes the subsequent build-up and so forth. After a few build-up cycles a 'quasi-steady-state' sets in (see Fig. 3.5). During the work for this thesis an equation for the extracted enhancement V_{ext} in this 'quasi-steady-state' scenario was derived as [39]:

$$V_{ext} = \eta_{ext} V_{eff} = \eta_{ext} \cdot \frac{(1 - R)\left[\left(\sqrt{AR}\right)^N - 1\right]^2}{\left(\sqrt{AR} - 1\right)^2 \left[1 - \left(\sqrt{AR}\right)^N \sqrt{1 - \eta_{ext}}\right]^2} \, . \tag{3.27}$$

This formula allows to calculate the extracted enhancement that can be expected from a stack-and-dump cavity with a given set of round-trip losses L, input-coupler reflectivity R, number of stacked pulses per cycle N and extraction efficiency η_{ext}. The appendix shows a more detailed derivation (Sec. A.1), similar to the derivation of Eq. 3.9 [76]. The experimentally achieved extracted enhancement can be easily calculated via

$$V_{\text{ext}} = \frac{E_{\text{out}}}{E_{\text{in}}} \ . \tag{3.28}$$

The overall efficiency of a stack-and-dump cavity η can be directly calculated from the easily measurable values of the extracted power P_{ext} and the input power P_{in}, or via the relation between extracted enhancement and number of pulses per build-up cycle

$$\eta = \frac{P_{\text{ext}}}{P_{\text{in}}} = \frac{V_{\text{ext}}}{N} \ . \tag{3.29}$$

It is noteworthy, that the efficiency can be further influenced and potentially be improved by using either a burst input [81], or by shaping the amplitude of the input pulses [28], as further discussed in Sec. 3.3.3. The repetition rate of the extracted signal equals the switching rate and can easily be calculated using the original repetition rate f_{rep} and the number of stacked pulses N via

$$f_{\text{switch}} = \frac{f_{\text{rep}}}{N} \ . \tag{3.30}$$

While for steady state enhancement cavities the optimum reflectivity of the input-coupling mirror R is determined by the impedance matching condition (see Eq. 3.13), the operation of a non-steady state cavity has different requirements on an optimum R. It is usually optimized to achieve the most efficient pulse-build up for a given number of pulses N. Such an optimization is shown in Fig. 3.6 for different pulse numbers. The reflectivity, losses and extraction efficiency were chosen to suit the experiments that will be presented in Sec. 4.3 of this thesis.
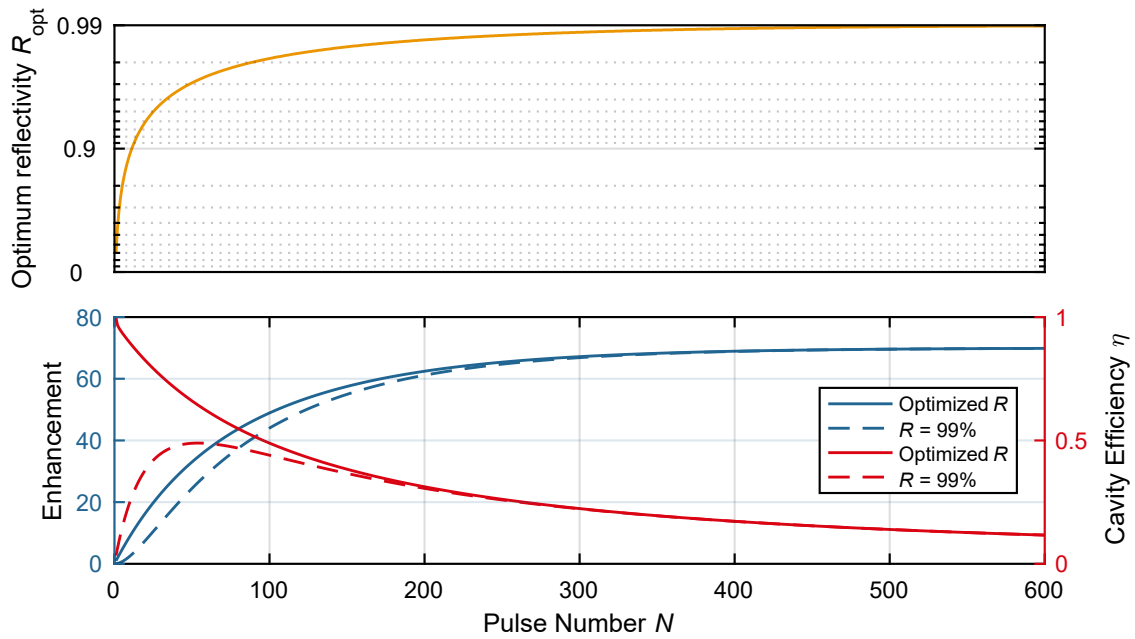
Figure 3.6.: Depicted is the optimum reflectivity R (logarithmic), the enhancement and the efficiency η (linear) over the number of stacked pulses N. Simulation parameters were: $L = 1\%$ and $\eta_{\text{ext}} = 70\%$, neglecting any phase terms due intracavity dispersion or SPM.

It is observable that optimizing the input-coupler to the number of stacked pulses is especially important for a small number of stacked pulses, or in other words, when the energy in the cavity is extracted long before the steady-state is reached. R converges to A when N increases, since this equals the steady-state case. Another interesting effect is visible for very low pulse numbers, due to the remaining field in the cavity ($1 - \eta_{\text{ext}} = 30\%$ of the energy remain after every build-up cycle). The cavity is very efficient for extremely low pulse numbers, since the part of the incoming field that constructively interferes on the inside of the input-coupler is much bigger than for an empty cavity and the impact of the losses is negligible.

3.3.3. Shaped Input Pulse Train
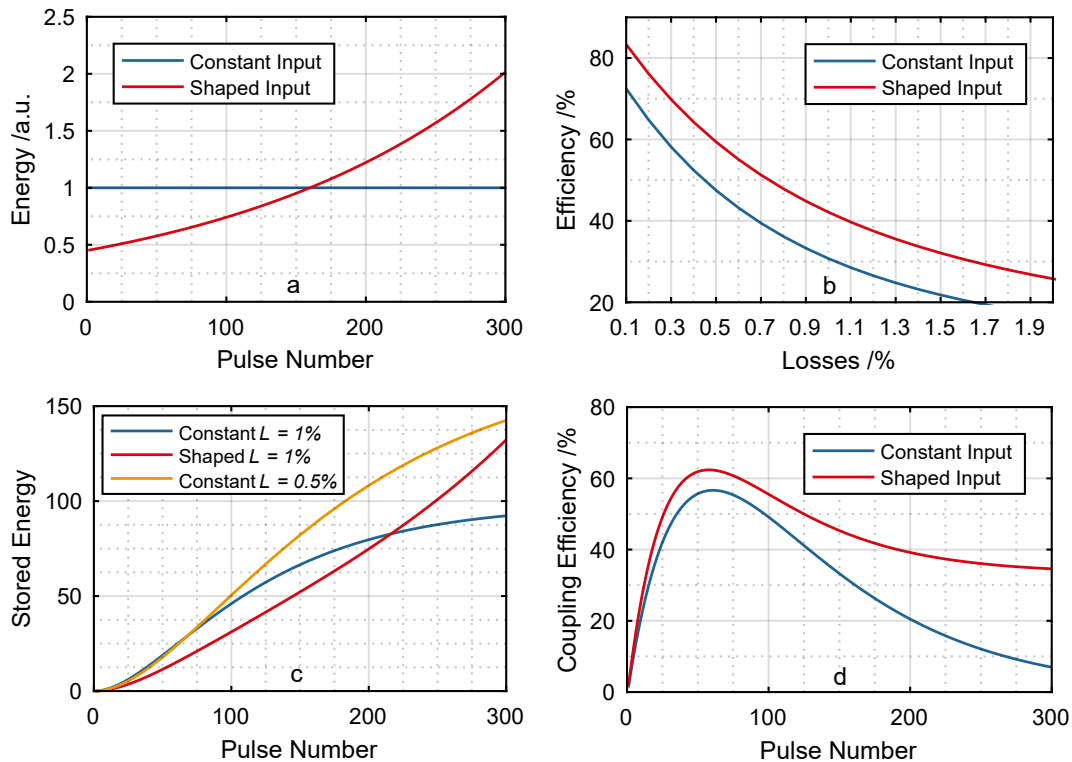
Figure 3.7.: a) Two different shapes of an incident pulse train consisting of 300 pulses. b) Maximum stacking efficiency of the cavity for varying losses assuming an optimum transmittance of the input coupling mirror when seeded with 300 pulses using the input pulse trains of a). c) Enhancement during the build-up and d) development of the coupling efficiency as a function of the pulse number in the input pulse train assuming losses of 1% and an optimized reflectivity [28].

If the efficiency of the stacking process is paramount, it can be beneficial to shape the amplitude of the input pulse train. This allows to reduce the amount of reflected energy in the early phase of the build-up. Fig. 3.7 compares two different scenarios, namely using input pulses with a constant energy or an input with an exponentially shaped amplitude (see Fig. 3.7a). This is merely an example and further optimization of the shape might be possible. Part b) shows, that for each loss value the efficiency can be improved using the amplitude shape as shown in a). This is depicted in c) and d) in greater detail for the example of 300 pulses stacked a cavity with a round-trip loss value of 1%. It can be seen, that while the constant input pulse train fails to couple energy into the cavity efficiently, the shaped input achieves a highly improved energy transfer, ultimately also leading to a higher overall stacking efficiency. This is simply due to the fact, that the deviation between the amplitude of the

field inside the cavity and the amplitude of the incoming field acts as a crucial limitation on the efficiency of this energy-transfer. When a shaped input is used, this difference is much smaller and, thus, a better transfer is achieved. Subplot c) also depicts the Enhancement during the build-up for lower losses of $0.5\,\%$. Compared to the shaped input pulse train, this leads to similar enhancement values, which underlines the benefit of a shaped input.

However, when generating an incoming pulse train with a shaped amplitude, matching the nonlinear phases of the individual pulses is crucial. This introduces additional demands on the amplifier, leading to some of the downsides of DPA and GTI, which were originally aimed to avoid using SnD. Furthermore, if the amplifier can handle the last pulse of the shaped incoming pulse train, it would also be possible to generate a train of pulses, in which every pulse contains that amount of energy, thus, leading to a higher enhanced energy. Shaping the input pulse train is therefore only interesting, if achieving the highest wall-plug efficiency is the primary design requirement. Hence, this approach was not investigated any further.

3.3.4. Limitations due to Nonlinear Effects

The SPM-effects discussed in Sec. 3.2.2 can have significant influence on the energy build-up inside the cavity from early on. If, for example, an AOM is used to extract the pulses, a small beam size is needed in the AOM to allow for sufficiently fast switching (see Sec. 3.6 for further details). This results in relatively high intensities, even for stretched pulses. The acquired nonlinear phase leads to a phase-mismatch between the intracavity-pulse and the incoming pulse. Furthermore, the phase of the intracavity-pulse changes every round-trip. Hence, for a larger number of pulses the phase-matching worsens. This behaviour is hard to simulate, as in reality, the stabilization algorithm of the cavity makes up for the average phase mismatch between them, in order to optimize for the highest IC-field. This offset phase added from the stabilization was neglected for these simulations. To justify this approximation, simulations including this effect were carried out for some carefully chosen parameters (one example is shown in Fig. 3.3). The results allowed to estimate, that the difference is only up to a factor of ~ 2 and therefore does not lead to significant better scalability.
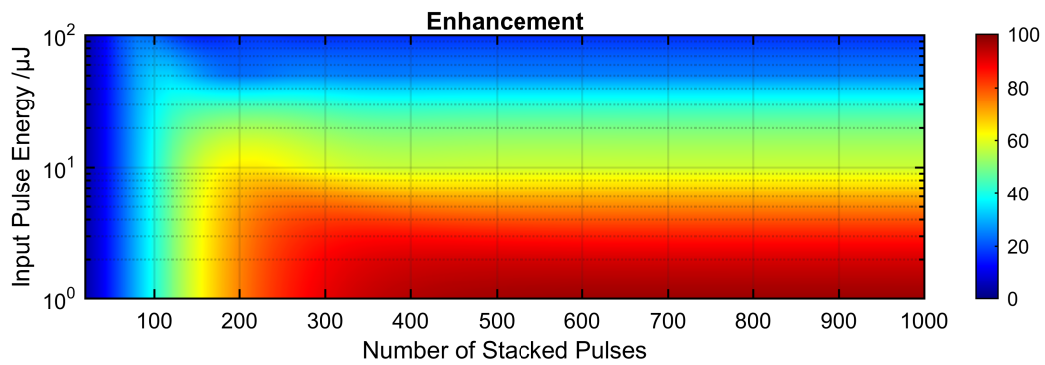
Figure 3.8.: Enhancement factor depending on input pulse energy and number of stacked pulses in the presence of SPM.

For the simulation shown in Fig. 3.8, Gaussian-shaped seeding pulses with a bandwidth of $5\,\text{nm}$ centered around $1040\,\text{nm}$ and stretched to $1.5\,\text{ns}$ pulse duration were assumed. The cavity round-trip losses were set to $1\,\%$ and the input-coupler reflectivity to $99\,\%$. The AOM in the cavity is $2.35\,\text{cm}$ long and the diameter of the transmitting beam is $0.4\,\text{mm}$. To simplify the simulations, a diffraction efficiency of 1 was assumed for the AOM. For an extraction efficiency below $100\,\%$, the effects gain significance, due to the higher number of interacting pulses. Dispersion in the cavity was neglected. The energy of the input pulses was varied between $1\,\upmu\text{J}$ and $100\,\upmu\text{J}$, while the pulse number varies between 50 and 1000. The plot in Fig. 3.8 shows the onset of SPM as a limiting mechanism depending on pulse energy and number of stacked pulses. For input pulse energies above $\sim 2\,\upmu\text{J}$, SPM effects in the AOM start having an impact on the enhancement. Naturally, for lower numbers of stacked pulses, the effect is less influential, which is visible in Fig. 3.9. It shows the reduction factor of the enhancement compared to the SPM-free case.
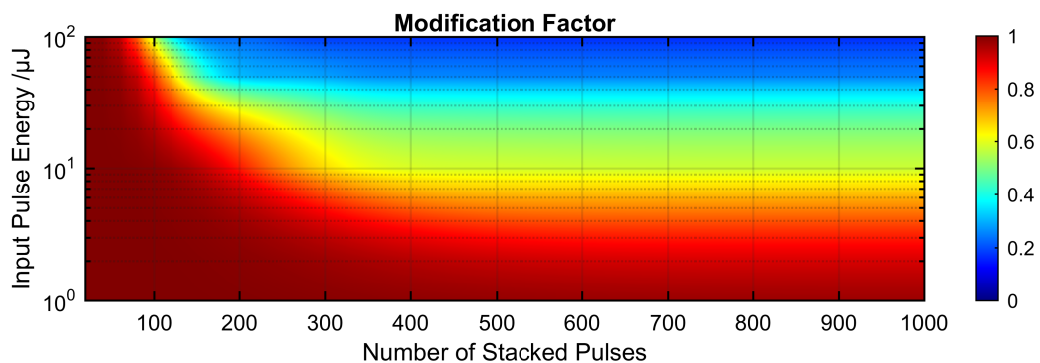

Figure 3.9.: Enhancement modification factor depending on input pulse energy and number of stacked pulses in the presence of SPM.

Stacking of 100 pulses with $20\,\mu\text{J}$ energy can be done without trade-offs, while the stacking of 300 pulses with the same energy results in a reduction of the enhancement, compared to the low-energy by $\sim 40\,\%$. This has the effect, that in presence of SPM, the typical saturation behaviour of the pulse build-up is altered in a way that fewer pulses eventually lead to higher enhancement factors. While at first counterintuitive, it becomes understandable, due to the higher number of interacting pulses, leading to a worse phase-matching between them. Altogether it can be stated, that the limitation due to the usage of AOMs is not damage-related but occurs much earlier due to the acquired nonlinear phases.

3.4. Oscillator and Cavity

3.4.1. Optical Path Length Matching

As explained in Sec. 2.2, in order to constructively interfere, the temporal and spectral phase of two pulses need to be matched. That is why, matching the temporal offset between the pulses is a necessity. Therefore, firstly the cavity has to be designed in a way that the optical path length of the cavity $n_\text{c}s_\text{c}$ matches an integer multiple k of the optical path length of the oscillator $s_\text{o}n_\text{o}$

$$n_\text{c}s_\text{c} = ks_\text{o}n_\text{o} \,, \tag{3.31}$$

with s_o and s_c being the physical length of the oscillator and cavity, respectively. If no pulse-picking is carried out in the laser system prior the cavity, k would be unity, otherwise k equals the picking factor. If, for example, the oscillator is operated at $80\,\text{MHz}$ and the cavity at $10\,\text{MHz}$, the pulse picker selects every 8th pulse resulting in $k = 8$. Since enhancement cavities are often embedded in vacuum chambers, the refractive index in the oscillator n_o and in the cavity n_c might be different and have to be considered. Even such small deviations, as the change between air and vacuum, are of paramount importance during the design as easily seen in this short example for a $10\,\text{MHz}$-cavity

$$\Delta s = \frac{c}{n_\text{vac}f_\text{rep}} - \frac{c}{n_\text{air}f_\text{rep}} = \frac{c(n_\text{vac} - n_\text{air})}{n_\text{air}n_\text{vac}f_\text{rep}} \approx 0.9\,\text{cm} \,. \tag{3.32}$$

This is the length change that needs to be compensated for in a formerly a matched cavity after the transition to vacuum. Due to thermal drifts and vibrations, fluctuations of the

optical-path length in oscillator and cavity occur permanently. An active stabilization of the length of either one of them to the other is therefore crucial. The thereby required error signal can be generated by numerous different methods (e.g. Hänsch-Couillaud [82] or Tilt-Locking [83]). However, Pound-Drever-Hall [84] was identified to deliver the most reliable stabilization in earlier publications [46] and was therefore implemented in all cavities presented in this thesis. The error signal needs to be asymmetrical, in order to be able to conclude the correct direction for the compensating element in the optical setup. It can be calculated, as depicted in Sec. A.4, which leads to error signals as shown in Figure 3.10. Therein, it becomes obvious, that for higher finesse cavities the prominence of the error signal decreases. This is important since in reality the signal shows some noise as well, making distinguishing the signal from the noise increasingly difficult at a high finesse. The relevant section for the loop controller is the small frequency range around the resonance, which is, for small deviations, linear to the length change [85]. Typically, a conventional PID- or PI^{2}D-scheme is employed as a controller. The path length matching is often carried out in two control loops. One loop with a small motion range makes up for fast fluctuations by changing the oscillator length accordingly. These are mostly caused by mechanical vibrations. A second, slower loop, compensates slow thermal or air-related drifts with a longer motion range inside of the cavity.
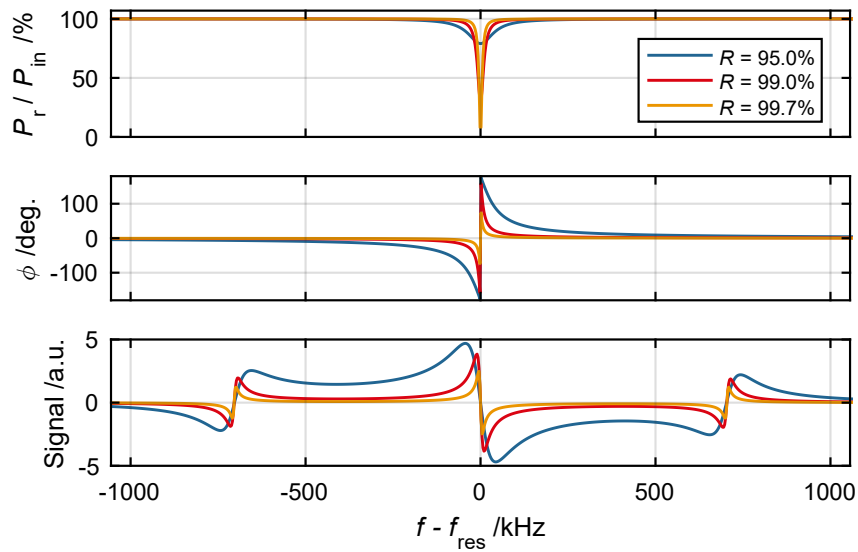
Figure 3.10.: (a) Reflected Power at the input coupling mirror of the cavity. (b) Phase of the reflected signal. (c) Pound-Drever-Hall error signal for a varying reflectivity R of the input-coupling mirror. All simulations where carried out for $P_{\text{in}} = 10\,\text{W}$, $L = 0.3\,\%$, and a central-wavelength of $1040\,\text{nm}$, as well as a cavity-length of $30\,\text{m}$ and a modulation-amplitude of $500\,\text{mV}$ at a frequency of $704\,\text{kHz}$. The imperfect impedance matching becomes apparent in a non-zero reflected field at the resonance frequency.

3.4.2. Impact of the Cavity Length

The oscillator stability and therefore the width of the comb-lines, limits the possible enhancement in any cavity [46]. The possible enhancement scales proportional to the finesse. The finesse, however, depends on the width of the comb-lines f_{FWHM}, given by the input signal that is to be enhanced, and the free-spectral-range f_{FSR} of the cavity. As the free-spectral-range shrinks for a longer cavity, it can be deduced, using Eq. 3.10, that for the possible enhancement, the following relation is valid:

$$V(s) \sim \mathcal{F}(s) = \frac{f_{\text{FSR}}(s)}{f_{\text{FWHM}}} = \frac{c}{s \cdot f_{\text{FWHM}}} \sim \frac{1}{s}. \tag{3.33}$$
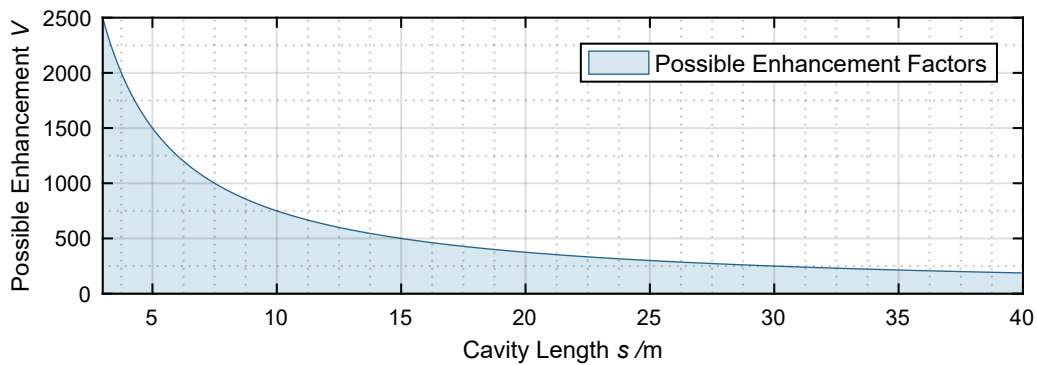
Figure 3.11.: Possible enhancement with the same oscillator for different cavity length.

Therefore, an oscillator that allowed for an enhancement of up to 1500 in a 5-m long cavity only allows for an enhancement of 250 in a 30-m long cavity. However, at the same time the required stabilization and adjustment accuracy scales also with the length of the resonator and the enhancement. In other words, stabilizing a 30-m long cavity at an enhancement-level of 250 is equally challenging, as stabilizing a 5-m long cavity at an enhancement level of 1500. An additional difference, however is, that thermal drifts of the cavity length have more impact in a longer cavity, increasing the difficulty to adjust a free-running long cavity to the desired resonance before the lock can be initiated and increases the requirements on the stabilization scheme. Furthermore, when the cavity is evacuated, a larger change of the optical-path-length needs to be compensated by a remotely controlled stage (see Eq. 3.32), which also leads to a misalignment of the reflection angles in the cavity relative to the original adjustment in air. This can only be partially compensated for, unless all cavity mirrors are motorized, which is for practical reasons only possible in cavities with a low number of mirrors. However, in order to still be able to extract pulses between subsequent round-trips as described in Sec. 3.6, it is necessary to find a good compromise in terms of cavity length.

3.5. Requirements on Cavity Dumpers
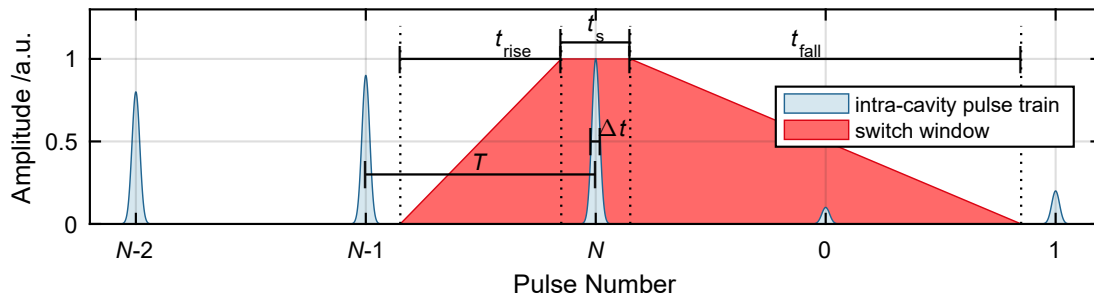
Figure 3.12.: A section of an intracavity pulse train is shown. The N-th pulse is the one to be extracted. Plotted are: the switching window t_s, the pulse-duration Δt, the rise-time of the switch t_rise, the distance between two successive pulses T, the fall-time t_fall and duration of the switch-window Δt_s.

Arguably the most critical part of the entire SnD cavity is the switch. It needs to suffice a multitude of requirements. The most important demands on an ideal switch can be summarized as:

- **High velocity** It needs to be fast enough to switch as shown in Fig. 3.12. While the rising slope of the switch is limited in duration by the distance between two successive pulses as

$$t_\mathsf{rise} \leq T - 2\Delta t \tag{3.34}$$

the requirements on the falling slope are more relaxed. A small number of blocked pulses in the beginning of the build-up reduce the cavity efficiency only slightly and are hence acceptable. The duration the switch needs to stay in the 'out-coupling position' is given by the pulse duration itself as

$$t_\mathsf{s} \geq 2\Delta t \ . \tag{3.35}$$

- **Purely reflective** Transmissive elements introduce significant losses, dispersion and nonlinear effects. Due to the Fresnel-reflex on the surface, an anti-reflex-coating is usually unavoidable. However, even the best available AR-coatings introduce residual losses of around $0.25\,\%$ per surface (for $\lambda \approx 1\,\mu\mathrm{m}$) [86], limiting the cavity finesse and hence, the possible enhancement. Furthermore, absorption in the material itself and in the coatings occurs, which will, at high powers, eventually lead to heating, beam distortions and ultimately to the destruction of the switch.

- **Large aperture** Even if the light is only reflected, a distribution of the beam over a large area is desirable, in order to reduce thermal effects in the coating. This is, however, a minor issue if the coatings are sophisticated enough to withstand the power-densities.

The next section will explain a variety of switching techniques and briefly compare their up- and downsides.

3.6. Switching Techniques

Some devices, such as AOMs and Pockels-Cells are commonly used in switching applications, while others are less typical. In this section, the working principle of possible switching devices and their advantages and disadvantages will briefly be discussed.

3.6.1. Pockels-Cell

Pockels-cells (PCs) [87] operate by rotating the polarization of the beam to allow for the separation via a polarization dependent component. For cavity switching applications, especially in regenerative amplifiers, they are the most common choice. This is primarily since they offer an extremely fast switching process at a relatively flexible aperture size. However, they also introduce critical limitations, since the electro-optical materials used for Pockels-cells, typically Beta barium borate (BBO) or Potassium titanyl phosphate (KTP), obtain a low tolerance for peak power related and thermal effects. This can be partly compensated for, by increasing the free aperture of the PC. However, this also increases complexity and cost of the system, since the driver needs to supply higher voltages. The largest PCs have a clear aperture of up to $10 \cdot 10 \, \text{mm}^2$ and need to be switched with a voltage of $\sim 13.5 \, \text{kV}$ to distinguish pulses in pulse trains with a temporal separation of $\sim 35 \, \text{ns}$ [54]. Furthermore, a polarization dependent optical component, such as a thin-film polarizer (TFP), is necessary, in order to finally extract the pulse. This combination of Pockels-cell and TFP typically introduces round-trip-losses of around $1 \, \%$ and thereby limits the possible enhancement and the efficiency.

3.6.2. Acousto-Optic Modulator

Acousto-Optic-Modulators (AOMs) [88] separate beams using an acoustically induced grating to diffract a certain temporal fraction of a beam away from its original path, as shown in Fig. 3.13. AOMs have many applications reaching from the loss-modulation in Q-switch resonators to the reduction of the pulse-repetition rate in most state-of-the-art ultrafast laser systems. They can have rise-times in the ns-range and are easily implemented. Their rise-time scales with the beam diameter d_x in x-direction and the sound velocity v_{us} as:

$$t_{rise} \approx 0.65 d_x / v_{us} \, . \tag{3.36}$$

Hence, to achieve rise-times below $100\,\text{ns}$, e.g. in fused silica with $v_{us} = 5960\,\text{m/s}$, the beam-diameter needs to be below $1\,\text{mm}$. This increases the intensity in the AOM and reduces the pulse-peak power such devices can handle, leading to similar limiting effects in terms of thermal and nonlinear effects, as described for the PC. This impact is described in greater detail in Sec. 3.3.4.
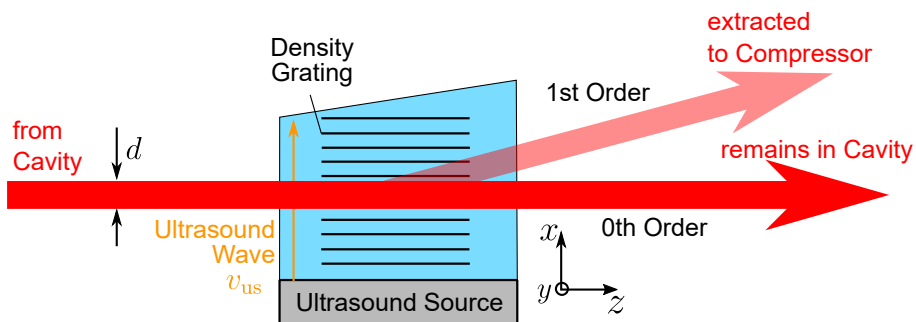
Figure 3.13.: Working principle of an acousto-optical-modulator as an optical switch in a cavity.

3.6.3. Electro-Optical Deflector

Similar to a Pockels-cell, in an electro-optical deflector (EOD) [89], the refraction index is changed by applying a voltage. This leads to a change of the refraction angle, as depicted in the setup in Fig. 3.14. Such a device is potentially interesting for SnD, due to the short distance the beam is propagating in the material, and the therefore small amount of nonlinear and thermal effects. Furthermore, EODs can achieve fast switching times and offer large apertures [90]. However, they also only introduce small separation angles, and the material

needs to have a high non-linearity. The separation angle can be calculated via:

$$
\begin{aligned}
\Delta\epsilon &= \epsilon_2 - \epsilon_1 \\
&= \arcsin\left\{(n_2 + \Delta n)\sin\left[2\alpha + \arcsin\left(\frac{\sin\beta}{(n_2 + \Delta n)}\right)\right]\right\} \\
&\quad -\arcsin\left\{n_2\sin\left[2\alpha + \arcsin\left(\frac{\sin\beta}{n_2}\right)\right]\right\}
\end{aligned}
$$

In a typical example, using BBO with $n_2 = 1.655$ (for $\lambda = 1\,\mu m$ [91]) as wedge material, choosing $\alpha = 5°$ and $\beta = 47°$ and assuming a typical refractive index change [89] of $\Delta n = 1\cdot10^{-4}$, the resulting separation angle is only about $0.1\,mrad$. This equals a spatial separation between the beam paths of around $1\,mm$ after $10\,m$. Due to the Gaussian propagation behaviour, such a small separation is not sufficient to isolate the enhanced pulse. It is noteworthy, that, while the separation angle does not depend on the thickness of the wedge, a thicker wedge does result in an additional constant spatial offset ζ between the beams. A thicker wedge, however, also increases the negative impact of the wedge material.

Figure 3.14.: a.) Principle of a wedge-like electro-optical deflector with the following magnitudes: n_1- refractive index of surrounding medium. n_2- refractive index of the EOD material, Δn - refractive index change due to applied voltage, α - wedge angle and β- angle of incidence of the beam. The separation angle at the output is $\Delta\epsilon = \epsilon_2 - \epsilon_1$.
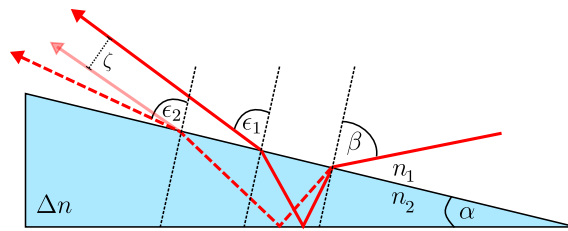
3.6.4. Piezoelectric Actuator Driven Mirror
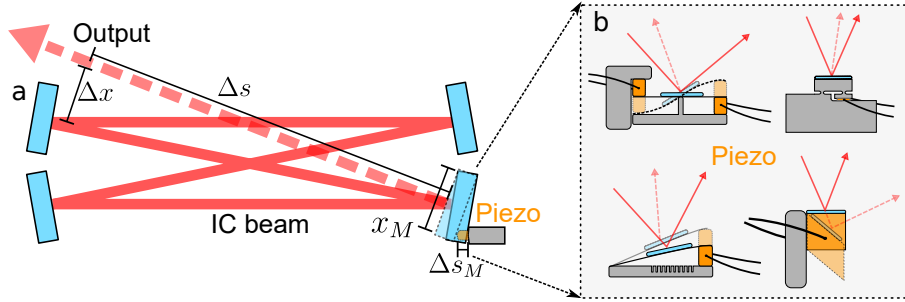
Figure 3.15.: a.) Possible implementation of a piezoelectric-driven mirror in an enhancement cavity. b) Possible mounting types for a piezoelectric driven tilting mirror [92].

One solution to dump pulses from an enhancement cavity might be a simple mechanical extraction via a fast tilting, deflecting mirror, as shown in Fig. 3.15a. This option was thoroughly investigated during this thesis and many calculations where carried out resulting in a patent application [92]. While interesting for numerous applications, it is too slow for an implementation in most SnD-cavities. This can be shown by some simple calculations. To achieve a separation between the IC beam and the output beam of $\Delta x = 4\,\text{mm}$ after a distance of $\Delta s = 4\,\text{m}$, a mirror of length $x_{\text{M}} = 4\,\text{mm}$ needs to be shifted by

$$\Delta s_{\text{M}} = x_{\text{M}}\text{arctan}(\Delta x/\Delta s) \approx x_{\text{M}}\frac{\Delta x}{\Delta s} \approx 4\,\mu\text{m}\,.$$

Shifting one end of a mirror by Δs_{M} within t_{rise} would result in an acceleration of that mirror part of

$$a = \frac{1}{2}\Delta s_{\text{M}}/t_{\text{rise}}^2\,.$$

For a switching process within $t_{\text{rise}} = 100\,\text{ns}$, the acceleration would be as high as $a = 2 \cdot 10^8\,\frac{m}{s^2}$, leading to immense forces on the mirror segment. This does not even consider the deceleration in order to be at rest during the entire pulse duration. If the piezoelectric actuator could move that fast, it would still lead to an immense deformation of the mirror, due to the limited speed of the ultrasound wave in the mirror plane, delivering the movement of the piezoelectric actuator driven edge to the rest of the mirror surface. For the given mirror segment, this would take

$$\frac{x_{\text{M}}}{v_{\text{us}}} = \frac{0.004\,\text{m}}{5960\,\frac{m}{s}} \approx 670\,\text{ns}\,, \tag{3.37}$$

which is roughly one order of magnitude slower than the necessary 100-ns limit. Hence, for a 1-MHz cavity this would be acceptable.

There might be some room to reduce the acceleration by using multiple, tiltable mirrors or optimizing beam size and separation angle, however, it will not be sufficient to overcome these limitations. It becomes clear, that if a mechanical switch is going to be used, it needs to move continuously to avoid high forces due to acceleration.

3.6.5. Interferometric Switches

Interferometric switches, such as classical Michelson-interferometers [93] or more complex grating based designs [94], make use of interference effects to change the output port of a device. A simple Michelson interferometer is an interferometric switch. While there are different geometries, the demands on the switch are similar. It is usually necessary to shift a mirror by $\lambda/2$ or in advanced designs by $\lambda/4$ in order to switch. For $\lambda \approx 1\,\mu m$, this results in similar accelerations as calculated for piezoelectric-driven mirrors in the last paragraph. While the deformation of the mirror is not such a drastic influence in such a setup, the forces to accelerate the mirror as fast as necessary exceed the possibilities of piezoelectric actuators by far.

3.6.6. Frustrated Total Internal Reflection

If two elements, typically made of glass, with a higher refractive-index than the surrounding medium were brought closely together, frustrated total internal reflection (FTIR) on the touching surfaces could be achieved as depicted in Fig. 3.16. However, in order to switch with a contrast of 1:1000 between reflection and transmittance, the gap distance between the elements has to be changed from at least 0.7λ to almost 0λ [95]. Hence, in terms of velocity it is as challenging as the interferometric switches and also needs transmissive elements.
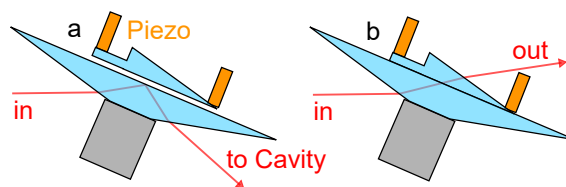
Figure 3.16.: a) Example of an FTIR-setup in the 'closed'-position (allowing total-internal reflection) and b) FTIR-setup in the 'open'-position (frustrating total internal reflection).

3.6.7. Phase-Shifted Input Pulse

Another concept for a switch, that does not need any element inside the cavity at all, can be a phase-shifted input pulse. However, this leads to significantly different design requirements on the cavity and eventually leads to a cascade of cavities instead of a single cavity. Thus, this method is classified as a different temporal pulse combining scheme and as such it is discussed in Sec. 2.3.3.

3.6.8. Conclusion

It can be concluded, that none of the available technologies suffices the high demands and hence, to truly scoop the full potential of SnD, in the long-term, a novel switching technique has to be introduced. Two potential candidates were investigated during this thesis and the results of those experiments are presented in Chap. 5.

4. Stack-and-Dump Experiments

4.1. Experimental Setup

4.1.1. Oscillator

The employed bulk-oscillator was set up during the early work for this thesis and later optimized, thoroughly explained and analyzed in [96] and [97]. A simple scheme of the setup is depicted in Fig. 4.1. The 80-MHz oscillator relies on a diode-pumped Yb:KYW crystal as gain-medium [98] and a saturable-absorber mirror (SAM) to allow for passive mode-locking [99].
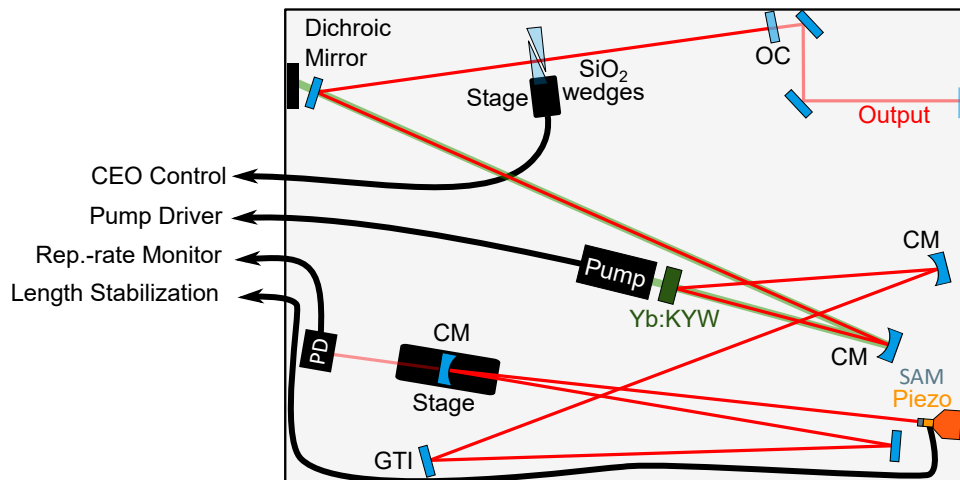
Figure 4.1.: Setup of the Yb:KYW oscillator. Three of the resonator mirrors were curved (CM) to control the beam size in the crystal and on the SAM. One of the mirrors was used to compensate the intracavity dispersion (GTI). The two end mirrors of the linear resonator were an output-coupler (OC) and a saturable-absorber mirror (SAM) mounted on a piezoactuator (Piezo).

The oscillator offered the possibility to easily change its length by up to $2\,\mu m$ via a small piezoelectric actuator that allowed to move the SESAM, which acted as one of the end mirrors of the linear resonator. This enabled stabilization of fast fluctuations with frequencies

48

up to ~1 kHz, while the slow drifts (a few Hz) were stabilized using a slow piezo with a large maximum displacement within the enhancement cavity itself. The repetition rate was monitored by a photodiode (PD), implemented behind one of the oscillator mirrors. Furthermore, two fused-silica wedges were installed to discriminated s-polarization and therefore ensure a linearly polarized output of the oscillator. Additionally, the wedges allowed to adjust the carrier-envelope-offset (CEO) during operation, by slightly changing the position of one of the wedges. This in- or decreased the material-thickness the beam transits and therefore changed the amount of the oscillators intracavity dispersion. This was not implemented as a part of an active stabilization scheme, but allowed to manually fine-tune the CEO of the oscillator to the one of the cavity during operation [100, 101].

4.1.2. Laser Amplifier System

The pulses delivered by the oscillator were sent through an AOM to enable adjusting the repetition rate. Afterwards, a grating-stretcher was employed to stretch the pulses to a duration of ~1.5 ns (measured at the -5 dB level of the maximum pulse intensity). A cascade of Ytterbium-doped fiber-amplifiers completed by a photonic crystal fiber (PCF: [13]) in a so-called large-pitch (LPF: [17]) design were employed. LPFs are optimized to withstand high-peak powers due to a large core area that reduces nonlinearities. In such fibers, 'single-mode' operation is ensured by gain-based discrimination of higher-order modes [?]. After amplification, the pulses had an energy of $E_{in} = 3\,\mu J$ at a repetition rate of 10 MHz corresponding to an average power of $P_{in} = 30$ W, respectively. The pulses were spectrally centered around $\lambda_0 = 1038$ nm and had a FWHM bandwidth of ~3 nm. The spectrum is depicted in Fig. 4.8b.

4.1.3. Cavity
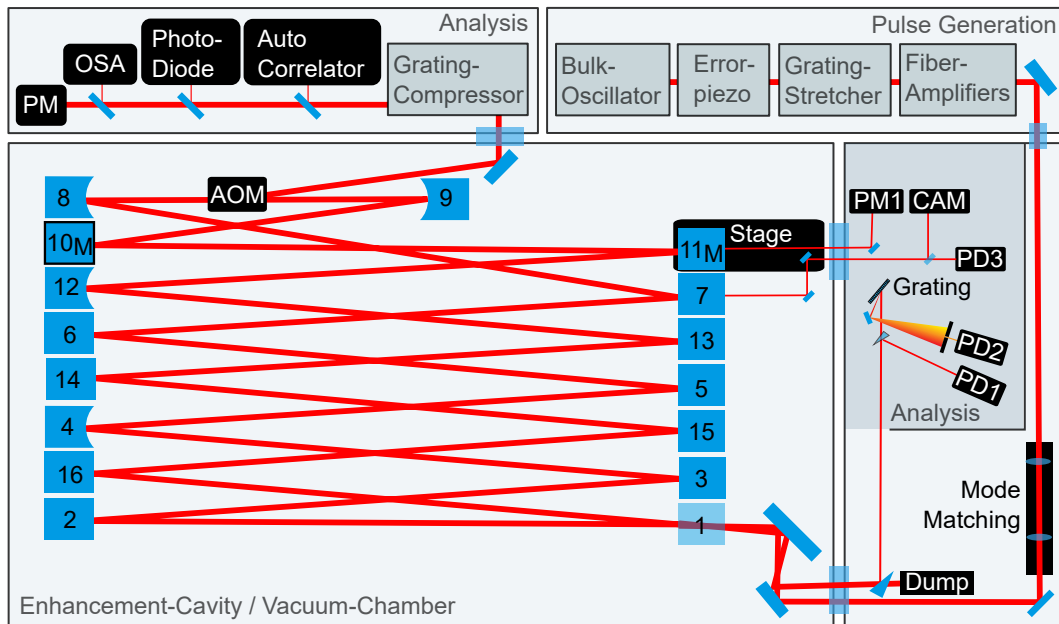
Figure 4.2.: Schematic of the enhancement-cavity. PD represents the photodiodes, CAM the camera and AOM the acousto-optic-modulator.

Figure 4.2 shows the entire laser system and cavity setup, including the monitoring section. The 30-m long ring-cavity was set up in a bow-tie design to keep the incident angles close to $0\,°$. Two softly focused 'cavity-arms' were generated by two curved mirrors with the radius of curvature of $R_{4,12} = 13.7\,\mathrm{m}$, resulting in the beam caustic shown in Fig. 4.3. A telescope was used to match the spatial mode of the incoming beam to the fundamental-mode of the EC, as described in section 3.2.4. This typically provided a measured overlap of $U = 80\,\%$, as defined in Eq. 3.18. The EC consisted of one input coupling mirror (1, $R = 99\,\%$) and 15 high-reflective (HR) mirrors (2-16). Two of the HR mirrors were curved (4, 12) in order to form a stable resonator (see Fig. 4.3). The x- and y-axis of the mirrors 10 and 11 were motorized to allow for readjustments while the cavity is evacuated. The mirrors 8 and 9, which were plane for the steady-state experiment, were later replaced by curved ones, once the AOM was inserted for the non-steady-state experiment (see Fig. 4.3). The transmitted fraction of the beam behind mirrors 7 and 11 was sent to diagnostics, such as a camera (CAM) and photodiodes (PD). PD1 is used to monitor the reflected signal, while PD3 monitored the transmitted field. PD2, the photodiode behind the grating, was used to generate an error-signal via the Pound-Drever-Hall stabilization scheme discussed in Sec. 3.4.1.
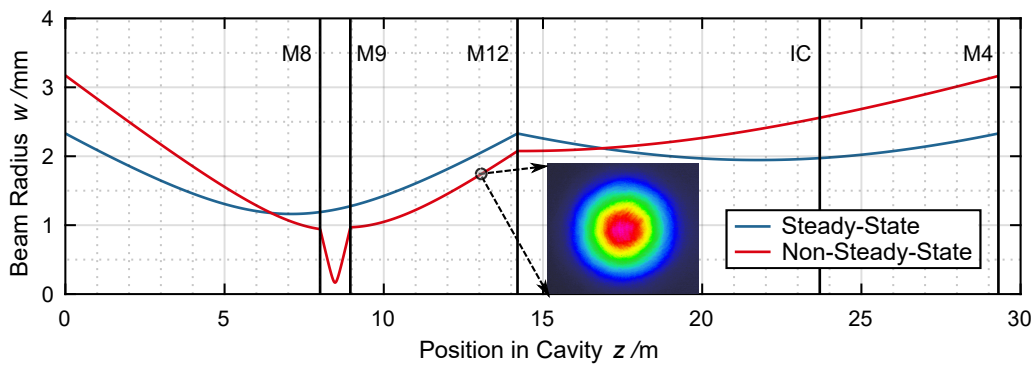
Figure 4.3.: Cavity caustic for the steady-state experiment (red) and the non-steady-state experiment (blue). The positions of the curved mirrors 4, 12 and 8, 9 (only for the non-steady-state experiment) are indicated by vertical lines. The inset shows the transmitted beam profile of the intracavity beam at an enhancement factor of 213 at the depicted position (the camera-position marked in Fig. 4.2).

4.1.4. Monitoring
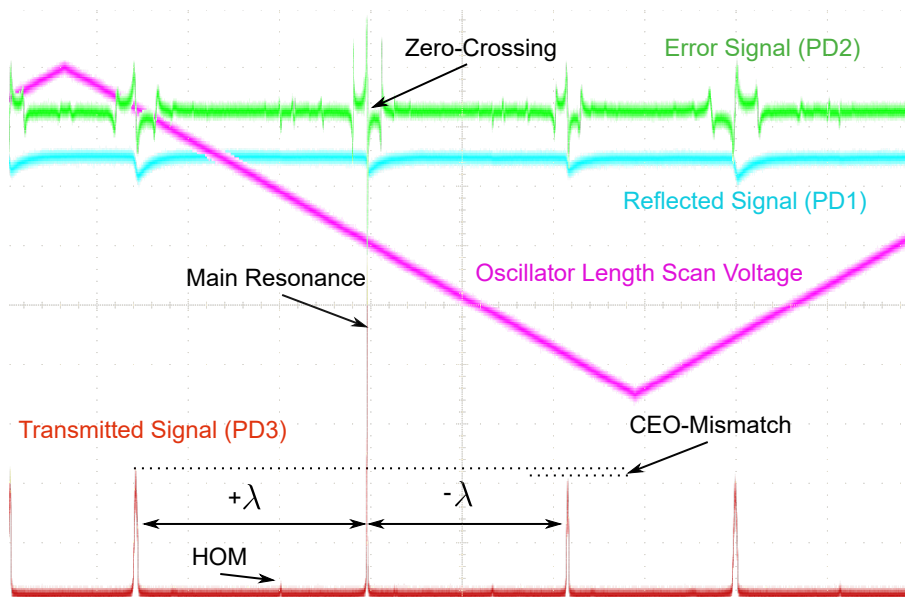
Figure 4.4.: Screenshot of typical oscillator traces as needed to adjust and monitor an enhancement cavity during the length-scan of the oscillator.

There are two key devices when adjusting and monitoring an enhancement cavity. First, a camera behind one of the cavity-mirrors, to adjust the spatial overlap and ensure the enhancement of the fundamental mode. Second, an oscilloscope that allows to observe a

life-feed of the levels of the transmitted signal behind one of the cavity mirrors, the reflected signal at the input-coupler and the error-signal. Such an exemplary oscillator trace during the so-called cavity-scan is shown in Fig. 4.4. During the scanning mode, the oscillator length is slowly modulated in order to make the resonances visible that occur when its length is matched to the enhancement cavity. The pink signal shows the voltage of the piezoelectric-actuator in the oscillator during this scan. The main resonance and two so-called side-resonances are visible in the transmitted signal (red). Such side-resonances occur when the oscillator is detuned by exactly one wavelength. It can therefore be concluded, that, during the scan, the peak-to-peak oscillator-length change is roughly 2.5λ. The main resonance is clearly higher than the side resonances and it is visible, that the $+\lambda$-resonance (the oscillator is longer than the cavity) is slightly stronger than the $-\lambda$-resonance (the oscillator is shorter than the cavity). This occurs if the CEO of the oscillator is not matched to the cavity and can be optimized by moving the wedges in the oscillator, as depicted in Fig. 4.1. Ideally, this would have to be actively stabilized, but the effect is very small for the pulse-durations in the herein presented experiments and, hence, an occasional manual adjustment via the wedges turned out to be sufficient. On the contrary, minimizing the energy, that is coupled into higher-order-modes (HOM), by optimizing the spatial cavity adjustment, is of paramount importance. While still visible in this example, they only contain a small amount of power. Naturally, when the cavity is in resonance, more power is coupled in and the reflection decreases, which is visible in the reflected signal (blue). Also, close to the resonances, error-signals as depicted in Fig. 3.10 can be observed (green). It is noteworthy, that the photodiode for the reflected signal is much slower than the one for the transmitted signal. Therefore, the depth of the dips does not deliver any information. However, when the cavity is locked, the reflected signal can be used to calculate the coupling-parameter K as discussed in Sec. 3.2.5.

4.2. Steady-state Operation

With this setup, an energy enhancement factor of $V = 213$ was achieved during steady-state operation, which corresponds to an intracavity average power of up to $6.4\,$kW. The enhanced pulses had an energy of $640\,\mu$J. The fundamental mode profile was verified by camera as shown in Fig. 4.3. The round-trip losses L within the cavity were estimated to be $0.22\,\%$ corresponding to average losses of $150\,$ppm and an average reflectivity of $99.985\,\%$ per mirror, respectively. At the time, the power enhancement was thought to be limited by the reflectivity of the input coupling (IC) mirror $R = 99$, which did not fulfill the impedance

matching condition ($R = 1 - L$) necessary for optimum steady-state enhancement [39]. However, this was not the design paradigm, since the IC was chosen to allow for a comparison to the upcoming non-steady state experiment. Here, a higher reflectivity would have been disadvantageous, due to the additional losses induced by the AOM employed as a switching device.

To verify if the reflectivity was truly the limitation, the steady-state experiment was later repeated with an IC with $R = 99.74\%$. Contrary to our expectations, this had detrimental effects and the achievable enhancement, in the otherwise identical setup, was reduced to 186. The explanation is rather obvious, considering that changing the reflectivity also increased the cavity finesse from ~ 514 to ~ 1309 and therewith also the requirements on stability of the oscillator and the lock. Hence, the actual limitation lies in the oscillator frequency comb-lines. Those had the same bandwidth for both experiments. For a cavity with a higher finesse, they were too broad compared to the bandwidth supported by the cavity. Therefore, the limitation for the enhancement factor is given by them and cannot be improved further without improving the oscillator first. This underlines the paramount importance of the oscillator in enhancement cavity setups. However, since this experiment aimed on extracting the enhanced pulses via an AOM, the losses were increased anyways, thus, reducing the cavity finesse and remove this limitation for now.

4.3. Non-steady-state Operation

For the dumping of pulses from the EC, an AOM was employed because of its simple implementation and fast switching times. The commercially available AOM (MQ80-A0.7-L1030.1064) offered an active aperture with a diameter of $0.7\,\text{mm}$ and had a thickness of $23.5\,\text{mm}$. The rise time of the acoustic waves is specified with $110\,\text{ns/mm}$ and therefore depends on the diameter of the beam d. The facets were antireflection-coated for wavelengths between 1030 and $1060\,\text{nm}$. The AOM introduced additional transmission losses of around 0.6% and consequently increased the overall round-trip losses to $L = 0.9\%$. This reduced the achieved steady-state enhancement to about 90. The cavity caustic was modified with respect to the steady-state experiment (see Fig. 4.3), in order to achieve an appropriate spot size in the AOM. The plane cavity mirrors 8 and 9 were replaced by concave mirrors with $R_{8,9} = 1000\,\text{mm}$, to obtain a focus with an $1/e^2$-diameter of $d = 0.3\,\text{mm}$ within the AOM. This led to negligible clipping losses while still providing a diffraction efficiency of around $\eta_{ext} = 72\%$. After adjusting the mode-matching telescope to the new caustic, the beam

overlap was comparable to the steady-state case around $U = 0.8$. Dumping via the AOM was triggered synchronously to the laser repetition frequency after an integer number of pulses, employing a gate function just wide enough for a single pulse. Using a TTL-trigger signal with the experimentally optimized duration of ~ 50 ns, single-pulse extraction was enabled. The intracavity and output signals are shown exemplary in Fig. 4.5 for 100 stacked pulses.
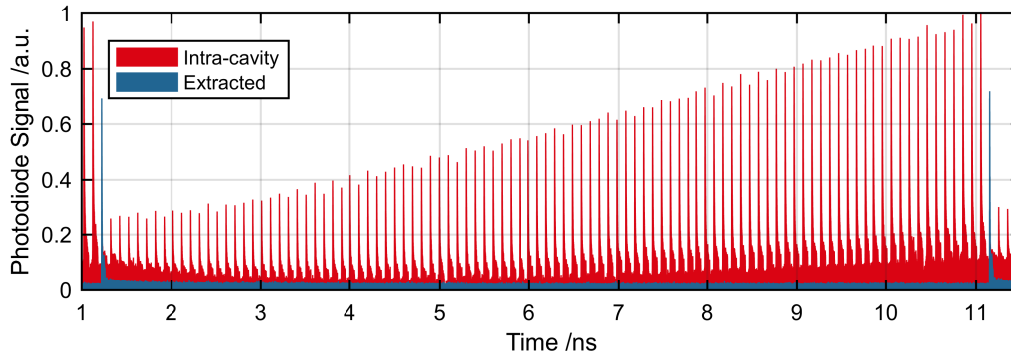
Figure 4.5.: Exemplary measurement of the entire pulse buildup within the EC using an AOM with $72\,\%$ diffraction efficiency and a switching rate of 100 kHz or 100 stacked pulses, respectively.

4.3.1. Variation of the Switching Rate

To systematically investigate the non-steady-state behaviour of the cavity with an AOM as a switch, multiple measurements were carried out. The switching-rate was set to 100, 60, 30, 15 and 10 kHz to allow for a meaningful comparison to the theoretical prediction. Fig. 4.6 shows a plot of the measured extracted enhancement and cavity efficiency over the number of stacked pulses and the switching rate, respectively. At first, the theoretical predictions made by the analytical approach, as shown in Eq. 3.27 were added to the plot and also presented in the corresponding publication [39]. Later on, the discovery that SPM already has a significant influence at these parameters encouraged an additional comparison of those results to the predictions by the numerical approach, as discussed in Sec. 3.2.2.
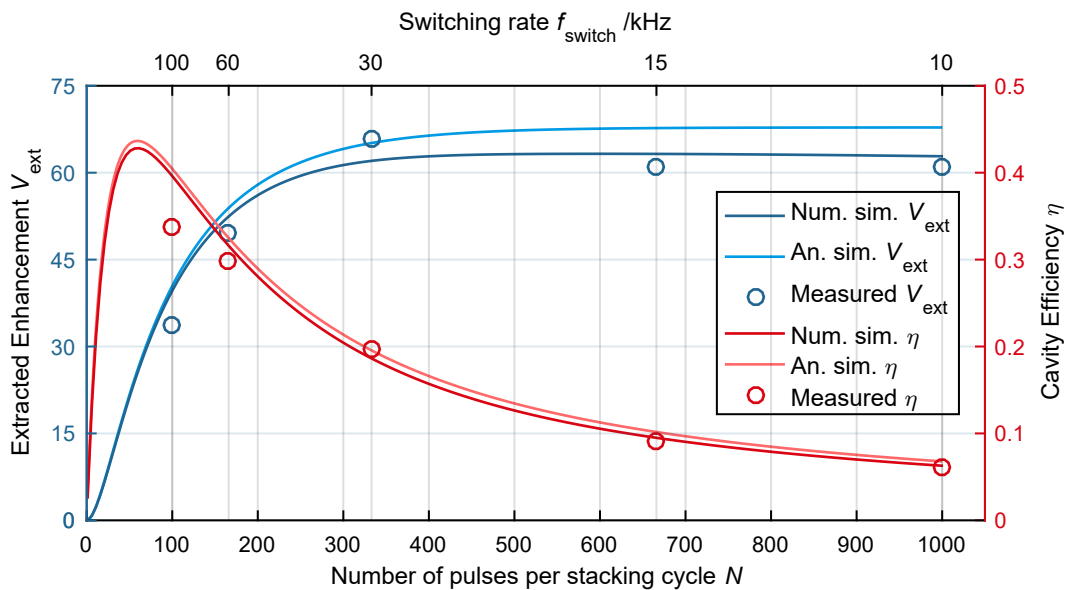
Figure 4.6.: Extracted enhancement and cavity efficiency for various switching rates along with the theoretical predictions, calculated numerically under consideration of SPM effects of in the employed AOM and analytically using Eq. 3.27. The parameters for the calculations were used as measured in the experiment. $U = 85\,\%$, $\eta_{\text{switch}} = 72\,\%$, $R = 99\,\%$ and $L = 0.9\,\%$.

In agreement to both theoretical models, up to 333 stacked pulses, a smaller number of stacked pulses led to a smaller extracted enhancement at a given input-coupler reflectivity. However, from here on an additional effect was detectable. It is noticeable that from this point on increasing the number of stacked pulses did not lead to improved values of extracted enhancement or pulse energy, respectively. First it was thought, that this was solely due to small uncertainties in the adjustment of the spatial and temporal overlap of the incoming pulses with the cavity pulse, thus, explaining the deviations from the theory. This may be caused by fluctuations of the spatial overlap between the cavity mode and the input beam, temporal fluctuations of the lock and fluctuations of the pulse-to-pulse stability of the oscillator. However, once SPM and dispersion inside the cavity were considered, a better explanation was found. As described in Sec. 3.3.4, a higher number of stacked pulses increases the influence of such effects, as it equals a higher number of average round-trips for the pulses. Obviously, the difference between the 1st pulse and the Nth pulse increases for higher N. Hence, considering SPM and the compensatory phase introduced by the stabilization scheme, the numerical model delivers the plots shown in Fig. 4.6. This explains the saturation and small decrease after ~ 500 pulses much better than the simple analytical model, neglecting SPM. The AOM created a GVD of $\backsim 520\,\text{fs}^2$ and the air in the cavity was responsible for

another $\backsim 490\,\text{fs}^2$. This was mostly compensated by employing one GTI mirror that removed $\backsim 1300\,\text{fs}^2$ GVD. Hence, all simulations neglected dispersive effects.

Another deviation from theory is visible at high switching-rates. The experimental performance is worse than the predictions, noticeable especially at $100\,\text{kHz}$. This is most likely caused by the stabilization of the oscillator to the cavity, which was slightly affected by the dumping process. At higher switching rates, the dumping occasionally led to a collapse of the lock, which most certainly decreased the measured output power and therefore the therefrom calculated extracted enhancement. If a cavity operation is desired at such high switching-rates, further optimization of the stabilization scheme may be advisable. This behaviour was not observed below $60\,\text{kHz}$.

The measured efficiency showed a clear maximum for 100 stacked pulses, reaching $34\,\%$. When the number of stacked pulses was increased, a saturation of the enhancement set in and as a result the efficiency dropped continuously. The efficiency as well as the extracted enhancement may be further optimized by adapting the input-coupler reflectivity for each switching-rate, as discussed in Sec. 3.3.2. For a given input-coupler reflectivity, the optimum working point regarding the switching-rate depends on whether the highest pulse energy or the highest efficiency is desired.

4.3.2. Characterization of the Output

A switching rate of $30\,\text{kHz}$ offered the highest extracted enhancement of 65, corresponding to an output pulse energy of $197\,\text{µJ}$. Fig. 5 shows the photodiode signal of the intracavity pulses and one output pulse of the system during this measurement. Afterwards, the dumped pulses were recompressed using a grating compressor with an efficiency of $80\,\%$ resulting in an energy of $160\,\text{µJ}$.
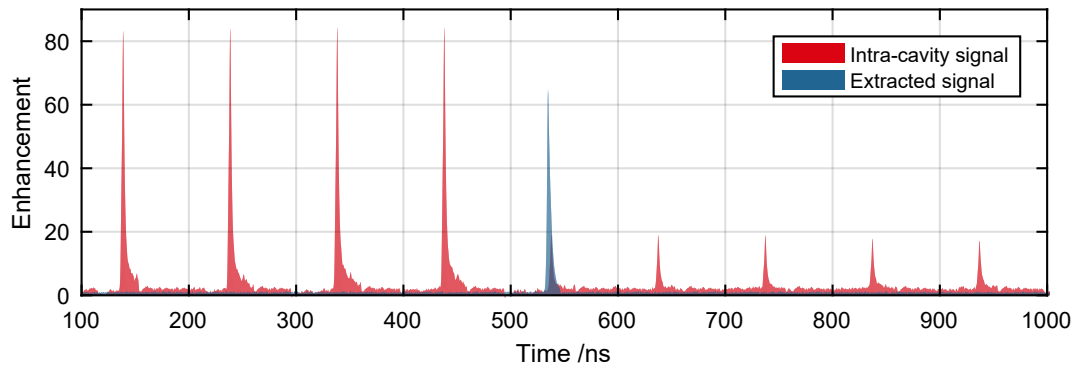
Figure 4.7.: Photodiode signals of the intracavity pulse (red) and of the output pulse (blue) for a switching rate of $30\,kHz$, revealing the extraction of a single pulse. A fraction of the pulse remains in the cavity due to the limited diffraction efficiency of the AOM.

Fig. 4.8 depicts a measurement of the auto-correlation and of the spectrum of the pulses. Additionally, a reference auto-correlation (Fig. 4.8a) was acquired in a single cavity-pass setup without any input-coupling mirror and therefore without any enhancement. Using the measured output spectrum and the spectral phase, the duration of the enhanced pulses was estimated to around $800\,fs$. This is only slightly longer than the input pulses, which is also confirmed by the almost identical spectrum of the input and of the extracted pulses (see Fig. 4.8b). According to Eq. 2.9, this corresponds to a pulse-peak power of around $190\,MW$.
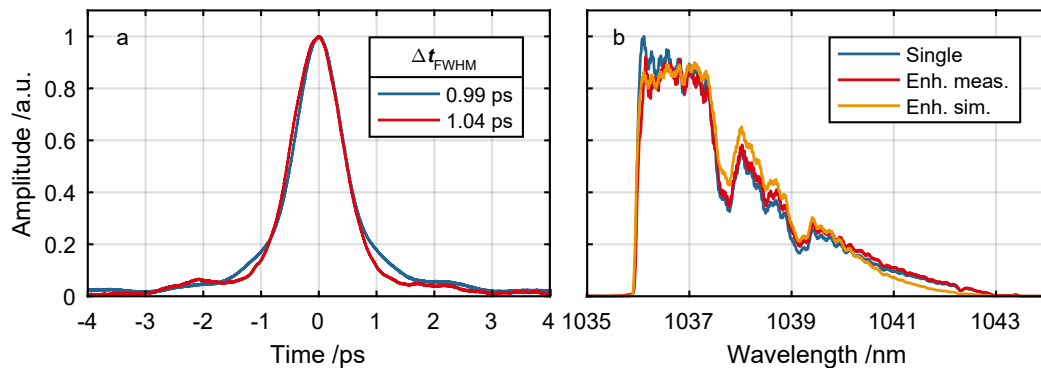
Figure 4.8.: a) Autocorrelation traces (AC) of a diffracted pulse in the single-pass setup (0th order of the AOM blocked) and of an extracted pulse during cavity operation. In the latter the shape is slightly different and the AC duration increased from 0.99 to $1.04\,ps$. The duration of the extracted pulse was estimated to be around $800\,fs$. b) Spectrum of the signal before the EC (blue), of the extracted pulse (red) and the spectrum predicted by the simulation (orange). All spectra clearly show the hard-cut of the stretcher at $\backsim 1036\,nm$.

4.3.3. Limitations of the AOM as a Switch

As discussed in Sec. 3.3.4 and specifically shown in Fig. 3.8, a higher input energy leads to a reduced enhancement as soon as the nonlinear effects caused by the AOM-material become significant. For 3-μJ input energy and a similar spectrum Fig. 3.8 shows a visible reduction of the possible enhancement. The influence is also observable in the difference between the simulations based on the analytical and numerical model, as carried out for the specific case of a switching-rate of $30\,\text{kHz}$. This is shown in Fig. 4.6. The laser-system used for this experiment was limited in terms of average power. Since further energy-scaling with an AOM as a switch did not promise any improvements, no upgraded laser-system was set up for this experiment and instead a different approach for energy scaling was evaluated by increasing the cavity length.

4.4. Cavity Length Scaling

One possibility to reduce the nonlinear phases acquired in the AOM, is to increase the spot size further, which leads to decreasing peak-intensities, as Eq. 2.22 shows. An improvement could be achieved by creating elliptically shaped beam at the position of the AOM, thus, only increase its size in the y-axis, perpendicular to the propagation direction of the ultrasound waves in the AOM (see Fig. 3.13). The resulting peak intensity reduction would scale linearly to the beam diameter expansion in that direction. A quadratic scaling could be achieved, if the beam diameter in both axis d_x and d_y would be increased. However, this would also result in a slower rise-time of the switching window, the AOM generates, since this scales linearly with the size of active area in x-direction (see Eq. 3.36). To allow for these slower rise-times, the feasibility of cavities with a length beyond $30\,\text{m}$ was investigated experimentally at the example of a 2-MHz cavity.

4.4.1. Setup of a 2-MHz Cavity

Since the available vacuum chamber only offered a length of $\sim 2\,\text{m}$, but a cavity length of $150\,\text{m}$ was to be covered, the cavity caustic needed to be folded ~ 70 times. Hence, to keep the complexity of the adjustment process acceptable and optimize the stability, a multi-pass-cell (MPC) needed to be introduced to the setup. The $10\,\text{MHz}$ cavity was therefore upgraded with a Herriott-type MPC [102] to add the missing optical-path-length. The MPC

consisted of three 3-inch mirrors, two concave and one plane. Changing the distance d_{MPC} between the curved mirrors either in- or decreased the number of round-trips in the MPC, thus, in- or decreasing the entire cavity length. With a correctly chosen incident angle and the distance between the two mirrors with a radius of curvature of $R_{\mathrm{MPC}} = 4147\,\mathrm{mm}$ set to $d_{\mathrm{MPC}} = 3765\,\mathrm{mm}$, it was possible to create the beam pattern shown in Fig. 4.9. The plane 3-inch mirror was used to fold the MPC.
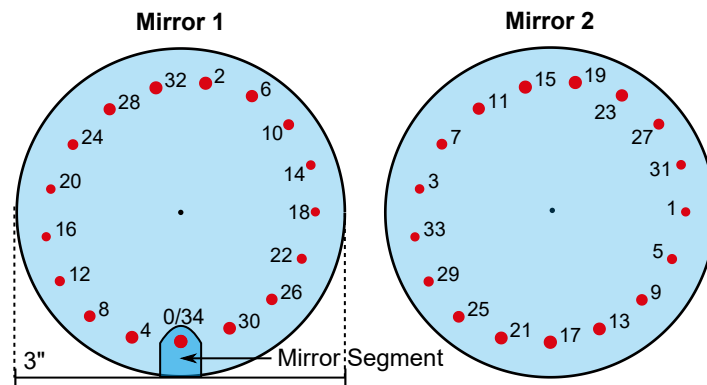
Figure 4.9.: Reflection pattern on the two curved mirrors of the multi-pass-cell. The 0th and 34th spot were reflected on a small mirror-segment, that was placed in front of the first curved mirror to allow coupling of the beam in and out of the multi-pass-cell.

The employed driving laser system was almost identical to the one in Fig. 4.2. Only the pulse repetition rate was reduced from $80\,\mathrm{MHz}$ as delivered by the oscillator down to $2\,\mathrm{MHz}$ to match the cavity. The cavity, however, was heavily modified to include the MPC as depicted in the setup scheme of the 2-MHz cavity in Fig. 4.10.
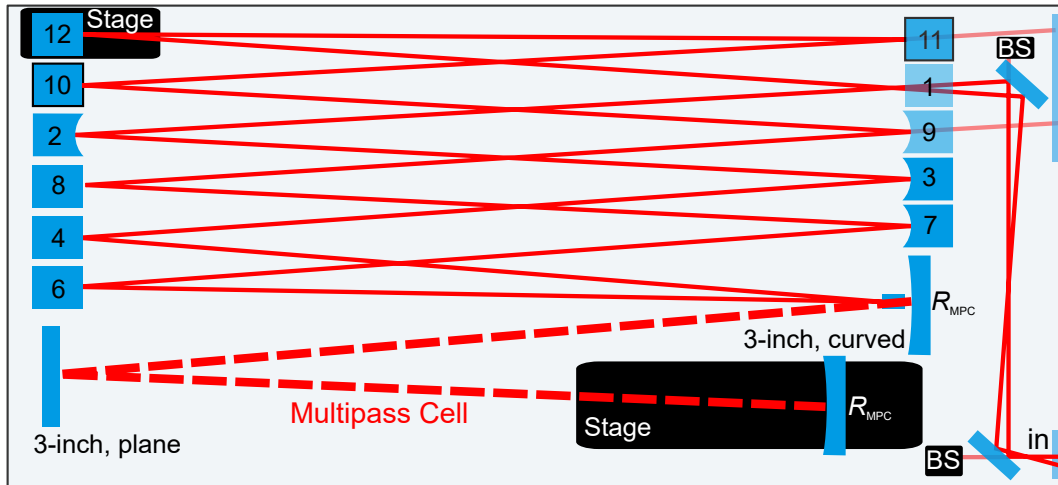
Figure 4.10.: Setup of the 2-MHz enhancement cavity. Mirror 3 and 7 are the same curved mirrors with $R_{3,7} = 13.7$ m from the 10-MHz setup in Fig. 4.2. Mirrors 2 and 9 are curved with $R_{2,9} = 10$ m to create the focus for the AOM. BS represents the cameras for the spatial beam stabilization of the incoming beam. A large stage is used to adjust the number of round-trips in the MPC, while a small stage is needed to make up for the change in optical path length after the transition to vacuum operation. The x- and y-axis of the mirrors 10 and 11 are motorized.

The cavity caustic including the MPC is shown in Fig. 4.11. The spot at the envisaged AOM position was increased to a diameter of ~ 1.3 mm, more than four times larger compared to the 10-MHz setup. However, in the first step, the cavity was setup without an AOM included to evaluate its steady-state behaviour. This experimental step was expected to be straight-forward but could not be carried out as planned. The next section will discuss possible reasons for that.
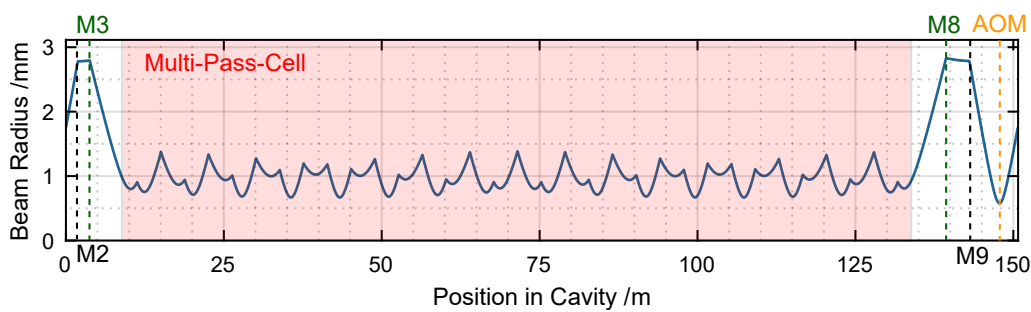
Figure 4.11.: Caustic of the 150-m long, 2-MHz enhancement cavity.

4.4.2. Discussion

Even after careful matching of the incoming beam to the calculated requirements, it was not possible to achieve a caustic that matched the simulations. The cavity caustic was changed multiple times, shortened or stretched, looking for a stable caustic. The beam parameters, however, could never be reproduced after one round-trip, thus, eventually leading to an explosion of the beam radius up to a point were the cavity mirrors could no longer fit it anymore and severe clipping occurred. Various reasons can be responsible for this undesirable behaviour.

- **Variations of the incoming Beam:** The incoming beam might be the problem. Variations of the radius and curvature from the envisaged values have a growing impact for longer resonators leading to a growing mismatch of the beam parameters after every round-trip.

- **Caustic Sensitivity:** In longer resonators, particularly angular deviations lead to increasing instabilities, due to alignment errors and thermal influences [103]. Hence, another explanation for the deviation of the caustic might be a sensible resonator design and particularly the design of the multi-pass-cell.

- **Surface Distortions on Mirrors:** Small distortions of the surface of the large MPC-mirrors might become significant, due to the large number of reflections over their surfaces. Thus, even usually negligible wave-front distortions, as induced by such a mirror surface, may eventually lead to large beam deformations over time. Furthermore, since mostly the outer sections of the mirror are used for reflection, the curvature may deviate slightly from point to point resulting in an overall deformation of the beam after a high number of reflections.

No stable 2-MHz cavity could be set up. Achieving a large number of round-trips, in a cavity design folded that often, is more challenging than anticipated. The employed optics need to be very carefully designed and chosen.

4.5. Energy Scaling

Even though further energy-scaling with an AOM is not feasible and longer cavities do not seem to be a promising alternative either, there are promising switching techniques as thoroughly discussed in Chap. 5, which could allow to further scale the output energy of a 10-MHz cavity. Hence, the first step towards such improved systems was to increase the

intracavity pulse energy to evaluate the energy-scaling limitations of the enhancement cavity itself in a completely passive and steady-state configuration. This can be done by increasing either the enhancement factor or the input energy. Since the enhancement factor was limited as discussed in Sec. 4.2 and a higher enhancement generally increases the effort that needs to be put into adjusting and stabilizing the cavity, the more promising approach was to scale the input energy. Fortunately, fs-laser systems with the highest average powers were available to be implemented for this experiment.

4.5.1. Upgrading the Laser System

In order to increase the available energy of the input pulses, the entire pre- and main-amplifier section was changed to deliver up to $100\,\mu J$ at $10\,MHz$ and $1\,kW$, respectively. The main amplifier stage consisted of 8 parallel fiber amplifiers and is explained in detail in [37]. However, the seed was delivered by the same bulk oscillator as before. The pulses were stretched to a duration of $\sim 1.5\,ns$ centered at $\sim 1038\,nm$ using the same stretcher as before.

4.5.2. Modifying the Setup for High-Power Operation

In order to handle the extremely high average powers during the enhancement, the entire cavity needed an overhaul. First of all, the beam path was improved in a way that any residual reflexes from AR-coated lenses or transmitted beams behind HR-coated mirrors could be dumped properly. Furthermore, the dump of the reflected signal port was enlarged and added to the cooling circuit. In front of every cavity mirror, a aperture of the mirror size was placed, so that any stray-light or clipped parts of the beam would not be heating the mirror mounts (see Fig. 4.12). Additionally, the operation of the cavity at such high power levels should only be done in vacuum, as otherwise dust would burn on the mirrors. Hence, the adjustments were carried out at low power levels ($\sim 1\,W$ input power) in air, before the chamber was evacuated (to a residual pressure of $\sim 0.4\,mbar$) and the input-power was increased further.
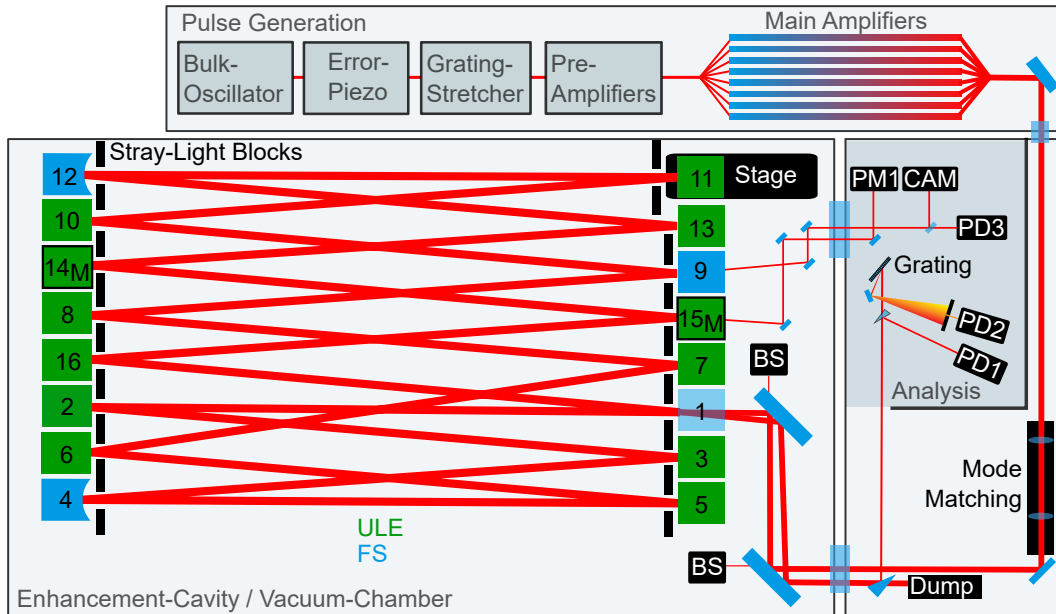
Figure 4.12.: Schematic of the enhancement-cavity. PD stands for photodiodes and CAM for the camera. The mirrors with ULE-substrates are depicted in green.

Since no AOM was to be included this time, the cavity was set-up to have a symmetric caustic (see Fig. 4.13), close to the stability center. This minimizes the effects of thermal lenses on the mode size, thus enabling a more reliable high-power operation. Besides two curved mirrors with $R_{4,12} = 13.7\,\mathrm{m}$ and the input coupling mirror with a reflectivity of $R = 99\,\%$, only plane mirrors with HR-coatings were employed. The beams transmitted through mirrors 9 and 15 are sent to diagnostics, such as a camera (CAM) and photodiodes (PD), analog to Fig. 4.2. To minimize thermal effects on the cavity caustic, it can be extremely beneficial to use ultra-low-expansion (ULE) substrates instead of fused-silica (FS) [38]. A thermally optimized setup would have consisted of only ULE-substrates and an input-coupler, made of sapphire or FS. However, no curved ULE-substrates were available to us and, therefore, the best mixture and positioning of the mirrors was simulated with the goal to keep the influence of the thermal deformations on the beam profile as low as possible, while embedding the FS mirrors into the design. This was done numerically using the code from [38]. The best solution was to use one further FS mirror, in addition to the input-coupler and the two curved mirrors, and arrange them symmetrically, as shown in Fig. 4.12. Most ULE mirrors were optimized for low-absorption and had a specified reflectivity of $R = 99.95\,\%$. However, due to limited availability, some with $R = 99.997\,\%$ and consequently higher absorption had to be used as well. All of these ULE mirrors were supplied by Manufacturer A ($\mathcal{A}$). The two curved (4,12) and the additional plane (9) FS-mirror were manufactured by Manufacturer B

($\mathcal{B}$).
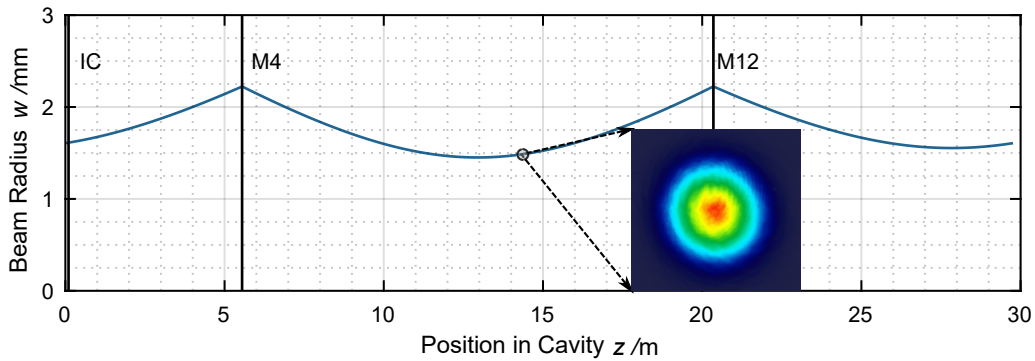
Figure 4.13.: Cavity caustic of the setup optimized for high average powers. The inset shows the transmitted beam profile of the intracavity beam at an enhancement factor of 121 at the depicted position (at the camera-position marked in Fig. 4.12).

4.5.3. Results
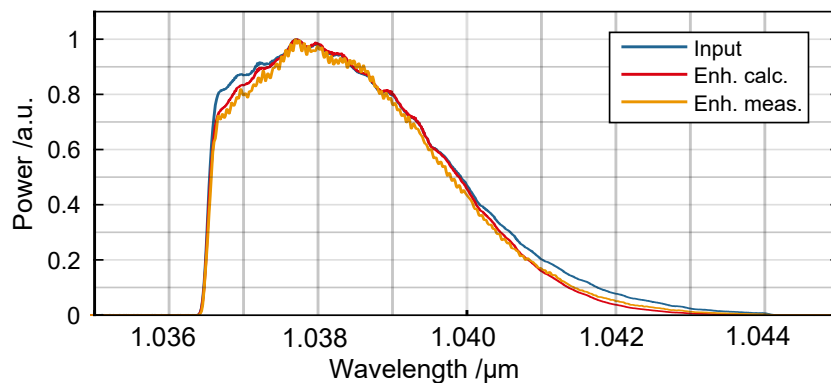
Figure 4.14.: Measured spectra of the input beam and the enhanced beam and the calculated spectrum for $V = 121$, assuming a residual dispersion of $400\,\mathrm{fs}^2$ due to the cavity mirrors.

When seeding $239\,\mathrm{W}$ into the cavity, this setup allowed for an enhancement factor of $V = 121$, leading to an intracavity average power of up to $28.8\,\mathrm{kW}$ and hence an energy of the circulating pulses of $2.88\,\mathrm{mJ}$. This is the highest pulse-energy, ever created in a femtosecond enhancement cavity. The round-trip losses L within the cavity were estimated to be $0.57\,\%$. The overlap was $U = 74.2\,\%$, therefore, the theoretically possible enhancement was 163. The enhancement is slightly lower than what was achieved in the earlier experiments, as presented in [39]. This is the case, as the mirrors were mostly changed from the ones optimized for

highest reflection ($R > 99.99\,\%$) to mirrors with $R \approx 99.95\,\%$, optimized for high-power performance. The spectrum of the enhanced beam looked almost identical to the input spectrum. It was only marginally narrower, which can be explained by residual intracavity dispersion, as the simulations shown in Fig. 4.14 underline. For these simulations, a GDD of $400\,\mathrm{fs}^2$ per round-trip was assumed, which leads to the measured spectral narrowing and also partly explains the imperfect overlap U. Such an amount of GDD can easily occur, if the 16 mirrors each add $25\,\mathrm{fs}^2$ in average. In a good agreement to that, the GDD of the employed mirrors was specified with $\sim 20\,\mathrm{fs}^2$. One could certainly optimize this further by adding a special mirror to compensate for the occurring amount of GDD. However, it did not cause a limitation to this experiment at the time. The actual limitations were much more severe and an attempt of an explanation will be given in the next section.

4.5.4. Limitations

a - Manufacturer C
b - Manufacturer A - 99.95%
c - Manufacturer A - 99.997%
d - Manufacturer B
e - Manufacturer B

200 µm
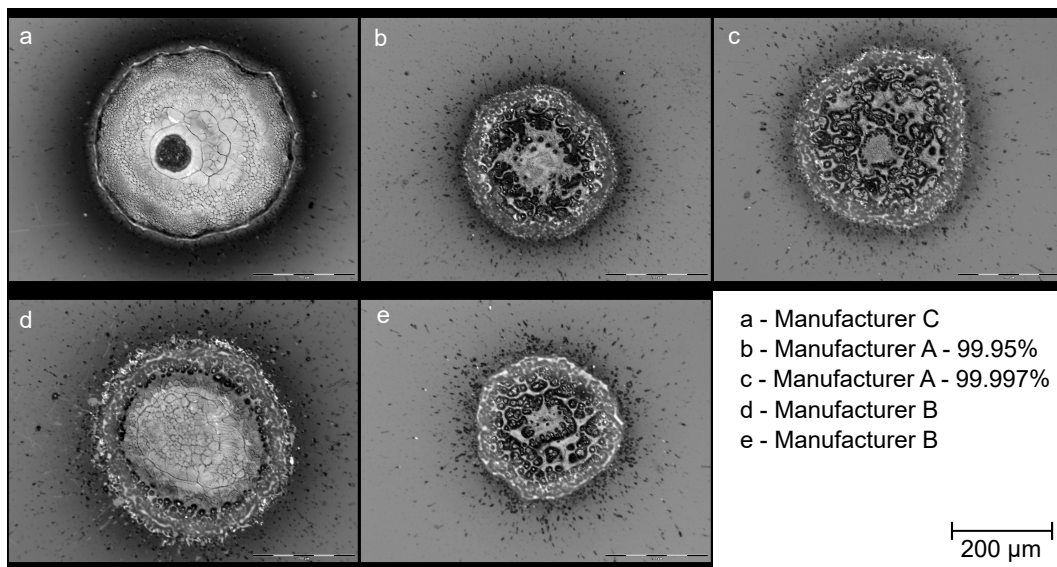
Figure 4.15.: Light microscope images of the damaged spots on different mirrors.

The available input power was as high as $1\,\mathrm{kW}$. Since only $239\,\mathrm{W}$ were being used, it is noticeable, that the limiting factors were neither the input power, nor the losses. At average intracavity powers above $20\,\mathrm{kW}$, mirror damage occurred repeatedly. The damage happened instantly when locking the cavity and was noticeable due to an immediate decline of the intracavity power level and corresponding rise of the reflected power level. The damaged mirrors could be spotted with an IR-viewer due to a significant increase in the amount of

scattered light. At first the mirrors from $\mathcal{A}$ with a specified reflectivity of $99.997\,\%$ were damaged repeatedly, so it was thought that the problem was the specific coating and all the effected mirrors were removed and replaced by mirrors from $\mathcal{B}$. At this point, the design considerations concerning the minimization of the mode expansion due to thermal issues were discarded, as they would not be an issue at this average power level and at this time no other HR-coated ULE substrates were available. However, most $\mathcal{B}$-mirrors also failed at around $24\,\text{kW}$, at the same point, were some mirrors supplied by a third manufacturer ($\mathcal{C}$) got destroyed. Beyond 30-kW of intracavity power, even the $\mathcal{A}$-mirrors with $R = 99.95\,\%$ were destroyed and the experiment was halted.

Fig. 4.15 shows some microscopic images of the affected surfaces. The varying pattern of the damaged surface did not help identifying the source of the damage. At times it looked molten, however, this may as well have happened after the original damage occurred and led to a locally higher absorption. The reason for the damage is therefore a puzzling question. As mentioned earlier, the highest achieved intracavity average power in a comparable cavity so far was $670\,\text{kW}$ by Carstens et al. [29]. They enhanced 10-ps pulses in a 250-MHz cavity. Tab. 4.1 shows a comparison of the parameters achieved in that experiment and the ones presented herein. The mirrors Carstens et al. employed, were the same type of mirrors from $\mathcal{A}$ with $R = 99.95\,\%$ as used for the results presented in this thesis. They were produced via ion beam sputtering [104], which typically produces the coatings with the best high-power durability. Generally, the reasons for damaged mirrors can be manifold. A brief overview of possible reasons is given in the upcoming section, to evaluate the cause of the observed destruction.

	Carstens et al.	Breitkopf et al.
Pulse Duration /ns	0.01	1.5
repetition rate /MHz	250	10
Average Power /kW	670	29
Pulse Energy /mJ	2.7	2.9
Pulse peak power /MW	250	1.8
Min. Spot Diameter on Mirror /mm	6	2.9
Max. Average Power Density /W/cm^2	240	44
Max. Peak Intensity /MW/cm^2	1800	55
Max. Energy Density /J/cm^2	0.0095	0.044

Table 4.1.: Key parameters for both experiments. Carstens et al. did use mirrors with the same specifications as the employed mirrors from $\mathcal{A}$ with $R = 99.95\,\%$.

LIDT   The laser-induced damage-threshold (LIDT) is typically given as either a power density (W/cm^2) or more commonly energy density (J/cm^2) and depends heavily on the wavelength as well as the pulse-duration and -shape and the spatial beam-profile. However, at this wavelength and with ion beam sputtered coatings, typical LIDT are in the range of 10 to $40\,\text{J/cm}^2$ [105], orders of magnitudes higher than determined in both experiments.. The question arises, if the apparently reduced LIDT in the presented experiment can be explained by any known scaling mechanism and under consideration of the different parameter sets of both experiments. Generally, it increases for longer pulses. More specifically, above a certain pulse-duration, it scales approximately proportional to the square-root of the pulse duration LIDT $\sim \sqrt{\Delta t}$. For $\lambda \approx 1050\,\text{nm}$, this threshold happens to be at $\sim 20\,\text{ps}$ for many surface materials as depicted in Fig. 4.16 [106, 107].
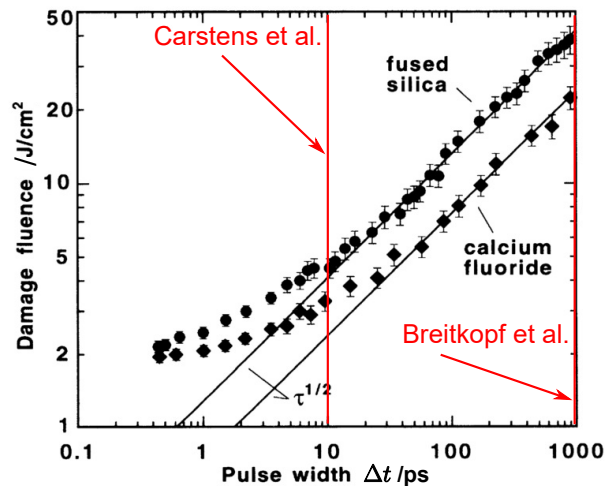
Figure 4.16.: Observed values of damage threshold at $1053\,\text{nm}$ for fused silica and CaF_2. Solid black lines are $\sqrt{\Delta t}$ fits to long pulse results. Red lines show the pulse durations of the two compared experiments (taken from [107]).

As a result, the LIDT in the herein presented experiment should be ~ 12 times higher compared to Carstens et al., while the actually occurring energy densities were only 4 times higher. Furthermore, it is known, that higher repetition rates decrease the damage-threshold [108]. This effect should also act to the benefit of the herein presented experiment, since the repetition rate in Carstens et al. was 25-times higher. No scaling mechanism can explain why damage should occur three orders of magnitude below typical damage thresholds in these coating materials. Furthermore, it is particularly peculiar, that this experiment was damage limited, while Carstens et al. were not. Therefore, it can be concluded, that the usual laser-induced-damage mechanism is most likely not the reason for the destroyed mirrors.

Outgassing   Contamination of the mirror surfaces can lead to a strongly reduced damage threshold of the coating materials. In air, small dust particles can create absorption centers, leading to heating and hence destruction of the affected spot. In vacuum, there are similar mechanisms with comparable effects. On one hand, slower heat conduction away from the mirror substrates can greatly reduce the amount of average power a mirror is capable of handling [109]. On the other hand, out-gassing of particles from any source in the vacuum chamber can create layers of gas molecules on the surfaces inside the cavity, again leading to higher absorption [110]. Both experiments were carried out in vacuum. For this experiment a pressure of $0.4\,\text{mbar}$ was sufficient to eliminate dispersion and scattering losses. Therefore, no components designed especially for ultra-high vacuum operation were used. This, however,

means, that out-gassing will have occurred to some extent, which might lead to damage of mirrors that have been in the chamber long enough to be effected. Nevertheless, some out-of-the-box mirrors got damaged during the experiment only a few minutes after they were placed in the cavity. It is very uncommon for out-gassing effects to occur after such a short time [109].

Coating Production Process   The production of HR mirrors is extremely sensible to the the cleanliness of the production facilities since parasitic particles could be imprinted in the coating. Therefore, the quality of the coatings can vary between different production charges. The employed $99.95\,\%$ mirrors from Manufacturer $\mathcal{A}$ were coated in 'full-charges'. According to a representative from $\mathcal{A}$, this can lead to a higher number of defects in the coating and the specified cleanliness is not guaranteed. The other mirrors were not specified for such high-powers, hence it might well be, that the replacement of all mirrors with cleaner ones with specified low defect-densities and optimized high-power capability, can lead to significantly higher intracavity powers before any damage occurs.

Unfortunately, no definite conclusion can be obtained from the high energy experiment. The mechanism that led to the unexpectedly early damage remains ambiguous. But independent of the damage source, it is fair to say to say that it could be fixable, i.e. by employing cleaner coatings or a better vacuum environment.

5. Evaluation of Novel Switches

5.1. Chopper Wheel

For the following section it is important to understand, that the design paradigm of the entire enhancement cavity setup was strongly influenced by the particle acceleration community and, especially, by the design proposals of Leemans et al. [5]. Hence, the design approach aimed for a $15\,\mathrm{kHz}$ output. The concept can however be easily adopted for different rotation frequencies and becomes even more feasible for output repetition rates $< 15\,\mathrm{kHz}$.

5.1.1. Working Principle
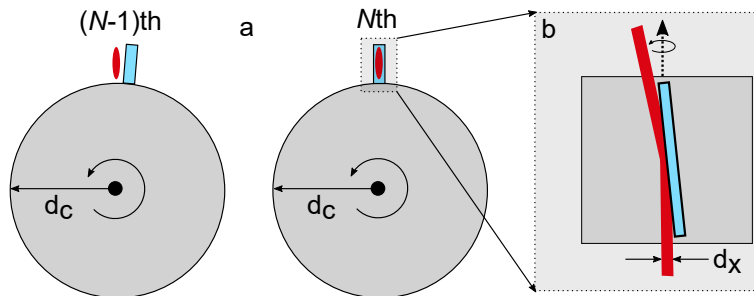
Figure 5.1.: Concept of a chopper-wheel employed as a pulse dumper for cavity enhancement. When a mirror, attached along the circumference of the chopper wheel, interrupts the optical path, the pulse is coupled out. There is no interaction with the cavity until the desired pulse energy has been built up. (b) Top view on the grazing-incidence reflection of the elliptically shaped beam spot on one of the mirror-segments. d_x is the width of the cavity beam in the x direction.

As described in [28], adopting a chopper wheel from those used for energy or polarization selection in particle beams [111], may result in a device capable of acting as a switch for SnD. The envisaged wheel has mirrors attached to its lateral facet and rotates in the vacuum chamber next to the cavity beam. For $(N-1)$ round-trips, while the enhanced pulse builds

up in the cavity, the wheel does not interact with the beam. When N pulses are stacked, the enhanced pulse is coupled out by a mirror attached to the wheel, which crosses the optical path of the beam. A schematic setup of this switch is depicted in Fig. 5.1. The required diameter of the chopper wheel d_c scales with the size of the beam d_x, the number of round-trips between two out-coupling events N and the number of mirrors attached to the wheel n_m. Assuming that a spatial seperation between the individual round-trips of $2d_x$ is sufficient to prevent significant clipping of the beam, the relation can be expressed as

$$d_c \geq \frac{2d_x N n_m}{\pi} \; . \tag{5.1}$$

This approximation is only valid for $\pi d_c \gg d_x$ or, in other words, when the curvature of the disc can be neglected compared to the small beam diameter. It is further important to understand, that n_m also represents the scaling of the switching rate. If the output is to be created with a 15-kHz repetition rate, the wheel would have to rotate with $15\,\text{kHz}$, unless multiple mirrors are attached to it. Commercially available chopper wheels as presented in [111] have diameters of $30\,\text{cm}$ and rotate at up to $f_{rot} = 1\,\text{kHz}$. Hence, assuming a 10-MHz cavity and 666 stacked pulses, 15 mirrors need to be attached to the wheel, in order to extract the pulses at $15\,\text{kHz}$. This is described by

$$f_{switch} = n_m f_{rot} = \frac{f_{rep}}{N} \tag{5.2}$$

Since such a design would require $d_x \approx 50\,\mu\text{m}$, the reflecting area has to be very narrow, in order to interact only during the 666th round-trip without disturbing the previous one. Fortunately, such thin mirrors are not necessary. If the mirror is broader and blocks the subsequent pulses, either a specially designed burst-mode laser input [81] could be employed, or the first few pulses in each stacking period are discarded, resulting in only a slight reduction of the efficiency (see Fig. 3.12). The peak intensities can be kept low, by shaping the beam elliptically at this position in the cavity caustic to increase the beam size. Additionally, by using the mirror under grazing incidence, the small beam diameter in the x-direction is projected on the large mirror surface (Fig. 5.1b) and the peak intensities are further reduced. Similarly to the cavity and the laser oscillator, the rotation frequency of the chopper wheel has to be stabilized and synchronized to an external clock. However, due to their high mass and the corresponding moment of inertia as well as their purely magnetic mounting, state-of-the-art chopper wheels typically possess only a slow timing jitter and a high stability of the rotation axis guaranteeing stable output-beam parameters (energy and pointing). The pointing stability is eventually limited by the positioning of the mirror segments on the

chopper wheel. This needs to be optimized during manufacturing, which is highly challenging. As a result, however, the largest deviations reoccur periodically with $15\,\mathrm{kHz}$ and can therefore be stabilized by an active beam stabilization mechanism that can be readily implemented after the output of the cavity. The mechanical vibrations introduced by the chopper wheel on the system are expected to be comparable to those of turbo-molecular vacuum pumps employed in standard cavity enhancement setups and, thus, uncritical for the optical alignment.

5.1.2. Fundamental Design Requirements

For an optimal implementation, the chopper wheel would have to meet three fundamental design criteria.

- **Rotation speed and size:** The wheel should rotate as fast as possible with the chosen size. This will be ultimately limited by the forces, that the disc-material can withstand.

- **Phase errors:** The rotation frequency needs to be sufficiently stable, to allow reproducible out-coupling of the pulses.

- **Exchangeable mirrors:** For a feasible implementation, the mirrors on the disc need to be replaceable. Otherwise, every mirror damage would require an entire new disc, resulting in substantial costs and effort.

Those design criteria were the basis of a feasibility study, carried out in order to evaluate the possibility to implement such a chopper wheel as a switch.

5.1.3. Brief Results of the Feasibility Study

The chopper wheel, as presented in [111], was originally built to select certain particles in a particle beam depending on their polarization or energy. Therefore, it had slits with a fixed position implemented at the outer end of the disc. This is much easier to realize, then adding an exchangeable, reflecting mirror to it. Hence, additional tests were necessary, in order to evaluate the feasibility of this concept. Additional studies were carried out by project-collaborators at the Central Institute for Engineering, Electronics and Analytics in Jülich, who also developed those choppers originally. They not only simulated the wheel's stress limits during rotation for different materials, but also realized numerical and experimental investigations of different ways to mount the mirrors. While the IAP developed the idea to use a chopper wheel as a switch, the experiments and simulations require an expertise and equipment not available to the IAP. They were therefore carried out entirely by the

collaborators in Jülich. However, as the results are not published anywhere, and can therefore not be referenced to, the outcome will briefly be presented for further discussions.

5.1.3.1. Rotation speed and size

The chopper presented in [111] was already limited by the tearing strength of the material. Higher speeds are therefore not possible at such diameters. A diameter of $30\,\mathrm{cm}$ at $1\,\mathrm{kHz}$ is hence the limit and only possible in the most advanced designs with an optimized mass distribution of the disc (see Fig. 5.2). Of course, if the diameter was reduced, the rotation frequency could be increased, but for the implementation as a switch this would not be beneficial.
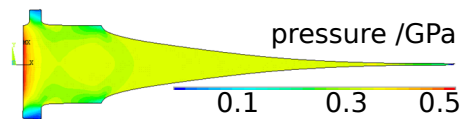
Figure 5.2.: Cross section of the chopper and the occurring stress at a rotation frequency of $1\,\mathrm{kHz}$.

5.1.3.2. Phase errors

The phase errors of a reference disc were measured to be $\pm 1\,\mathrm{ns}$ over 10 minutes during rotation at $1\,\mathrm{kHz}$ or $1\,\mathrm{ppm}$ (part-per-million), respectively. This equals a placement error of $\sim 1\,\mathrm{\mu m}$. Which would be tolerable for the proposed design. The larger error, however, occurs due to the placement of the mirrors on the discs outer surface. This misplacement error can be as high as $\pm 10\,\mathrm{\mu m}$. This would have to be compensated for by a smaller beam diameter d_x and consequently increased intensities on the mirror surface. While this is undesirable, it remains possible.

5.1.3.3. Exchangeable mirrors

Implementing the exchangeable mirrors is the most critical issue of the design study, as this is a fundamental modification from the original wheel design. Creating a connection that is sufficiently stable to withstand the extreme centrifugal forces, but at the same time allows to exchange the mirrors easily, states a contradictory design requirement. Hence, compromises have to be made. Three different connection-types are possible: plug connection (e.g. dove tail), soldering or glueing, as depicted in Fig. 5.3.
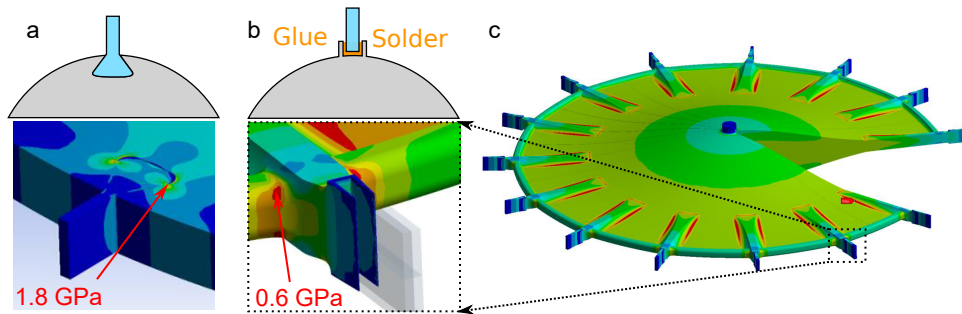
Figure 5.3.: a) Schematic and stress simulation of plug connection. b) Schematic and stress simulation of glued or soldered design. c) stress simulation of chopper design with stronger outer ring to hold mirrors.

The dove tail configuration was optimized to minimize the mechanic stress on the connecting surface between disc and mirror. However, in any configuration the peak pressure would be at least 1.8 GPa, too high for the material to withstand. A reduction of the mirror mass or rotation frequency would be required. Furthermore, a thickness of ~10 mm at the outer surface of the disc in order to provide room for the desired reflective surface, leads to a mass distribution of the chopper, that is unbearable for the mounting. Hence, for the soldered and glued approaches, the disc was changed to have a thick outer ring (see Fig. 5.3c) but otherwise similar mass distribution, as shown in Fig. 5.2. As a transmissive material for the mirror, only sapphire and diamond are possible, since for fused silica, the occurring centrifugal forces are higher than its tearing strength. However, as experiments showed, neither soldering or gluing are strong enough to hold a mirror of the proposed size at the proposed rotation speeds. All three concepts are of by a factor of ~ 2, not including any security margins.

5.1.3.4. Conclusion on Chopper Wheels as Switching Devices

While the realization of a chopper wheel with the given parameters is not possible, it is at the same time not that far off. Most limitations are only exceeded by a factor of 2 to 3. Hence, in a smaller version it might be implementable. However, in that case it is also less appearing since the requirements on the cavity design would grow and other problems would still remain. For example, the price tag of around 500 k€ makes it too expensive for most applications. Furthermore, adjusting and maintaining the device would be extremely complicated. The mounting does not allow for an exchange of the wheel without careful counterbalancing. This takes a lot of time and effort and also requires a specially trained engineer. However, thinking about the design of such a chopper wheel led to an extremely promising idea for a

modification of the chopper-wheel approach [112], which will be presented and thoroughly evaluated in the next section.

5.2. Rotating Cavity Caustic

5.2.1. Concept
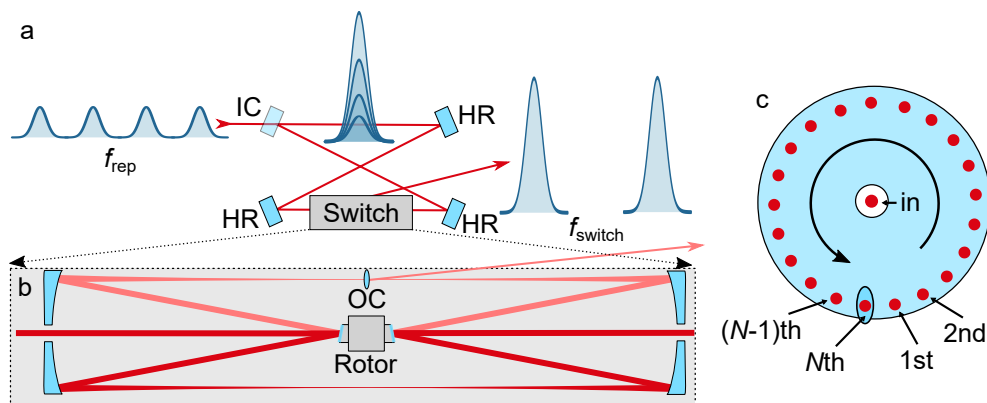
Figure 5.4.: a) Working principle of a stack-and-dump cavity. b) An ultra-fast rotor can, correctly implemented, serve as a switch. c) Front view on one of the curved mirrors, including the small mirror segment to extract the Nth pulse from the cavity. OC: Output-coupling mirror, IC: input-coupling-mirror, HR: highly-reflective mirror.

The key change of this approach in comparison to the chopper wheel is, that instead of rotating the mirror, which deflects the desired round-trip out of the cavity, the cavity caustic is rotated, while the mirror (OC) is fixed (see Fig. 5.4). To achieve this behaviour, the rotor and two large, curved mirrors with a hole in their center are embedded in the SnD cavity. Every round-trip inside the cavity is now rotated via the mirror mounted on the rotor and, thus, hits a different spot on the curved mirrors on both sides of the rotor. This allows to spatially separate the individual round-trips from one another. In the path of the the Nth round-trip, an output-coupling mirror is embedded, thus, extracting the enhanced pulse [112].

This setup reduces the requirements on the rotor significantly, since it can be a lot smaller. Such drives with a rotor size of ~1 cm can currently run at rotation frequencies up to $8.3\,\text{kHz}$ [113] with room for further improvement [114]. Like the chopper wheel approach, it is not only interesting for SnD, but also for the much broader field of regenerative amplifiers. On the downside, since not only the Nth, but every round-trip interacts with the rotating mirror, thereby generating a 'rotating cavity caustic', the rotation must be extremely stable. Hence,

the acquisition of data concerning the velocity and pointing errors of such a device was highly desirable. Precise measurements of these properties at ultra-high velocities have not been published before. Publications of measurements at slower rotation frequencies suggest that the relative velocity error can be well below $0.02\,\%$ at $\sim 67\,\mathrm{Hz}$ and above [115]. Since this idea arose only recently and the design of the rotor itself would have to be overhauled, it was not possible to implement it as suggested. However, a prototype of a rotor was available, that allowed to measure the velocity and pointing errors in a simple setup, in order to evaluate the feasibility of the concept for future implementation. The results will be presented in the remaining sections of this chapter. The technical details of the rotor can be found in [40].

5.2.2. Influence of Velocity and Pointing Errors
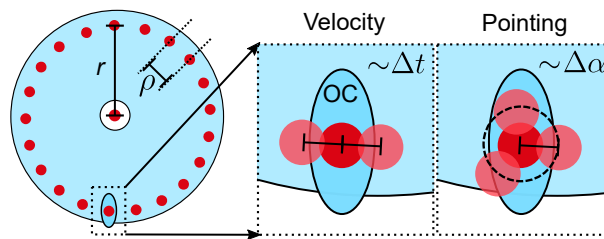
Figure 5.5.: Influence of velocity and asynchronous pointing errors on the position of the Nth round-trip on the out-coupling mirror.

Velocity Errors (Rotation Period Errors) The rotation period jitter Δt of the revolution n is defined as the deviation of the rotation period t_n from the average rotation period t_{avg}. It influences the position of the beam during the round-trip. If the deviation is too large, the outcoupling mirror (OC) might be missed. Smaller deviations can be counteracted by an increased mirror size or reduced beam radius on the output mirror. This deviation occurs in the direction of the rotation, as shown in Fig. 5.5. Assuming, that the separation between two subsequent pulses ρ must be at least $4w$ with w being the beam diameter in the plane of the output-mirror, we can define a relative deviation of $\Delta\rho/\rho \overset{!}{=} 0.1$ as the highest tolerable error, in order to still have a sufficient overlap with the OC. Hence, using $t_{\mathrm{avg}} \sim N\rho$, the relative error of the rotation period can be calculated as

$$\frac{\Delta t}{t_{\mathrm{avg}}} = \frac{\Delta\rho}{\rho N} \,.$$

(5.3)

The currently commercially available rotors rotate at up to $5\,\mathrm{kHz}$. In a 10-MHz cavity, this results in $N = 2000$. The relative velocity error is therefore allowed to be up to

$\Delta t / t_{\mathrm{avg}} = 50\,\mathrm{ppm}$. For $t_{\mathrm{avg}} = 1/f_{\mathrm{rot}} = 200\,\mu$s which leads to an absolute velocity error of $\Delta t = 10\,\mathrm{ns}$. This is the maximum time the rotation period is allowed to deviate between two round-trips and still enable undisturbed build-up and extraction of the enhanced beam. While this is valid for fast, jitter-like disturbances, changes over a longer time period can be potentially compensated for, by adjusting the cavity length. Larger long term drifts may therefore be tolerated.

Pointing errors Pointing errors can be distinguished in synchronous and asynchronous pointing errors. Synchronous pointing errors occur periodically and are synchronized to the current rotor position. Asynchronous errors lead to a different reflection angle at the same rotor position depending on the round-trip. In the worst case, they can even be entirely chaotic. Both have an impact when applying a rotor as a switch for enhanced pulses. If the pointing deviates asynchronous to the rotation, this can result in a varying position of the beam on the OC after each round-trip. Contrary to the velocity errors, the hereby caused deviation can be unidirectional, as depicted in Fig. 5.5. The tolerable amount of such pointing errors, is harder to estimated than the impact of velocity errors but a good explanation is given by Lilienfein at al. using the Fox-Li algorithm [116]. According to this paper, a synchronous pointing jitter of up to $10\,\mu$m is acceptable in order to only lose $14\,\%$ of efficiency and enhancement, respectively, due to a slightly decreased spatial overlap of the beam [112].

Since a vast amount of data points were measured to acquire data on the pointing stability and velocity errors for different scenarios, it is important to go into the details of the data analysis to understand the method. However, the results in regard to the usage as a cavity switch are briefly summarized and discussed in Sec. 5.2.5. Reading this section will also suffice to understand the conclusion.

5.2.3. Velocity Error Measurements

To allow for meaningful statements, it was necessary to measure the jitter of every revolution over a certain number of subsequent revolutions with a relative accuracy of $\Delta t / t_{\mathrm{avg}} \ll 50\,\mathrm{ppm}$. In order to measure such small deviations with a simple optical setup, a continuous-wave laser ($1064\,\mathrm{nm}$ central wavelength), the metal rotor with a polished surface, and a fast photodiode sufficed, as shown in Fig. 5.6.
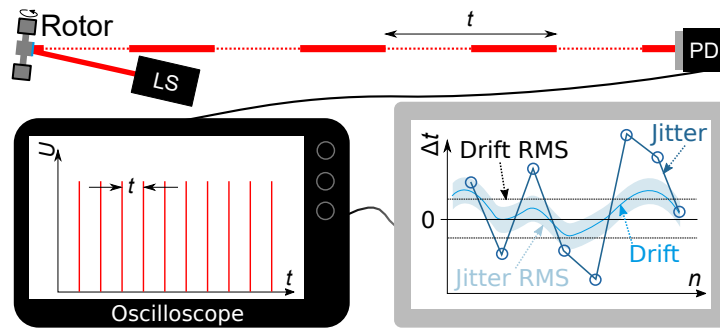
Figure 5.6.: Measurement setup consisting of a cw-laser (LS – Non-planar Ring Oscillator, $\lambda = 1064\,\text{nm}$), the rotor, a photodiode (PD) and an oscilloscope [40].

The laser beam reflected from the polished facet of the rotor hit the photodiode (PD) at a distance $s = 2\,\text{m}$ from the rotor once during every rotation period. For the measurements in vacuum the motor was placed in a vacuum chamber with a residual pressure of around $0.7\,\text{mbar}$, while the light source and detectors remained in an air environment. For these measurements, the distance was increased to $s = 3\,\text{m}$. The oscilloscope acquires a trace, containing the signal from a certain number of revolutions (Fig. 5.7a). For the measurements in air, the oscilloscope saved traces of up to $16 \cdot 10^6$ samples at rates of up to $30 \cdot 10^9$ samples/s. This was further optimized for the later carried out measurements in vacuum, allowing to acquire up to $64 \cdot 10^6$ samples. To record as many revolutions as possible, without compromising the measurement accuracy, the varying sample rates were chosen to achieve between $0.2 \cdot 10^6$ and $3 \cdot 10^6$ samples per revolution. The resulting time traces contained between 16 and 50 revolutions for the measurements in air, and between 20 and 320 revolutions for the vacuum measurements. The longer traces give better information about slow fluctuations, while the shorter traces offer a higher temporal resolution, which is particularly useful for the fast rotation speeds. Before extraction of the rotation periods from the acquired oscilloscope traces, two processing steps were carried out (Fig. 5.7).
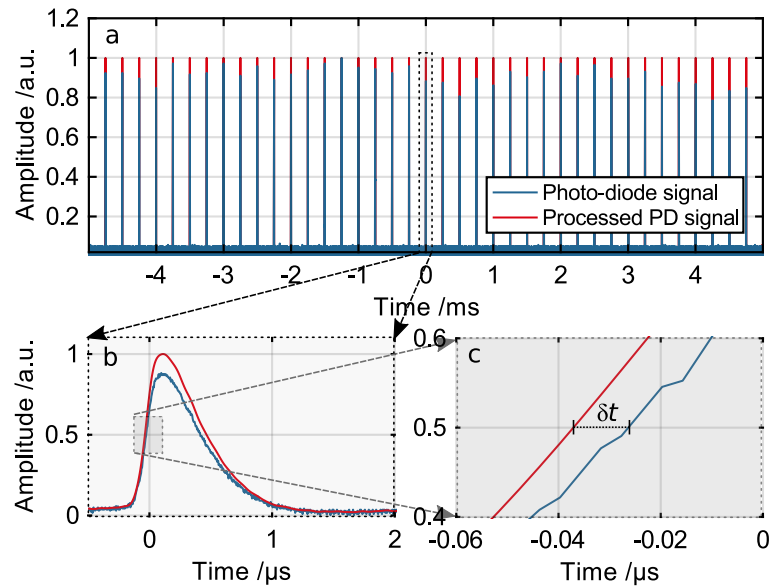
Figure 5.7.: Post-processing of the acquired traces, permitting to accurately calculate the time delay between the round-trips. The main goal is to remove the temporal error δt otherwise occurring when the trace is directly used without any post-processing [40].

First, the signal was filtered, employing a low-pass Fourier-filter with a hard-cut at $10\,\mathrm{MHz}$ to eliminate the noise on the PD signal, which could potentially cause problems for the rising-edge detection (see Fig. 5.7b and c). Second, since the peaks varied in terms of amplitude, due to beam pointing fluctuations between the revolutions (see next section) each peak was normalized to its maximum (visible in Fig. 5.7a). This step was important in order to avoid timing errors δt, when scanning for the temporal position of each revolution (see Fig. 5.7c). An algorithm detecting the rising edges passing 0.5 in the processed signal trace was used to calculate the time delay between all subsequent pulses and thereby the deviation of each individual rotation-period from the average period of this measurement. For practical reasons the terms 'jitter' and 'drift' are used (see Fig. 5.6). Drift is the moving average over 10 subsequent round-trip time deviations. RMS drift is the RMS-deviation of this drift from the mean revolution time. In many optical applications, those drifts can be actively compensated for. RMS jitter is defined as the RMS-deviation of the measured time-period from its corresponding drift and can typically not be compensated for. The bandwidth of the measured deviations was limited due to the limited number of measured revolutions. The fastest detectable disturbance occurred at the rotation frequency itself. Therefore, these measurements do not yield information on the long-term stability ($>$seconds) but give valuable information on short-term effects. Measurements were carried out in air (up to $4\,\mathrm{kHz}$, limited by rotor-heating) and vacuum (up to $5\,\mathrm{kHz}$) for 0.1, 0.2,

0.5, 1, 2, 3, 4 and $5\,\mathrm{kHz}$. For each rotation frequency 3 to 5 traces were acquired per medium, containing between 16 and 320 revolutions with varying sample-rates and rotation frequency. In addition, traces for the passively decelerating rotor, just after the motor was switched off, for different initial revolution speeds were measured. In Fig. 5.8 the transition between activated and deactivated motor drive in vacuum is shown. As soon as the motor was switched off the formerly dominant modulations disappeared and an unmodulated rise of the rotation period t was visible.
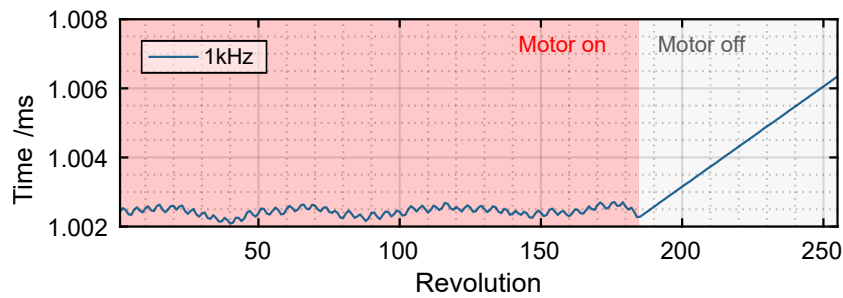
Figure 5.8.: Round-trip time with activated and deactivated motor, starting at a rotation frequency of $1\,\mathrm{kHz}$ [40].

After this slope was substracted, the resulting graph showed the behavior of the free-running rotor without a driving motor (right parts of each subplot in Fig. 5.9). Thus, the contribution of the motor drive to fluctuations of the rotation period can be distinguished from contributions of the bearing, the surrounding medium and measurement errors. To stay as close to the original rotation-frequency as possible, all presented measurements of the free-running rotor start directly after the motor drive was switched off. Figure 5.10 shows the relative RMS drift and jitter values for all measurements at each rotation frequency. In vacuum, the relative timing jitter as well as the drift decreased with increasing frequency from $\sim 3000\,\mathrm{ppm}$ to $\sim 100\,\mathrm{ppm}$, up to a rotation frequency of $\sim 1\,\mathrm{kHz}$. Between $1\,\mathrm{kHz}$ and $5\,\mathrm{kHz}$ it remained more or less constant. This applied to both the air and the vacuum measurements and with both activated and deactivated motor drive. With active motor, the air and vacuum jitter and drift measurements were of similar magnitude. In vacuum, switching off the motor drive reduced the velocity error by about 2 orders of magnitude. The free-running measurement gave an upper limit for the experimental error of the measurement method. At $5\,\mathrm{kHz}$ this was $\Delta t/t_{\mathrm{avg}} = 0.85\,\mathrm{ppm}$ (RMS) for the jitter, and $\Delta t/t_{\mathrm{avg}} = 0.15\,\mathrm{ppm}$ (RMS) for drifts. However, it is noteworthy that with deactivated motor the jitter was dominant, while for measurements with the activated motor, the drift was usually dominant. The large difference of the results with the activated and deactivated motor suggest that both jitter and drift in vacuum were mainly caused by the driving motor, while the contribution of the bearing was

negligible (Fig. 5.9a, b; Fig. 5.10). With active motor drive, the fluctuation in most vacuum measurements at all rotation velocities was dominated by a modulation, as illustrated in Fig. 5.9b. A possible explanation for this behaviour is given in [40].
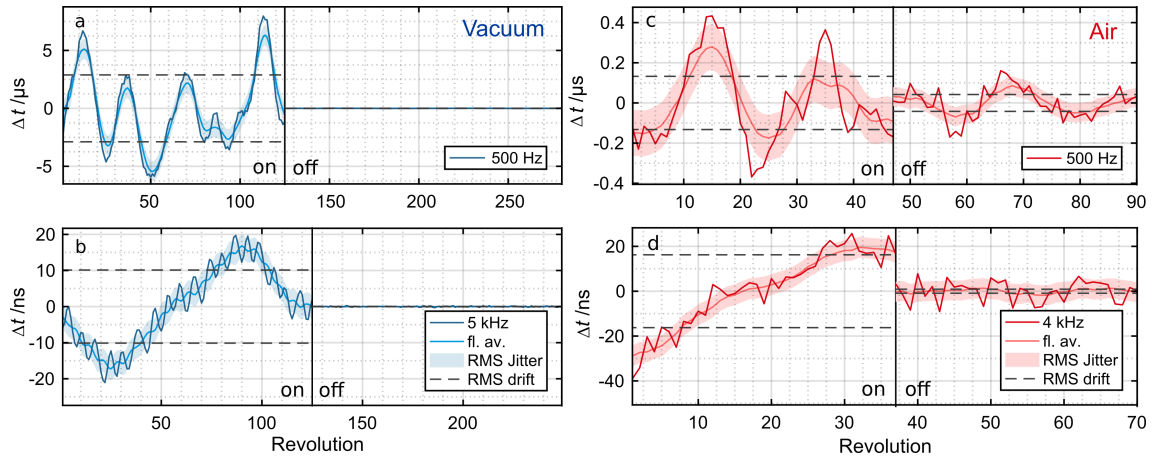
Figure 5.9.: Typical traces with active motor drive (left part of each subplot), and shortly after deactivation (right part of each subplot). The traces with deactivated motor were processed to remove the slope. Blue traces: Rotor in vacuum running at a) $500\,\mathrm{Hz}$ and b) $5\,\mathrm{kHz}$, respectively. Red traces: Rotor in air running at c) $500\,\mathrm{Hz}$ and d) $4\,\mathrm{kHz}$, respectively. Each floating average (fl. av. = drift) point was calculated taking 10 surrounding revolutions into account. Note that the y-axes of a) and c) are scaled in µs while b) and d) are scaled in ns [40].
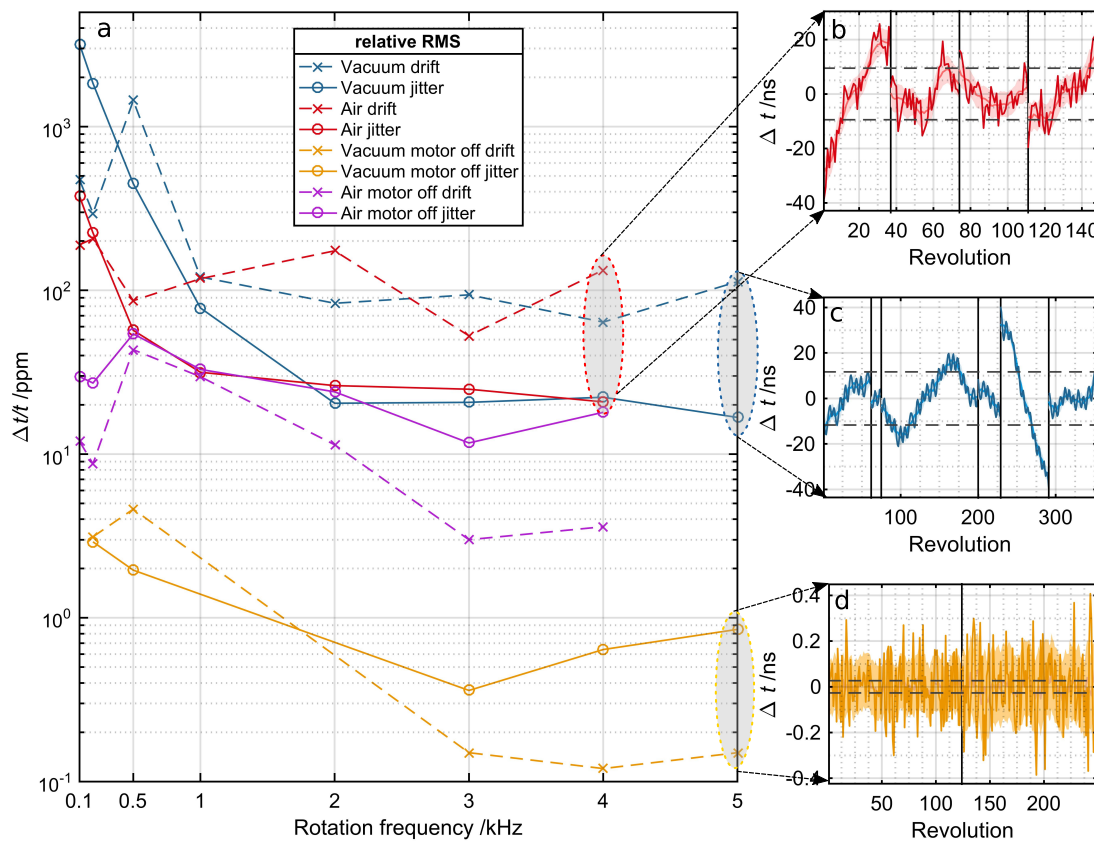
Figure 5.10.: a) Overview of maximum relative drift RMS and maximum relative jitter RMS for all acquired rotation frequencies in air (red), vacuum (blue), in vacuum with deactivated motor drive (yellow) and in air with deactivated motor drive (purple). (Connecting lines between measurement points were only added to improve visibility and represent no experimental data or fits) b) Combined traces of the measurements in air at $4\,\text{kHz}$ rotation frequency. c) Combined traces of the measurements in vacuum at $5\,\text{kHz}$ rotation frequency. d) Combined traces of the measurements in vacuum at $5\,\text{kHz}$ rotation frequency with deactivated motor, ring-down slope removed. The individual traces are visually separated by solid black lines in the plot [40].

In air, the magnitudes of both drift and jitter at frequencies of $2\,\text{kHz}$ and above were similar to the vacuum measurements. The change of the rotor behavior upon deactivation of the drive, however, was distinctly different. While the drift decreases by about one order of magnitude, the jitter level was similar for most rotation frequencies. This suggests that the jitter was caused mainly by either the interaction of the rotor with the surrounding air, or air fluctuations displacing the laser beam on its path to the photodiode. In general, the traces acquired in air do not contain the fast modulations observable at all rotation frequencies in vacuum, suggesting that the contribution of the motor drive was less significant than in the vacuum measurements. Counterintuitive, at lower frequencies (100 to $500\,\text{Hz}$) the

jitter and drift caused by the motor drive in vacuum was even higher than it was in air (see Fig. 5.9a/c and Fig. 5.10a). As Celeroton Ltd., the developer of the rotor, explained, these unexpected differences in jitter and drift between air and the vacuum measurements for low velocities were caused by the different modulation schemes of the motor coil, which was changed between the measurements [40]. This effect was therefore purely a matter of the motor control unit and can easily be fixed.

5.2.4. Asynchronous Pointing Stability

The setup to measure the pointing stability was very similar to the velocity error measurement setup. The photodiode was simply replaced by a high-speed camera, allowing measurements of the spatial beam displacement parallel to the rotation axis (see Fig. 7).
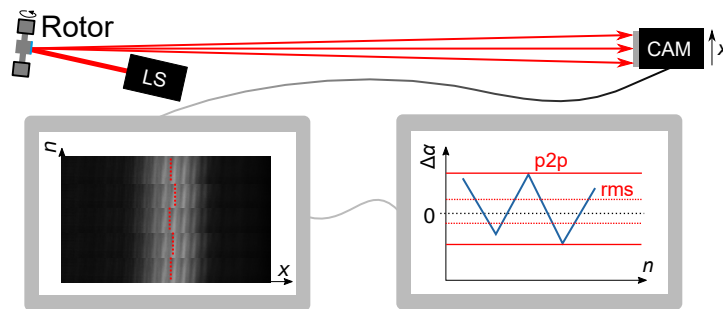
Figure 5.11.: Measurement setup consisting of a cw-laser (LS – Non-planar Ring Oscillator, $\lambda = 1064$ nm), the rotor, a photodiode (PD) and an high-speed-camera. The fringes are due to interference effects, caused by the glass window in front of the camera sensor [40].

The camera allowed to acquire up to 106 frames per second (fps). To make sure that only one round-trip is captured on a single frame, the frame-rate was chosen such that only every 10th frame contains an image of the beam for each rotation frequency. For every exposed frame, the vertical pixels were summed up and the center of mass of these sums in the horizontal direction was calculated and recorded as the deviation from the average beam position Δx. The angular deviation was derived from the beam position on the camera via $\Delta \alpha = \arctan(\Delta x/s)$. The beam position for >9000 revolutions was monitored at rotation frequencies of 0.1, 0.2 0.5, 1, 2, 3, 4 and 5 kHz. Since the beam position was recorded at one specific rotational angle of the rotor, only the asynchronous jitter was measured, while no information about pointing jitter that was synchronous to the rotation frequency was acquired. The results of the measurement in vacuum are plotted in Fig. 5.12.
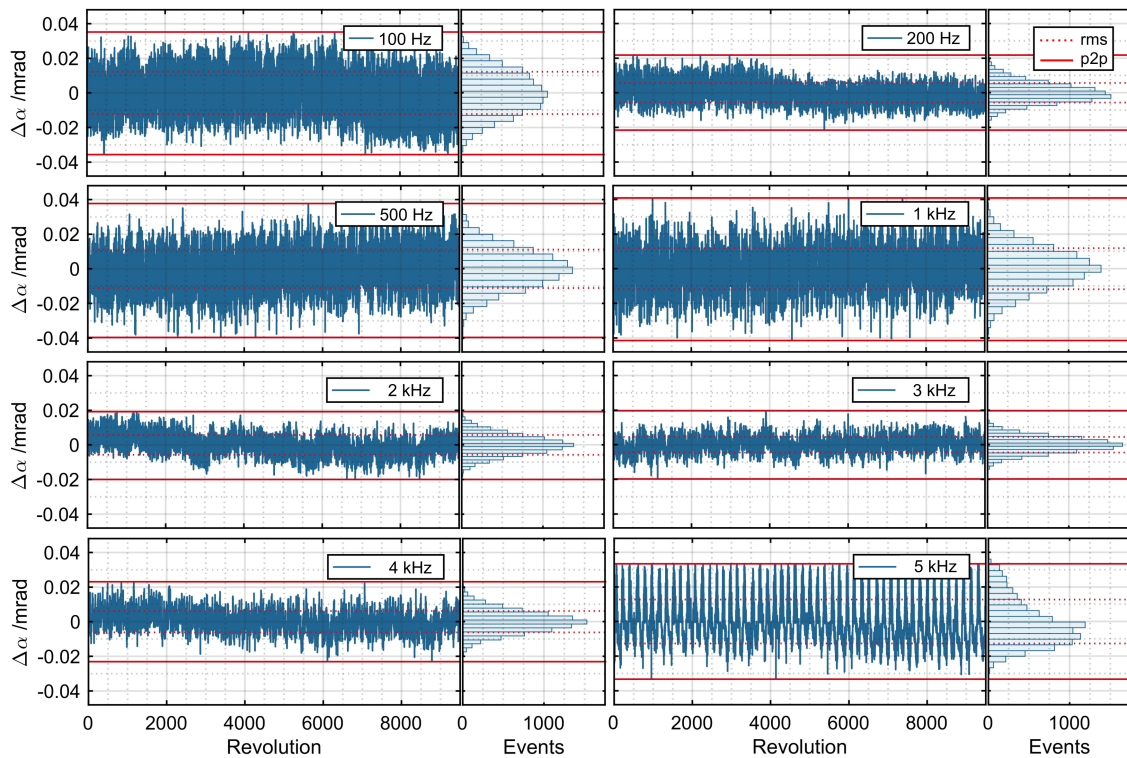
Figure 5.12.: Angular deviation of rotor position for >9000 subsequent revolutions at different round-trip frequencies. The red line shows the minimum and maximum deviation and the dotted red line shows the root-mean-square deviation. Each plot also depicts the statistical distribution of each angular deviation in a histogram. The center of mass of all revolutions at one fixed round-trip frequency was taken as the position were $\Delta\alpha = 0$ [40].

In all plots, the angular deviation from the average angle of the respective trace is shown, with all traces plotted to the same scale. The RMS angular deviations varied by a factor of ~ 2 for different rotation frequencies. The deviations were drastically reduced from 1 to $2\,\mathrm{kHz}$. In the bearing control, the position measurements were filtered with a notch filter with a corner frequency equal to the rotational speed. According to Celeroton, this notch filter was enabled for speeds higher than $1\,\mathrm{kHz}$ and therefore explains the reduction in the angular deviations. The traces exhibit a Gaussian distribution for all rotation frequencies except at the highest investigated frequency of $5\,\mathrm{kHz}$. Here, the distribution is asymmetric with respect to its center of mass, and the trace shows a periodic temporal pattern. This pattern may be explained by the gyroscopic couplings of the rotor, which were proportional to the rotation velocity. The higher the gyroscopic couplings, the lower the stability margin of the control. Figure 5.13 shows the offsets of the average angles for each rotation frequency together with error bars illustrating the RMS and peak-to-peak deviations. That offset was calculated as

the deviation of the center of mass for the pointing angle of each frequency from the average center of mass of all measurements. Due to changes of the setup, this was done separately for the measurements in air and vacuum and hence, the absolute offset is only comparable within one medium. The offset, as well as the RMS- and p2p-deviation, ware notably smaller for the vacuum measurements. This was, similar to the temporal jitter, most likely caused by air fluctuations which disturb the rotor. In air, the change of angular offset between different rotation frequencies was much larger than the deviations within the individual traces, for both the measurements in vacuum and in air (see Fig. 5.13). At rotation frequencies of 1 to $4\,\text{kHz}$, the offset of the vacuum measurement settled, and slightly changed again at $5\,\text{kHz}$. Such offsets were caused either by a static or a rotation-synchronous displacement of the rotor and were in any case well below $400\,\text{µrad}$.
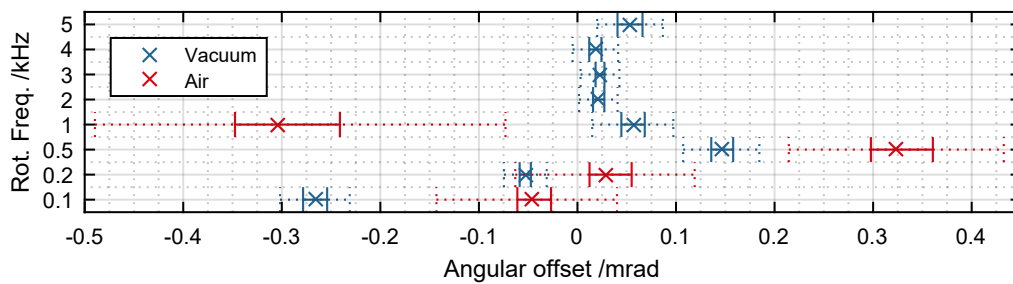
Figure 5.13.: Constant offset of the pointing angle and the RMS- and p2p-deviation depending on the rotation frequency for the measurements in vacuum and air [40].

5.2.5. Discussion

	Motor on	Motor off	Desired	Limit
Jitter (RMS)	3.4 ns	0.17 ns	1 ns	10 ns
Drift (RMS)	23 ns	0.03 ns	-	25 ns
Synchronous Pointing Jitter	-	-	5 µrad	20 µrad
Asynchronous Pointing Jitter	33 µrad	-	-	-

Table 5.1.: Comparison of measured values at $5\,\text{kHz}$ with the theoretically derived limits [112] for a possible implementation in a stack-and-dump cavity and the desired parameters for optimal operation. For both: jitter and drift, the highest values measured in any trace are shown in this table.

Velocity errors   The velocity error, in form of rotation-period jitter and drift of the investi-
gated high-speed self-bearing motor CM-AMB-400 in air and vacuum, decreased significantly
with increasing rotation frequency. The motor drive and its control are identified as the main
sources of rotation-period errors in vacuum with a maximum jitter of 3.4 ns (RMS) and a
drift of 23 ns (RMS) at the highest revolution speed of 5 kHz. The jitter was of similar mag-
nitude in both air and vacuum. While the rotation-period stability in air seemed to be limited
by air fluctuations, the measurements with deactivated motor suggest a large potential for
improvement in vacuum operation and the therewith achieved values of 0.17 ns were well
below the desired 1 ns value.

Pointing errors   The asynchronous beam pointing stability was significantly increased by
the operation in vacuum, with RMS and peak-to-peak values of 12 µrad and 33 µrad, re-
spectively, measured over ~ 10000 round-trips at 5 kHz. The rotation-frequency-dependent
angular shift may be problematic for applications which need to enable switching between
different velocities without being able to readjust for the resulting offset change. For SnD,
however, this is no problem.

Conclusion   The measurements as presented in this section, allow, for the first time, to
evaluate the velocity- and pointing-errors of the fastest available mechanical rotors. Not all
relevant parameters could be measured with the employed setup, especially the synchronous
pointing jitter. However, the measurement of the asynchronous pointing stability allows to
roughly estimate their magnitude. Furthermore, significant improvements can certainly be
made by optimizing the frequency stabilization electronic for the motor drive, which was,
due to a lack of measurement data, not yet optimized. As a result of our measurements,
this can and will be addressed in the next step. Hence, an implementation of a rotor-based
mechanical switch in a SnD cavity should be feasible in the future.

6. Conclusion and Outlook

The steady-state enhancement experiments carried out in this thesis using a 10-MHz cavity, allowed to demonstrate an enhanced intracavity pulse energy of $2.88\,$mJ, which is the highest energy in any femtosecond enhancement cavity. Furthermore, among the femtosecond enhancement cavities with a length of $30\,$m or more, the achieved enhancement factor of 216 states a new record [39]. These results proof the flexibility of enhancement cavities in regard to new applications.
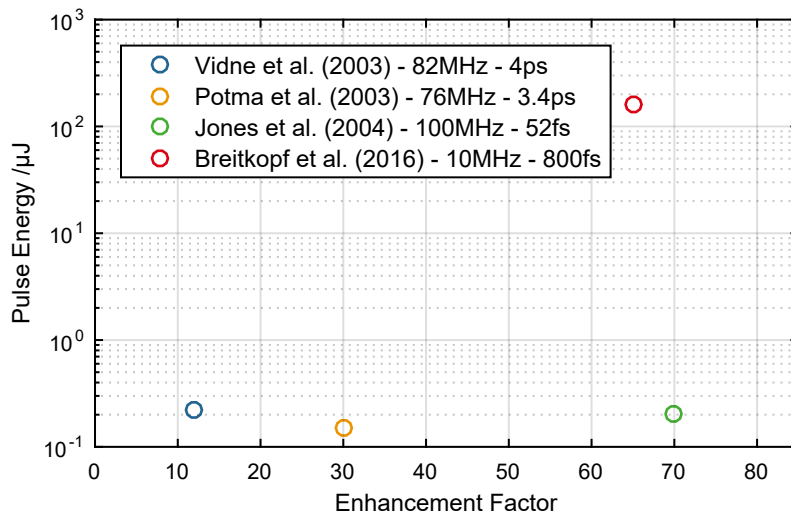
Figure 6.1.: Overview of all pico- and femtosecond stack-and-dump (non-steady state) experiments [34–36, 39].

Even more importantly, in non-steady-state operation, 160-µJ pulse energy at 30-kHz repetition rate with 800-fs pulse duration could be extracted using an acousto-optic modulator as a switch [39]. This is an 800-times higher extracted energy than what was ever demonstrated before with any stack-and-dumb (SnD) architecture [36], as Fig. 6.1 demonstrates. It shows a plot of the achieved pulse energy over the enhancement factor of all carried out SnD experiments. While increased pulse energies are the obvious emphasis of all temporal pulse stacking techniques, a higher enhancement factor relaxes the requirements on the driving

	Single [20]	DPA [25]	GTI [75]	SnD [39]	SnD [39]
Year	2011	2016	2016	2016	2016
Pulse Energy /µJ	2200	1600	4000	158	84
Repetition Rate /kHz	5	56	1	30	100
Pulse Duration /fs	480	262	330	800	800
Enhancement Factor	1	3.1	10	65	34
Stacking Efficiency	1	0.78	0.40	0.20	0.34

Table 6.1.: Overview of the record values of ultrafast fiber laser systems relying on temporally separated amplification. When spatially separated amplification was used as well, the output of one individual channel was calculated.

laser system and therefore offers more room for further pulse energy scaling with an acceptable amount of parasitic nonlinear effects. The dramatic improvement achieved within the work for this thesis was enabled by increasing the cavity length, to allow for larger beam sizes in the AOM and a therefore delayed onset of nonlinear effects as a limitation mechanism. However, scaling the cavity-length further to reduce the intensities in the AOM even more, sets extreme requirements on the the setup, both optically and mechanically and a stable system could not be demonstrated at $2\,\mathrm{MHz}$. Despite these important results, compared to other temporal combining techniques, SnD not yet enabled designing a laser system with unparalleled output parameters as Tab..6.1 clearly shows.

Due to the nature of the technique, achieving a relatively high enhancement factor is rather easy for SnD, compared to GTI and DPA. Furthermore, both DPA and GTI, need to put rigorous effort in extinguishing the post-pulses, which is something SnD solves intrinsically. For example, in the depicted GTI-experiment, the 26 post-pulses of the output signal had a combined energy as high as the main pulse. Stabilizing a growing number of cavities on each other is also increasingly challenging for the GTI approach and both GTI and DPA have serious issues with gain-saturation effects in the amplifier. Furthermore, SnD can offer superior repetition rates, if the amount of stacked pulses is chosen accordingly.

In summary, SnD clearly provides important benefits in terms of contrast and complexity, but unfortunately, the available switches, i.e. AOMs, limit the enhanced energy and therefore also the extractable energy. As a result, the achieved laser parameters cannot compete with other state-of-the-art temporal combining techniques in terms of energy, yet. To overcome the energy limitation in the future, novel switching concepts were developed and investigated as a part of this thesis. The idea of a rotating chopper-wheel [28], while disregarded for now,

due to complexity and severe costs, still eventually led to the extremely promising concept of employing a rotating cavity beam caustic, in order to allow for extremely fast and efficient switching and still maintain a relatively simple and compact setup [117]. The therefore required rotor technology was thoroughly investigated to evaluate whether the occurring velocity- and pointing-errors are within an acceptable range [40]. Since the measurements showed, that these errors are indeed very close to the desired parameters and appear to be currently limited by the electronic of the driving motor, it is absolutely feasible to implement such a switch as part of an enhancement cavity setup in the near future. However, setting up a long, high-finesse enhancement cavity with a rotating element in it, remains an enormous challenge and if a realization is possible, can only be finally evaluated in a further experiment. The first important steps were done, but whether SnD truly has the potential to fulfill the high expectations tied to it, is yet to be shown.

Bibliography

[1] M. Ferray, A. L'Huillier, and X. Li, "Multiple-harmonic conversion of 1064 nm radiation in rare gases," Journal of Physics B: At. Mol. Opt. Phys **21**, L31–L35 (1988).

[2] I. Will, H. I. Templin, S. Schreiber, and W. Sandner, "Photoinjector drive laser of the FLASH FEL." Optics express **19**, 23770–81 (2011).

[3] The LIGO Scientific Collaboration, the Virgo Collaboration, B. Abbott, R. Abbott, T. Abbott, F. Acernese, K. Ackley, C. Adams, T. Adams, P. Addesso, and E. al., "GW170817: Observation of Gravitational Waves from a Binary Neutron Star Inspiral," Physical Review Letters **119**, 161101 (2017).

[4] M. Chini, K. Zhao, and Z. Chang, "The generation, characterization and applications of broadband isolated attosecond pulses," Nature Photonics **8**, 178–186 (2014).

[5] W. Leemans and E. Esarey, "Laser-driven plasma-wave electron accelerators," Physics Today **62**, 44–49 (2009).

[6] T. Tajima and J. Dawson, "Laser electron accelerator," Physical Review Letters **43**, 267–270 (1979).

[7] S. M. Hooker, "Developments in laser-driven plasma accelerators," Nature Photonics **7**, 775–782 (2013).

[8] S. Döbert, "RF-Breakdown in High Frequency Accelerators," IEEE international power modulator conference pp. 60–63 (2004).

[9] S. Steinke, J. van Tilborg, C. Benedetti, C. G. R. Geddes, C. B. Schroeder, J. Daniels, K. K. Swanson, A. J. Gonsalves, K. Nakamura, N. H. Matlis, B. H. Shaw, E. Esarey, and W. P. Leemans, "Multistage coupling of independent laser-plasma accelerators," Nature **530**, 190–193 (2016).

[10] J. A. Abate, L. Lund, D. Brown, S. Jacobs, S. Refermat, J. Kelly, M. Gavin, and J. Waldbillig, "Active mirror : a large-aperture medium-repetition rate Nd : glass amplifier," **20**, 351–361 (1981).

[11] P. Russbueldt, T. Mans, J. Weitenberg, H. D. Hoffmann, and R. Poprawe, "Compact diode-pumped 1.1 kW Yb:YAG Innoslab femtosecond amplifier." Optics letters **35**, 4169–71 (2010).

[12] C. J. Koester and E. Snitzer, "Amplification in a Fiber Laser," Applied Optics **3**, 1182 (1964).

[13] P. Russell, "Photonic crystal fibers," science **299**, 358–362 (2003).

[14] T. Eidam, S. Hanf, E. Seise, T. V. Andersen, T. Gabler, C. Wirth, T. Schreiber, J. Limpert, and A. Tünnermann, "Femtosecond fiber CPA system emitting 830 W average output power." Optics letters **35**, 94–6 (2010).

[15] C. Jauregui, J. Limpert, and A. Tünnermann, "High-power fibre lasers," Nature Photonics **7**, 861–867 (2013).

[16] R. L. Farrow, D. a. V. Kliner, G. R. Hadley, and A. V. Smith, "Peak-power limits on fiber amplifiers imposed by self-focusing." Optics letters **31**, 3423–5 (2006).

[17] J. Limpert, F. Stutzki, F. Jansen, H.-J. Otto, T. Eidam, C. Jauregui, and A. Tünnermann, "Yb-doped large-pitch fibres: effective single-mode operation based on higher-order mode delocalisation," Light: Science & Applications **1**, 1–5 (2012).

[18] C. E. Cook, "Pulse Compression - Key to More Efficient Radar Transmission," Proceedings of the IRE **48**, 310–316 (1960).

[19] D. Strickland and G. Mourou, "Compression of amplified chirped optical pulses," Optics Communications **56**, 219–221 (1985).

[20] T. Eidam, J. Rothhardt, F. Stutzki, F. Jansen, S. Hädrich, H. Carstens, C. Jauregui, J. Limpert, and A. Tünnermann, "Fiber chirped-pulse amplification system emitting 3.8 GW peak power." Optics express **19**, 255–60 (2011).

[21] F. Stutzki, F. Jansen, A. Liem, and C. Jauregui, "26 mJ, 130 W Q-switched fiber-laser system with near-diffraction-limited beam quality," Optics letters **37**, 1073–1075 (2012).

[22] H. E. Bates, R. R. Alfano, and N. Schiller, "Picosecond pulse stacking in calcite," Applied Optics **18**, 947–949 (1979).

[23] M. Kienel, A. Klenke, and T. Eidam, "Analysis of passively combined divided-pulse amplification as an energy-scaling concept," Optics Letters **21**, 25379–25387 (2013).

[24] Y. Zaouter, F. Guichard, L. Daniault, M. Hanna, F. Morin, C. Hönninger, E. Mottay, F. Druon, and P. Georges, "Femtosecond fiber chirped- and divided-pulse amplification system," Optics Letters **38**, 106 (2013).

[25] M. Kienel, M. Müller, A. Klenke, J. Limpert, and A. Tünnermann, "12 mJ kW-class ultrafast fiber laser system using multidimensional coherent pulse addition," Optics Letters **41**, 3343 (2016).

[26] M. Kienel, "Power Scaling of Ultrashort Pulses by Spatial and Temporal Coherent Combining," Phd-thesis, Friedrich-Schiller-Universität Jena (2017).

[27] R. J. Jones and J. Ye, "Femtosecond pulse amplification by coherent addition in a passive optical cavity." Optics letters **27**, 1848–50 (2002).

[28] S. Breitkopf, T. Eidam, A. Klenke, L. von Grafenstein, H. Carstens, S. Holzberger, E. Fill, T. Schreiber, F. Krausz, A. Tünnermann, I. Pupeza, and J. Limpert, "A concept for multiterawatt fibre lasers based on coherent pulse stacking in passive cavities," Light: Science & Applications **3**, 1–7 (2014).

[29] H. Carstens, N. Lilienfein, S. Holzberger, C. Jocher, T. Eidam, J. Limpert, A. Tünnermann, J. Weitenberg, D. C. Yost, A. Alghamdi, Z. Alahmed, A. Azzeer, A. Apolonski, E. Fill, F. Krausz, and I. Pupeza, "Megawatt-scale average-power ultrashort pulses in an enhancement cavity," Optics letters **39**, 2595–8 (2014).

[30] I. Pupeza, S. Holzberger, T. Eidam, H. Carstens, D. Esser, J. Weitenberg, P. Rußbüldt, J. Rauschenberger, J. Limpert, T. Udem, A. Tünnermann, T. W. Hänsch, A. Apolonski, F. Krausz, and E. Fill, "Compact high-repetition-rate source of coherent 100 eV radiation," Nature Photonics **7**, 608–612 (2013).

[31] C. Gohle, T. Udem, M. Herrmann, J. Rauschenberger, R. Holzwarth, H. a. Schuessler, F. Krausz, and T. W. Hänsch, "A frequency comb in the extreme ultraviolet." Nature **436**, 234–7 (2005).

[32] R. Jones, K. Moll, M. Thorpe, and J. Ye, "Phase-Coherent Frequency Combs in the Vacuum Ultraviolet via High-Harmonic Generation inside a Femtosecond Enhancement Cavity," Physical Review Letters **94**, 193201 (2005).

[33] M. Couprie, D. Nutarelli, R. Roux, B. Visentin, L. Nahon, R. Bakker, A. Delboulbé, and M. Billardon, "Gamma rays produced by intra-cavity inverse Compton scattering of a storage ring free-electron laser," Journal of Physics B: At. Mol. Opt. Phys **32**, 5657–5667 (1999).

[34] E. O. Potma, C. Evans, X. S. Xie, R. J. Jones, and J. Ye, "Picosecond-pulse amplification with an external passive optical cavity." Optics letters **28**, 1835–7 (2003).

[35] Y. Vidne, M. Rosenbluh, and T. W. Hänsch, "Pulse picking by phase-coherent additive pulse generation in an external cavity." Optics letters **28**, 2396–8 (2003).

[36] R. J. Jones and J. Ye, "High-repetition-rate coherent femtosecond pulse amplification with an external passive optical cavity." Optics letters **29**, 2812–4 (2004).

[37] M. Müller, M. Kienel, A. Klenke, T. Gottschall, E. Shestaev, M. Plötner, J. Limpert, and A. Tünnermann, "1 kW 1 mJ eight-channel ultrafast fiber laser," Optics Letters **41**, 3439 (2016).

[38] H. Carstens, N. Lilienfein, S. Holzberger, C. Jocher, T. Eidam, J. Limpert, J. Weitenberg, D. Yost, A. Alghamdi, Z. Alahmed, A. Azzeer, A. Apolonski, E. Fill, F. Krausz, and I. Pupeza, "Megawatt-scale avergage-power ultrashort pulses in an enhancement cavity," Optics Letters **39**, 3–6 (2014).

[39] S. Breitkopf, S. Wunderlich, T. Eidam, E. Shestaev, S. Holzberger, T. Gottschall, H. Carstens, A. Tünnermann, I. Pupeza, and J. Limpert, "Extraction of enhanced, ultrashort laser pulses from a passive 10- MHz stack-and-dump cavity," Applied Physics B **122**, 297 (2016).

[40] S. Breitkopf, N. Lilienfein, T. Achtnich, C. Zwyssig, A. Tünnermann, I. Pupeza, and J. Limpert, "Velocity- and pointing-error measurements of a 300 000-r/min self-bearing permanent-magnet motor for optical applications," Review of Scientific Instruments **89**, 0631101–6 (2018).

[41] Träger, *Handbook of Lasers and Optics* (Springer, 2007).

[42] A. J. DeMaria, D. A. Stetser, and H. Heynau, "Self Mode-Locking of Lasers With Saturable Absorbers," Applied Physics Letters **8**, 174–& (1966).

[43] G. P. Agraval, *Nonlinear fiber optics* (Academic Press, 1995), 2nd ed.

[44] Z. Chang, *Fundamentals of attosecond optics* (CRC Press, 2011).

[45] A. E. Siegman, *Lasers* (University Science Books, 1990).

[46] I. Pupeza, "Power Scaling of Enhancement Cavities for Nonlinear Optics," Dissertation, LMU Munich (2011).

[47] R. W. Boyd, *Nonlinear Optics* (Elsevier Science, San Diego, 2003).

[48] E. Hecht, *Optics* (Addison-Wesley, 2001).

[49] A. Klenke, "Performance scaling of laser amplifiers via coherent combination of ultra-short pulses," Phd-thesis, Friedrich-Schiller-Universität Jena (2016).

[50] C. Danson, D. Hillier, N. Hopps, and D. Neely, "Petawatt class lasers worldwide," High Power Laser Science and Engineering **3**, e3 (2015).

[51] P. Wan, L.-M. Yang, and J. Liu, "All fiber-based Yb-doped high energy, high power femtosecond fiber lasers," Optics Express **21**, 29854 (2013).

[52] W. P. Leemans, R. Duarte, E. Esarey, S. Fournier, C. G. R. Geddes, D. Lockhart, C. B. Schroeder, C. Toth, J.-L. Vay, S. Zimmermann, S. H. Gold, and G. S. Nusinovich, "The BErkeley Lab Laser Accelerator (BELLA): A 10 GeV Laser Plasma Accelerator," **3**, 3–11 (2010).

[53] Y. Nabekawa, D. Yashitomi, T. Sekikawa, and S. Watanabe, "50-W average-power , 480-fs KrF excimer laser with gated gain amplification," **26**, 807–809 (2001).

[54] M. Ueffing, R. Lange, T. Pleyer, V. Pervak, T. Metzger, D. Sutter, Z. Major, T. Nubbe-meyer, and F. Krausz, "Direct regenerative amplification of femtosecond pulses to the multimillijoule level," Optics Letters **41**, 3840 (2016).

[55] H. Fattahi, A. Alismail, H. Wang, J. Brons, O. Pronin, T. Buberl, L. Vámos, G. Arisholm, A. M. Azzeer, and F. Krausz, "High-power, 1-ps, all-Yb:YAG thin-disk regenerative amplifier," Optics Letters **41**, 1126–1129 (2016).

[56] A. Klenke, S. Hädrich, T. Eidam, J. Rothhardt, M. Kienel, S. Demmler, T. Gottschall, J. Limpert, and A. Tünnermann, "Amplification System," **39**, 6875–6878 (2014).

[57] A. Klenke, S. Breitkopf, M. Kienel, T. Gottschall, T. Eidam, S. Hädrich, J. Rothhardt, J. Limpert, and A. Tünnermann, "530 W, 1.3 mJ, four-channel coherently combined femtosecond fiber chirped-pulse amplification system," Optics Letters **38**, 2283–2285 (2013).

[58] A. Klenke, E. Seise, S. Demmler, J. Rothhardt, S. Breitkopf, J. Limpert, and A. Tünnermann, "Coherently-combined two channel femtosecond fiber CPA system producing 3 mJ pulse energy," Optics Express **19**, 24280 (2011).

[59] E. Seise, A. Klenke, S. Breitkopf, J. Limpert, and A. Tünnermann, "88 W 0.5 mJ femtosecond laser pulses from two coherently combined fiber amplifiers." Optics letters **36**, 3858–60 (2011).

[60] M. Kienel, A. Klenke, T. Eidam, S. Hädrich, J. Limpert, and A. Tünnermann, "Energy scaling of femtosecond amplifiers using actively controlled divided-pulse amplification." Optics letters **39**, 1049–52 (2014).

[61] G. Mourou, B. Brocklesby, T. Tajima, and J. Limpert, "The future is fibre accelerators," Nature Photonics **7**, 258–261 (2013).

[62] F. Beier, C. Hupel, S. Kuhn, S. Hein, J. Nold, F. Proske, B. Sattler, A. Liem, C. Jauregui, J. Limpert, N. Haarlammert, T. Schreiber, R. Eberhardt, and A. T?nnermann, "Single mode 4.3 kW output power from a diode-pumped Yb-doped fiber amplifier," Optics Express **25**, 14892 (2017).

[63] E. Shcherbakov, V. Fomin, A. Abramov, A. Ferin, D. Mochalov, and V. P. Gapontsev, "Industrial Grade 100 kW Power CW Fiber Laser," in "Advanced Solid-State Lasers Congress," , vol. 5 (2013), vol. 5, p. 4.

[64] C. Jauregui, T. Eidam, H.-J. Otto, F. Stutzki, F. Jansen, J. Limpert, and A. Tünnermann, "Physical origin of mode instabilities in high-power fiber laser systems." Optics express **20**, 12912–25 (2012).

[65] H.-J. Otto, F. Stutzki, F. Jansen, T. Eidam, C. Jauregui, J. Limpert, and A. Tünnermann, "Temporal dynamics of mode instabilities in high-power fiber lasers and amplifiers," Optics Express **20**, 15710 (2012).

[66] C. Jauregui, H.-J. Otto, S. Breitkopf, J. Limpert, and A. Tünnermann, "Optimizing high-power Yb-doped fiber amplifier systems in the presence of transverse mode instabilities," Optics Express **24**, 7879–7892 (2016).

[67] J. Limpert, A. Klenke, M. Kienel, S. Breitkopf, T. Eidam, S. Hadrich, C. Jauregui, and A. Tunnermann, "Performance Scaling of Ultrafast Laser Systems by Coherent Addition of Femtosecond Pulses," IEEE Journal of Selected Topics in Quantum Electronics **20**, 1–10 (2014).

[68] J. E. Smith and G. S. Sohi, "The Microarchitecture of Superscalar Processors," Proceedings of the IEEE **83**, 1609–1624 (1995).

[69] W.-z. Chang, T. Zhou, L. a. Siiman, and A. Galvanauskas, "Femtosecond pulse spectral synthesis in coherently-spectrally combined multi-channel fiber chirped pulse amplifiers," Optics Express **21**, 3897 (2013).

[70] L. Siiman, W.-z. Chang, T. Zhou, and A. Galvanauskas, "Coherent femtosecond pulse combining of multiple parallel chirped pulse fiber amplifiers," Optics Express **20**, 18097–18116 (2012).

[71] C. Wirth, O. Schmidt, I. Tsybin, T. Schreiber, T. Peschel, F. Brückner, T. Clausnitzer, J. Limpert, R. Eberhardt, a. Tünnermann, M. Gowin, E. ten Have, K. Ludewigt, and

M. Jung, "2 kW incoherent beam combining of four narrow-linewidth photonic crystal fiber amplifiers." Optics express **17**, 1178–1183 (2009).

[72] H. Stark, M. Müller, M. Kienel, A. Klenke, J. Limpert, and A. Tünnermann, "Electro-optically controlled divided-pulse amplification," Optics Express **25**, 1049–1052 (2017).

[73] T. Zhou, J. Ruppe, C. Zhu, I.-N. Hu, J. Nees, and A. Galvanauskas, "Coherent pulse stacking amplification using low-finesse Gires-Tournois interferometers," Optics Express **23**, 7442 (2015).

[74] T. Zhou, "Coherent Combining of Optical Pulses in Spatial , Spectral and Time Domains," Dissertation, University of Michigan (2015).

[75] J. Ruppe, S. Chen, M. Sheikhsofla, R. Wilcox, J. Nees, and A. Galvanauskas, "Multiplexed Coherent Pulse Stacking of 27 Pulses in a 4+1 GTI Resonator Sequence," Lasers Congress 2016 (ASSL, LSC, LAC) **2016**, AM4A.6 (2016).

[76] W. Nagourney, *Quantum electronics for atomic physics* (Oxford University Press, New York, 2010).

[77] H. Carstens, S. Holzberger, J. Kaster, J. Weitenberg, V. Pervak, A. Apolonski, E. Fill, F. Krausz, and I. Pupeza, "Large-mode enhancement cavities," Optics Express **21**, 11606 (2013).

[78] O. Denchev and N. Gorunski, "Dynamically Stable Single and Multirod Linear Resonators with Large-Volume Fundamental Mode," **34**, 280–294 (2007).

[79] N. Lilienfein, H. Carstens, S. Holzberger, C. Jocher, T. Eidam, J. Limpert, a. Tünnermann, a. Apolonski, F. Krausz, and I. Pupeza, "Balancing of thermal lenses in enhancement cavities with transmissive elements." Optics letters **40**, 843–6 (2015).

[80] M. Yamashita, M. Ishikawa, K. Torizuka, and T. Sato, "Femtosecond-pulse laser chirp compensated by cavity-mirror dispersion," Optics Letters **11**, 504–6 (1986).

[81] S. Breitkopf, A. Klenke, T. Gottschall, H.-J. Otto, C. Jauregui, J. Limpert, and A. Tünnermann, "58 mJ burst comprising ultrashort pulses with homogenous energy level from an Yb-doped fiber amplifier," Optics Letters **37**, 5169 (2012).

[82] T. W. Hänsch and B. Couillaud, "Laser frequency stabilization by polarization spectroscopy of a reference cavity," Optics Communications **35**, 441–444 (1980).

[83] D. A. Shaddock, M. B. Gray, and D. E. McClelland, "Frequency locking a laser to an optical cavity by use of spatial mode interference," Optics Letters **24**, 1499 (1999).

[84] R. W. P. Drever, J. L. Hall, F. V. Kowalski, J. Hough, G. M. Ford, a. J. Munley, and H. Ward, "Laser phase and frequency stabilization using an optical resonator," Applied Physics B Photophysics and Laser Chemistry **31**, 97–105 (1983).

[85] E. D. Black, "An introduction to Pound-Drever-Hall laser frequency stabilization," American Journal of Physics **69**, 79 (2001).

[86] J. Q. Xi, M. F. Schubert, J. K. Kim, E. F. Schubert, M. Chen, S. Y. Lin, W. Liu, and J. A. Smart, "Optical thin-film materials with low refractive index for broadband elimination of Fresnel reflection," Nature Photonics **1**, 176–179 (2007).

[87] E. J. McLellan and J. F. Figueira, "Ultrafast Pockels cells for the infrared," Review of Scientific Instruments **50**, 1213–1217 (1979).

[88] C. Hayes, R. Brandewie, W. Davis, and G. Mevers, "Experimental test of an infrared phase conjugation adaptive array," Journal of the Optical Society of America A **67** (1977).

[89] V. J. Fowler and J. Schlafer, "A Survey of Laser Beam Deflection Techniques," Proceedings of the IEEE **54**, 1437–1444 (1966).

[90] A. Bosco, S. T. Boogert, G. E. Boorman, and G. a. Blair, "A large aperture electro-optic deflector," Applied Physics Letters **94**, 211104 (2009).

[91] D. Eimerl, L. Davis, S. Velsko, E. Graham, and A. Zalkin, "Optical, mechanical, and thermal properties of barium borate," Journal of Applied Physics **62**, 1968–1983 (1987).

[92] J. Limpert, S. Breitkopf, T. Eidam, A. Klenke, I. Pupeza, and A. Tünnermann, "Patent: WO2014056989A1 - Optischer überhöhungsresonator," (2013).

[93] A. A. Michelson and W. E. Morley, "On the relative motion of the Earth and the luminiferous ether," American Journal of Science **34**, 333–345 (1887).

[94] A. Freise, A. Bunkowski, and R. Schnabel, "Phase and alignment noise in grating interferometers," New Journal of Physics **9** (2007).

[95] D. C. S. Beddows, B. C. Griffiths, O. Samek, and H. H. Telle, "Devices To Analytical Laser Spectroscopy," Applied Optics **42** (2003).

[96] E. Shestaev, "A passively mode-locked Yb : KYW oscillator for cavity enhancement," Research labworks report, Friedrich-Schiller-Universität Jena (2014).

[97] E. Shestaev, "Femtosecond oscillators for non-steady-state enhancement cavities," Master thesis, Friedrich-Schiller-Universität Jena (2015).

[98] H. Liu, J. Nees, and G. Mourou, "Diode-pumped Kerr-lens mode-locked Yb : KY (WO4) 2 laser," **26**, 1723–1725 (2001).

[99] U. Keller, K. J. Weingarten, F. X. Kärtner, D. Kopf, B. Braun, I. D. Jung, R. Fluck, C. Hönninger, N. Matuschek, and J. Aus Der Au, "Semiconductor saturable absorber mirrors (SESAM's) for femtosecond to nanosecond pulse generation in solid-state lasers," IEEE Journal on Selected Topics in Quantum Electronics **2**, 435–451 (1996).

[100] F. Lücking, "Carrier-Envelope Phase Control for the Advancement of Attosecond Pulse Generation," Phd-thesis, LMU München (2014).

[101] S. Holzberger, N. Lilienfein, M. Trubetskov, H. Carstens, F. Lücking, V. Pervak, F. Krausz, and I. Pupeza, "Enhancement cavities for zero-offset-frequency pulse trains," Optics Letters **40**, 2165 (2015).

[102] D. Herriott, H. Kogelnik, and R. Kompfner, "Off-Axis Paths in Spherical Mirror Interferometers," Applied Optics **3**, 523 (1964).

[103] Dennis Hall, *The Physics and Technology of Laser Resonators* (CRC Press, 1990).

[104] A. Valentini, A. Convertino, M. Alvisi, R. Cingolani, T. Ligonzo, R. Lamendola, and L. Tapfer, "Synthesis of silicon carbide thin films by ion beam sputtering," Thin Solid Films **335**, 80–84 (1998).

[105] J. Becker and V. Scheuer, "Coatings for optical applications produced by ion beam sputter deposition." Applied optics **29**, 4303–9 (1990).

[106] B. C. Stuart, M. D. Feit, S. Herman, A. M. Rubenchik, B. W. Shore, and M. D. Perry, "Nanosecond-to-femtosecond laser-induced breakdown in dielectrics," Physical Review B **53**, 1749–1761 (1996).

[107] B. C. Stuart, M. D. Feit, A. M. Rubenchik, B. W. Shore, and M. D. Perry, "Laser-induced damage in dielectrics with nanosecond to subpicosecond pulses," Physical Review Letters **74**, 2248–2251 (1995).

[108] C. Kerse, H. Kalaycioglu, P. Elahi, B. Cetin, D. K. Kesim, Ö. Akcaalan, S. Yavas, M. D. Asik, B. Oktem, H. Hoogland, R. Holzwarth, and F. Ö. Ilday, "Ablation-cooled material removal with ultrafast bursts of pulses," Nature **537**, 84–88 (2016).

[109] P. Wagner, "Laser-induced contamination on high-reflective optics," Master thesis, Hochschule Darmstadt (2014).

[110] Y. Cui, Y. Zhao, H. Yu, H. He, and J. Shao, "Impact of organic contamination on laser-

induced damage threshold of high reflectance coatings in vacuum," Applied Surface Science **254**, 5990–5993 (2008).

[111] M. Cammarata, L. Eybert, F. Ewald, W. Reichenbach, M. Wulff, P. Anfinrud, F. Schotte, A. Plech, Q. Kong, M. Lorenc, B. Lindenau, J. Räbiger, and S. Polachowski, "Chopper system for time resolved experiments with synchrotron radiation." The Review of scientific instruments **80**, 1–10 (2009).

[112] N. Lilienfein, S. Holzberger, and I. Pupeza, "Ultrafast optomechanical pulse picking," Applied Physics B **123**, 47 (2017).

[113] T. Baumgartner, R. Burkar, J. W. Kolar, S. S.-b. P.-m. Motor, T. Baumgartner, S. Member, R. M. Burkart, S. Member, and J. W. Kolar, "Analysis and Design of a 300-W 500 000-r / min Slotless Self-Bearing Permanent-MagnetMotor," IEEE Transactions on industrial Electronics **61**, 4326–4336 (2014).

[114] C. Zwyssig, S. Member, J. W. Kolar, S. Member, S. D. Round, and S. Member, "Megaspeed Drive Systems : Pushing Beyond 1 Million r/min," IEEE/ASME Transactions on mechatronics **14**, 564–574 (2009).

[115] G. Marshall and G. Stutz, *Handbook of Optical and Laser Scanning, Performance, and Design* (2011).

[116] A. G. Fox and T. Li, "Resonant Modes in a Maser Interferometer," Bell System Technical Journal **40**, 453 – 488 (1961).

[117] N. Lilienfein, C. Hofer, S. Holzberger, C. Matzer, P. Zimmermann, M. Trubetskov, V. Pervak, and I. Pupeza, "Enhancement cavities for few-cycle pulses," Optics Letters **42**, 271–274 (2017).

[118] E. Black, "Notes on the Pound-Drever-Hall technique," (1998).

[119] L. von Grafenstein, "Stacking of Chirped Femtosecond Pulses with an Ultra-long Enhancement Cavity," Master thesis, Friedrich-Schiller-Universität Jena (2014).

Danksagung

Zu allererst möchte ich mich bei Jens Limpert sowie Andreas Tünnermann für die Betreuung, die Unterstützung und das außergewöhnlich gute Arbeitsumfeld am IAP bedanken. Desweiteren möchte ich mich bei Tino Eidam für die große Unterstützung in der Anfangsphase der Promotion bedanken. Bei der Laborarbeit und bei inhaltlichen Diskussionen haben mich vorallem meine beiden Master-Studenten Lorenz von Grafenstein und Stefano Wunderlich stets motiviert und zuverlässig unterstützt. Mein großer Dank gilt außerdem Evgeny Shestaev, der immer bereitwillig geholfen hat, wenn der Oszillator mal wieder seine chaotischen Momente hatte. Dank gilt auch dem Rest der Combining-Crew: Arno Klenke, Marco Kienel, Michael Müller und Henning Stark, die mir regelmäßig mit Rat und Tat zur Seite standen.

Ganz generell war die freundschaftliche Atmosphäre, der enge Gruppenzusammenhalt und die große Hilfbereitschaft aller Kollegen einer der Gründe, warum man jeden Tag gerne wieder ans Institut gekommen ist, auch an Tagen, an denen im Labor mal nichts so funktioniert hat, wie gedacht. Daher gilt ein ganz großer Dank der gesamten Faserlasergruppe für diese bemerkenswerte Kollegialität. Insbesondere seien hier all jene genannt mit denen ich im Laufe der Jahre die Freude hatte das Büro zu teilen: Enrico Seise, César Jáuregui, Arno Klenke, Jan Rothardt, Steffen Hädrich, Thomas Gottschall, Christoph Stihler, Robert Klas, Alexander Kirsche und Albrecht Steinkopff. Aber auch Stefan Demmler, Hans-Jürgen Otto, Florian Jansen, Fabian Stutzki und Vittoria Schuster sollen hier nicht unerwähnt bleiben!

Auch außerhalb des IAPs hatte ich das Vergnügen im Rahmen gemeinsamer Projekte mit motivierten und sympathischen Menschen zusammen zu arbeiten. Das gilt vorallem für die Kollegen am Max-Planck-Institut in Garching: Ioachim Pupeza, Henning Carstens, Simon Holzberger und allen voran Nikolai Lilienfein, mit dem ich in der Endphase noch einige spannende Experimente durchführen konnte.

Nicht zuletzt danke ich meiner Familie und meinen Freunden, die für den nötigen Ausgleich gesorgt haben und so das Gesamtpaket Promotionszeit perfekt abgerundet haben. Meine Schwester hat außerdem noch zahlreiche fehlende Kommas ergänzt. Ganz besonders möchte ich mich jedoch bei meiner Lebengefährtin Linn Handel bedanken, die stets ein offenes Ohr hatte, wenn ich einmal über ein nicht funktionierendes Experiment oder ein abgelehntes Paper fluchen musste.

Ehrenwörtliche Erklärung

Ich erkläre hiermit ehrenwörtlich, dass ich die vorliegende Arbeit selbständig, ohne unzulässige Hilfe Dritter und ohne Benutzung anderer als der angegebenen Hilfsmittel und Literatur angefertigt habe. Die aus anderen Quellen direkt oder indirekt übernommenen Daten und Konzepte sind unter Angabe der Quelle gekennzeichnet. Beim Erstellen dieser Arbeit habe ich mich an der "Empfehlung der Konferenz der Fachbereiche Physik" für die "Gute wissenschaftliche Praxis bei wissenschaftlichen Qualifikationsarbeiten in der Physik " vom 18. Mai 2016 orientiert.

Bei der Auswahl und Auswertung folgenden Materials haben mir die nachstehend aufgeführten Personen in der jeweils beschriebenen Weise geholfen:

- Die Koautoren der entsprechenden Publikationen bei durchgeführten Experimenten.
- Lars-Henning Stark und Thomas Gottschall halfen mir bei der Multi-Pass-Zellen Simulation mittels Zeemax und Matlab.
- Nikolai Lilienfein unterstütze mich bei der Abschätzung der thermischen Effekte in der High-Power Cavity.
- Michael Butzek und Eberhardt Rosenthal lieferten die Ergebnisse der Chopper-Studie.

Weitere Personen waren an der inhaltlich-materiellen Erstellung der vorliegenden Arbeit nicht beteiligt. Insbesondere habe ich hierfür nicht die entgeltliche Hilfe von Vermittlungs- bzw. Beratungsdiensten (Promotionsberater oder andere Personen) in Anspruch genommen. Niemand hat von mir unmittelbar oder mittelbar geldwerte Leistungen für Arbeiten erhalten, die im Zusammenhang mit dem Inhalt der vorgelegten Dissertation stehen. Die Arbeit wurde bisher weder im In- noch im Ausland in gleicher oder ähnlicher Form einer anderen Prüfungsbehörde vorgelegt. Die geltende Promotionsordnung der Physikalisch-Astronomischen Fakultät ist mir bekannt.

Ich versichere ehrenwörtlich, dass ich nach bestem Wissen die reine Wahrheit gesagt und nichts verschwiegen habe.

Jena, den

Dipl. Phys. Sven Breitkopf

A. Appendix

This appendix aims to give some very particular but potentially practical information on some aspects of this thesis.

A.1. Derivation of the Formula for the Extracted Enhancement

We define E_R as the intra-cavity field at the end of the previous build-up and for the sake of readibility $\eta_{rem} = 1 - \eta_{ext}$. It is now possible to derive an equation for the enhanced field in the cavity (similar to [76])

$$E_1 = t \cdot E_{in} + r\alpha\sqrt{\eta_{rem}} \cdot E_R$$

$$E_2 = t \cdot E_{in} + r\alpha \left[t \cdot E_{in} + r\alpha\sqrt{\eta_{rem}} \cdot E_R\right]$$

$$\vdots$$

$$E_N = t \cdot E_{in} \sum_{n=0}^{N-1} (r\alpha)^n + (r\alpha)^N \sqrt{\eta_{rem}} \cdot E_R$$

$$E_N = t \cdot E_{in} \frac{(r\alpha)^N - 1}{r\alpha - 1} + (r\alpha)^N \sqrt{\eta_{rem}} \cdot E_R \ .$$

E_R depends on the final field in the cavity during the previous buildup. Therefore the parameter k is introduced, which depicts the number of build-up cycles. It is now possible to write:

$$E_{N,k=1} = t \cdot E_{\text{in}} \frac{(r\alpha)^N - 1}{r\alpha - 1} + (r\alpha)^N \sqrt{\eta_{\text{rem}}} \cdot E_{N,k=0}$$

$$E_{N,k=2} = t \cdot E_{\text{in}} \frac{(r\alpha)^N - 1}{r\alpha - 1} + (r\alpha)^N \sqrt{\eta_{\text{rem}}} \cdot E_{N,k=0}$$

$$E_{N,k=2} = t \cdot E_{\text{in}} \frac{(r\alpha)^N - 1}{r\alpha - 1} + t \cdot E_{\text{in}} \frac{(r\alpha)^N - 1}{r\alpha - 1} (r\alpha)^N \sqrt{\eta_{\text{rem}}} + \left[(r\alpha)^N \sqrt{\eta_{\text{rem}}} \right]^2 \cdot E_{N,k=0}$$

$$\vdots$$

$$E_{N,k} = t \cdot E_{\text{in}} \frac{(r\alpha)^N - 1}{r\alpha - 1} (r\alpha)^N \sum_{j=1}^{k-1} (\sqrt{\eta_{\text{rem}}})^j$$

$$E_{N,k\to\infty} = \frac{t \cdot E_{\text{in}} \frac{(r\alpha)^N - 1}{r\alpha - 1}}{1 - (r\alpha)^N \sqrt{\eta_{\text{rem}}}} \tag{A.1}$$

When substituting back $\eta_{rem} = 1 - \eta_{\text{ext}}$,the extracted enhancement V_{ext} can be written as:

$$V_{\text{ext}} = \eta_{\text{diff}} \cdot V_{\text{eff}} = \eta_{\text{ext}} \cdot \frac{|E_{\text{N},\infty}|^2}{|E_{\text{in}}|^2}$$

$$V_{\text{ext}} = \eta_{\text{ext}} \cdot \frac{(1-R)\left[\left(\sqrt{AR}\right)^N - 1 \right]^2}{\left(\sqrt{AR} - 1\right)^2 \left[1 - \left(\sqrt{AR}\right)^N \sqrt{1 - \eta_{\text{ext}}} \right]^2} \tag{A.2}$$

A.2. Exemplary Calculation of a Stable Caustic and Beam Parameters at IC
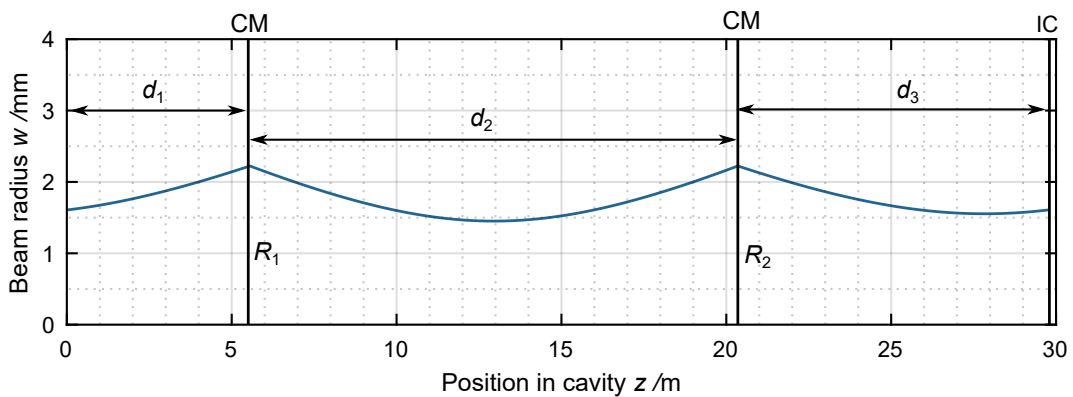

Figure A.1.: Simple cavity caustic.

As an example a simple ring-cavity consisting of two curved mirrors and some plane-mirrors is shown in fig. A.1. Since plane mirrors have no effect on the beam properties, we can neglect them. The matrix therefore simply consists of the curved mirrors and the distances between them. However, since we are interested in the beam parameters at the input-coupler we arrange the elements in the following order:

$$
\mathcal{M} = \mathcal{M}_{d_3} \cdot \mathcal{M}_{R_2} \cdot \mathcal{M}_{d_2} \cdot \mathcal{M}_{R_1} \cdot \mathcal{M}_{d_1}
$$

$$
\mathcal{M} = \begin{pmatrix} 1 & d_3 \\ 0 & 1 \end{pmatrix} \begin{pmatrix} 1 & 0 \\ -\frac{2}{R_2} & 1 \end{pmatrix} \begin{pmatrix} 1 & d_2 \\ 0 & 1 \end{pmatrix} \begin{pmatrix} 1 & 0 \\ -\frac{2}{R_1} & 1 \end{pmatrix} \begin{pmatrix} 1 & d_1 \\ 0 & 1 \end{pmatrix}
$$

$$
\mathcal{M} = \begin{pmatrix} -\frac{2d_3}{R_2} - \frac{2\left(d_3+d_2\left(1-\frac{2d_3}{R_2}\right)\right)}{R_1} + 1 & d_2 + d_2\left(1 - \frac{2d_3}{R_2}\right) + d_1\left(-\frac{2d_3}{R2} - \frac{2\left(d_3+d_2\left(1-\frac{2d_3}{R_2}\right)\right)}{R_1} + 1\right) \\ -2\frac{\left(1-\frac{2d_2}{R_2}\right)}{R_1} - \frac{2}{R_2} & -\frac{2d_2}{R_2} + d_1\left(-\frac{2\left(1-\frac{2d_2}{R_2}\right)}{R_1} - \frac{2}{R_2}\right) + 1 \end{pmatrix} .
$$

One can now easily insert the distances between the curved mirrors d_1, d_2 and d_3 as well as the radii of curvature R_1 and R_2 to get $\mathcal{M}$. Using

$$
R = \frac{2B}{D-A} \quad \text{and} \quad w = \sqrt{\frac{2\lambda\,|B|}{\pi\sqrt{4-(A+D)^2}}} , \tag{A.3}
$$

allows to also calculate the curvature and waist of the fundamental mode at the input-coupling mirror (IC), which can then be easily matched by adjusting the last telescope before the cavity input to make the incoming beam match these parameters at the position were it is transmitted through the IC. However it becomes clear, even for such a simple cavity, that due to their length such calculations are usually not done by hand but rather via Matlab or Python. They also allow to easily plot the entire caustic as shown in Fig. A.1.

A.3. Calculation of the Round-trip Attenuation from Coupling Parameter and Measured Enhancement

K is given as

$$K = 1 - \frac{P_r}{P_{\text{in}}} = U \left[1 - \frac{\left(\sqrt{A} - \sqrt{R} \right)^2}{\left(1 - \sqrt{AR} \right)^2} \right] , \qquad (A.4)$$

wherein P_r is derived similarly to P_{IC} (see [76]) . Furthermore V_{eff} is given by

$$V_{\text{eff}} = U \frac{1 - R}{\left(1 - \sqrt{R} \right)^2} . \qquad (A.5)$$

The ratio of both can be calculated as follows:

$$
\begin{aligned}
\frac{K}{V_{\text{eff}}} &= \frac{\left(1 - \sqrt{R} \right)^2 - \left(\sqrt{A} - \sqrt{R} \right)^2}{1 - R} \\
&= \frac{1 - R - A(1 - R)}{1 - R} \\
\frac{K}{V_{\text{eff}}} &= 1 - A .
\end{aligned}
$$

This eventually leads to

$$A = 1 - \frac{K}{V_{\text{eff}}} . \qquad (A.6)$$

A.4. Pound-Drever-Hall Error Signal Calculation

The following derivation is oriented on the calculations in [118] and [85] and similarly edited as in [119].

In order to generate a assymetrical error-signal around the correct length of the cavity, the phase of the incident field is modulated and frequency side-bands are created

$$E(t) = E_{\text{in}} \exp \left\{ \mathrm{i} \left[\omega_{\text{in}} t + \beta \sin(\omega_m t) \right] \right\} .$$

If one assumes a small modulation depth $\beta \ll \pi$ and a sinusoidal modulation, the resulting

field can be decomposed in a Taylor-series

$$E(t) = E_{\text{in}} \exp\left(i\omega_{\text{in}}t\right)\left[1 + i\beta\sin(\omega_m t)\right] + \dots$$

$$E(t) = E_{\text{in}}\left\{\exp\left(i\omega_{\text{in}}t\right) + \frac{\beta}{2}\exp\left[i\left(\omega_{\text{in}} + \omega_m\right)t\right] - \frac{\beta}{2}\exp\left[i\left(\omega_{\text{in}} - \omega_m\right)t\right]\right\} . \qquad \text{(A.7)}$$

Hence, after the phase modulation, E can be expressed as the sum of three electric fields with a frequency separation of the modulation frequency ω_m. The modulation depth β determines how much power is in the sidebands. The error signal is generated by the reflected light, whereas the reflection coefficient describes the amplitude of this field in dependence of the phase and, therefore, in dependence of the frequency

$$\delta(\omega) = \frac{s_c\omega}{c} = \frac{\omega}{\text{FSR}} . \qquad \text{(A.8)}$$

When the laser frequency is a multiple of the free spectral range, the phase is zero and the reflection coefficient gets minimal. The modulated beams have a slightly different frequency above and below and, therefore, a different phase and finally amplitude. The reflected signal is now calculated by multiplying each field with its corresponding reflection coefficient $r(\omega) = \sqrt{R(\omega)}$.

$$E(t) = E_{\text{in}}\left\{r(\omega)\exp\left(i\omega t\right) + r(\omega + \omega_m)\tfrac{\beta}{2}\exp\left[i\left(\omega + \omega_m\right)t\right]\right.$$
$$\left. - r(\omega - \omega_m)\tfrac{\beta}{2}\exp\left[i\left(\omega - \omega_m\right)t\right]\right\} . \qquad \text{(A.9)}$$

Since a photodiode detects an intensity and not the electric field, the reflected intensity Ir has to be calculated in dependence of the incident intensity I_0. With $I \sim |E|^2$ it follows to be

$$I_r = I_0\left|r(\omega)\right|^2 + I_0\frac{\beta^2}{4}\left[\left|r(\omega + \omega_m)\right|^2 + \left|r(\omega - \omega_m)\right|^2\right]$$
$$+ \frac{\beta}{2}I_0\left\{\Re\left[r(\omega)r^*(\omega + \omega_m) - r^*(\omega)r(\omega - \omega_m)\right]\cos(\omega_m t)\right. \qquad \text{(A.10)}$$
$$+ \Im\left[r(\omega)r^*(\omega + \omega_m) - r^*(\omega)r(\omega - \omega_m)\right]\sin(\omega_m t)\right\} + \mathcal{O}(2\omega_m) .$$

An electronic component is employed in order to "mix" out all the terms which are proportional to $\sin(\omega_m t)$ and its higher harmonics. Since β is small, their amplitude is small but

may have to be filtered with a low-pass filter. The final consequently error signal reads as

$$\epsilon = \frac{\beta}{2} \Im\left[r(\omega)r^*(\omega + \omega_m) - r^*(\omega)r(\omega - \omega_m)\right] \ . \tag{A.11}$$

A plot with some examples can be found in Fig. 3.10.